PATTERNS OF ELECTRO-MAGNETIC RESPONSE IN TOPOLOGICAL SEMI-METALS

BY

SRINIDHI T. RAMAMURTHY

DISSERTATION

Submitted in partial fulfillment of the requirements
for the degree of Doctor of Philosophy in Physics
in the Graduate College of the
University of Illinois at Urbana-Champaign, 2019

Urbana, Illinois

Doctoral Committee:

Professor Philip W. Phillips, Chair
Professor Taylor L. Hughes, Director of Research
Professor S. Lance Cooper
Professor Robert G. Leigh

Abstract

Topological semimetals are gapless states of matter which have robust and unique electromagnetic responses and surface states. In this thesis, we consider semimetals which have point like Fermi surfaces in various spatial dimensions $D = 1, 2, 3$ which naturally occur in the transition between nth order weak topological insulators and a trivial insulating phase. These semimetals include those of Dirac and Weyl type. We construct these phases by layering strong topological insulator phases in lower dimensions. This perspective helps us understand their effective response field theory, which is generally characterized by a n-form which represents a source of Lorentz violation and can be read off from the location of the singular points in momentum space and the helicities/chiralities of the singularities. We motivate and derive effective response actions for the 2D and 3D Dirac semi-metals, the Weyl semimetal, the 3D line node semi-metal and the 3D mirror protected topological crystalline insulator.

To my parents and mentors

Acknowledgments

I am deeply grateful to my adviser Taylor L. Hughes for his guidance and constant source of encouragement through my years in graduate school. The emphasis he laid on understanding the physics of a problem, and in clear explanation of the requisite ideas and mathematics has shaped the way I think about physics, and in general any quantitative discipline. I thank Robert G. Leigh and Philip W. Phillips for collaborations and help in many of my projects through graduate school. I am indebted to the graduate program at the University of Illinois, under S. Lance Cooper for being a huge source of advice and encouragement through the years, and for making me feel at home when away from family.

I have learned a tremendous amount from fellow students and postdoctoral researchers at the university, I thank Onkar Parrikar, Apoorv Tiwari, Garrett Vanacore, Vatsal Dwivedi, Wladimir Benalcazar, Yuxuan Wang, Philip Russ, Mohammed Sheikh, Jackson Fliss, Matthew Lapa, Mayukh Khan, Jeffrey Teo, Ian Mondragon-Shem, and Victor Chua. I am also grateful to all my friends here at Urbana-Champaign - Venanzio Cichella, Caterina Lamuta, Sergio Poo Dalidet, Megan White, Erman Gungor, Giusy Falcone Demaria, Rob Rouphail and Samantha Brotman.

Last, but certainly not least, I am deeply grateful to my parents, my sister Surabhi, my brothers Srikanth and Nishikant and my nephew Ayansh who have been a constant source of love and affection. None of this would have been possible without them.

I acknowledge support from ONR award N0014-12-1-0935 and ONR YIP Award N00014-15-1-2383.

Table of Contents

Chapter 1

Introduction

The discovery of topological band insulators (TIs) and their novel electronic properties has led to a re-examination and search for robust topological features of the electronic structure of many different material types [41]. Some notable properties of topological insulators include a gapped, insulating bulk interior, protected boundary modes that are robust even in the presence of disorder, and quantized electromagnetic transport. A full (periodic) classification table of non-interacting fermionic states of matter that are protected by time-reversal (T), chiral, and/or particle-hole (C) symmetries has been established [82, 75, 57]. Recent work has further augmented the initial periodic table by including the classification of states protected by spatial symmetries such as translation, reflection, and rotation [30, 91, 29, 47, 94, 27, 90, 86, 3, 66, 18, 28, 48, 95, 112, 52]. While these symmetry protected topological phases are theoretically interesting in their own right, this field would not have attracted so much attention if it were not for the prediction and confirmation of candidate materials for many different topological classes. A few examples are the 2D quantum spin Hall insulator (e.g., CdTe/HgTe quantum wells [54, 7, 58]), the 3D T-invariant strong topological insulator (e.g., BiSb [44], Bi_2Se_3 [64, 104, 113]), the 2D quantum anomalous Hall (Chern) insulator (e.g., Cr-doped $(Bi,Sb)_2Te_3$ [37, 14]), and the 3D T-invariant topological superfluid state (e.g., the B-phase of He-3 [73, 82, 57]).

All of above work pertains to gapped systems, however, recent theoretical predictions have shown that even materials that are not bulk insulators can harbor robust topological electronic responses,transport properties, and conducting surface/boundary states [69, 99, 93, 38, 61, 70, 17, 53, 42]. This class of materials falls under the name topological semi-metals, and represents another type of non-interacting electronic structure with a topological imprint. The most well-studied examples of topological semi-metals (TSMs) are the 2D Dirac semi-metal (e.g., graphene [12]), the 3D Weyl semi-metal (possibly in pyrochlore irridates [99], inversion-breaking super-lattices [36], or optical lattices [33]), the 3D Dirac semi-metal [110, 100, 60, 68, 101, 107] and the 3D line node semi-metal. The incomplete Fermi-arc surface modes, an anomalous Hall effect(AHE), and a chiral magnetic effect has drawn theoretical and experimental attention to Weyl semi-metals. Two types of 3D Dirac semi-metals, i.e. a Dirac semi-metal type with nodes at the time-reversal invariant momenta [110, 68, 101], and one with nodes away from those special momenta [100, 60] have been reported to be found. In addition to these TSMs there is a large set of symmetry-protected TSMs which rely on additional symmetries for their stability [61]. Finally, we also note that there are superconducting relatives of these semi-metal phases called topological nodal superconductors, or Weyl superconductor phases, that await experimental discovery [62, 19, 61], though we will not consider them further.

In this thesis, we explore the quasi-topological response properties of TSMs in the presence of external electromagnetic fields. We present a generic construction of TSMs that can be adapted to model almost any type of TSM. This construction allows us to manifestly determine the electromagnetic response properties of the TSMs in question. It also enables us to uncover clear patterns in the quasi-topological electromagnetic response terms exhibited by the various semi-metal types and in different spatial dimensions. In addition, our work nicely complements the extensive recent work studying the topological response properties of semi-metals [99, 93, 38, 61, 43].

The previous field-theoretic calculations of the response of Weyl semi-metals have predicted a novel electro-magnetic response for the 3D TSMs, but not without some subtlety [34, 114, 98, 16, 38, 15, 96]. Thus, another goal of this thesis is to address the electro-magnetic (EM) response for various topological semi-metals, and to show the validity and limitations of the field-theory results. To this end, we provide explicit numerical simulations using simple lattice models to complement our transparent analytic discussion. In addition to the discussion of the 3D Weyl semi-metals, we carefully illustrate the pattern of TSM response actions that exist in 1D metallic wires and 2D Dirac semi-metals to establish a unified framework of the EM response of TSMs. We discuss the influence of and, in some cases, the necessity of, anti-unitary and/or spatial symmetries for the stability of the semi-metal phase, and the resultant implications for the EM response. Furthermore, we provide an analytic solution for the boundary modes of the TSMs in our simple lattice models, derive a topological effective response action for the 2D and 3D Dirac semi-metals, the 3D line node semi-metal, calculate the EM response at interfaces between different TSMs, and, where possible, emphasize the important physical quantities of TSMs that can be observed.

1.1 Preliminaries and motivation

One of the primary goals of this work is to produce valuable intuition for understanding the response properties of generic topological semi-metals with point-nodes and line-nodes. In this section, we will first consider point-nodes and then move onto line-nodes. We will begin with a simple physical construction that is applicable to different types of topological semi-metals and provides a basis for understanding the EM response of a wide-class of TSMs in a unified manner. In this context we will discuss some of the previous work on the EM response of Weyl semi-metals as an explicit example. Finally, before we move on to more technical calculations, we will illustrate the pattern followed by the electromagnetic response of TSMs in various spatial dimensions.

1.1.1 Electromagnetic response of point-nodes

An insightful way to view a topological semi-metal is as a stable gapless phase that separates a trivial insulator phase from a weak topological insulator phase. A trivial insulator is essentially a band insulator that is adiabatically connected to the decoupled atomic limit. The electronic structure of trivial insulators does not exhibit any non-vanishing topological properties. On the other hand, weak topological insulators (WTIs) are anisotropic, gapped topological phases that are protected by translation symmetry, and characterized by a vector topological invariant $\vec{\nu}$. The fact that the topological invariant is a vector, and not a scalar, is an indication that they are essentially anisotropic. This anisotropy can be made more apparent because each WTI phase in d spatial dimensions can be adiabatically connected to a limit of decoupled $d-1$-dimensional systems that are layered perpendicular to $\vec{\nu}$. The $(d-1)$-dimensional building blocks that make up the d-dimensional WTI must each be in a $(d-1)$-dimensional topological insulator phase to generate the higher dimensional WTI phase. Of course, one can also construct a d-dimensional WTI from $(d-q)$-dimensional $(1 < q < d)$ topological phases, which will lead to Fermi-surfaces with lower co-dimension although we save their consideration to later.

The most well-known example of a WTI is a stack of planes of 2D integer quantum Hall states (or 2D Chern insulators) that create the so-called 3D quantum Hall effect(QHE) [40, 63, 2, 6]. If the 2D planes are parallel to the xy-plane then the vector invariant $\vec{\nu} \propto \hat{z}$. If the coupling between the planes is weak, then the bulk gap, arising from the initial bulk gaps of the 2D planes, will not be closed by the dispersion in the stacking direction. However, when the inter-layer tunneling becomes strong enough, the system will become gapless and exhibit the so-called Weyl semi-metal phase. Eventually, as the tunneling strength increases, the system will transition to another gapped phase that will either be a different WTI phase or a trivial insulator. Thus, in the simplest case, the Weyl semi-metal is an intermediate gapless phase separating a WTI from a trivial insulator. As we will discuss later, a similar picture can be developed for the 2D Dirac semi-metal which can be adiabatically connected to an array of 1D TI wires that are stacked into 2D. Ultimately, this type of description of TSMs will be very useful since the relevant EM response properties of the lower dimensional TI building blocks are known [75], and the problem of the TSM response is transformed into understanding how the inter-layer coupling affects the EM responses of the TI constituents.

While it is well-known that TIs and WTIs exhibit topological electromagnetic response properties, at the transition between trivial and topological phases the relevant topological response coefficients are no longer well-defined, i.e. not sharply quantized. In fact, there is usually a jump from a quantized non-zero value in the topological phase to a vanishing value of the response coefficient in the trivial phase. Therefore, it is a bit surprising that the semi-metal phases intermediate between trivial and topological insulators retain an imprint of the topological response.

This is illustrated beautifully in the case of the Weyl semi-metal as we will now discuss. A trivial insulator has no topological component to its EM response, it obeys Maxwell's equations with the conventional insulator constituent relations for polarization and magnetization. On the other hand, the non-trivial WTI represented by the 3D quantum Hall insulator produces a topological response term in the effective action

$$S_{eff}[A_\mu] = -\frac{e^2}{2\pi h}\int d^3x dt\ \nu_\mu \epsilon^{\mu\sigma\rho\tau} A_\sigma \partial_\rho A_\tau \tag{1.1}$$

where $\nu_0 = 0$, $\nu_i = \frac{n}{2}G_i$ are the components of a half-integer multiple $n/2$ of a reciprocal lattice vector $\vec{G}$, and A_μ are external EM fields. This action implies that spatial planes perpendicular to $\vec{\nu}$ will have a Hall effect, and the 3D Hall conductance is $\sigma_{xy} = -ne^2/ha_G$ where a_G is the lattice spacing along $\vec{G}$ ($a_G = 2\pi/|\vec{G}|$). Note that we have chosen the global negative sign to match the convention of [114]. The trivial insulator phase can be thought of as the case when $\vec{\nu} = \vec{0}$. It is clear that the topological response is anisotropic, as the particular $\vec{\nu} = \frac{\vec{G}}{2}$ breaks rotation invariance, and as a consequence Lorentz invariance if we are considering relativistic theories which are a common low-energy description of a TSM. Generically the electromagnetic response properties of topological semi-metals with point-nodes is determined by a vector b_μ. If this vector is non-vanishing, then this vector generally violates Lorentz invariance since both the time and space components can be non-vanishing. If only the spatial components were non-zero, as is found, for example, in a weak topological insulator, then the system is simply anisotropic. However, the semi-metal response is more general. Throughout this thesis, we will often use the term Lorentz-violation to imply one of several things. First, any source of anisotropy we term as violating Lorentz invariance, whether it arises from an external field such as an electric field, or intrinsically due to the crystal structure or electronic structure of the system in question. The crystal lattice itself provides direct and reciprocal lattice vectors which are signatures of anisotropy, and if there are point-like Fermi surfaces in the Brillouin zone they can also serve as a signal of anisotropy/Lorentz violation. Additionally, the topological semi-metals are often described at low-energy by a massless relativistic continuum theory when expanded near the point-nodes. Thus, we will often encounter three additional sources of Lorentz violation (i) differences in energy between

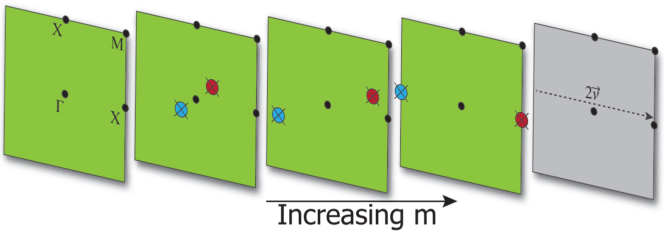

Figure 1.1: Schematic Illustration of the motion of point-nodes in the $k_z = 0$ plane of a cubic, 3D Brillouin zone as a parameter m is adjusted. As m increases two Weyl nodes with opposite chirality (as represented by the color shading) are created in the 2D subspace (i.e., $k_z = 0$) of a full 3D Brillouin zone. As m increases further, the nodes move throughout the Brillouin zone, meet at the boundary, and then finally annihilate to create a gapped phase with a weak topological invariant proportional to the reciprocal lattice vector separation $\vec{G} = 2\vec{\nu}$ of the Weyl nodes before annihilation. The far left Brillouin zone represents a trivial insulator, the far right represents a weak topological insulator, and the intermediate slices represent the Weyl semi-metal phase.

the nodes (ii) differences in velocity ("speed of light") of the massless dispersions of the nodes, and (iii) background charge density and/or current density which give rise to a preferred frame. Thus, when we use the term Lorentz violation we are referring to a general extrinsic or intrinsic source that picks out a "preferred frame" whether it be due to spatial anisotropy or a more general mechanism. These sources are termed as such because they can generate a non-vanishing b_μ..

Now that we understand the topological response of the two phases that straddle the Weyl semi-metal phase, we can try to understand the response of the simplest type of Weyl semi-metal, i.e., the kind with only two Weyl nodes (the minimal number). Let us imagine the following process where we begin with a trivial insulator and nucleate two Weyl nodes at the Γ-point in the 3D Brillouin zone (BZ) by tuning a parameter m (see Fig. 1.1). The low-energy $k \cdot P$ Hamiltonian near each Weyl-node is of the form $H_{Weyl}(\mathrm{p}) = p_1\sigma^1 + p_2\sigma^2 + p_3\sigma^3$ where σ^a are Pauli matrices and we have set the velocity to unity. As m is further changed, the Weyl nodes will move through the BZ but cannot be gapped (assuming translation invariance) unless they meet each other again, or another node with opposite chirality. The reason is that if the Weyl-nodes are separated, then there is no matrix which anti-commutes with $H_{Weyl}(\mathrm{p})$, and thus no perturbation can be added that will open a gap. If the two Weyl nodes (with opposite chirality) meet and become degenerate, then the resulting 4×4 Hamiltonian $H_{Weyl} \oplus \widetilde{H}_{Weyl}$ has the Dirac form. In this case one can find an anti-commuting matrix to add that will perturbatively open a gap and annihilate the nodes. If the Weyl nodes meet at the boundary of the BZ, at points which differ by a reciprocal lattice vector $\vec{G}$, then upon annihilation the system will undergo a change of its weak-invariant, i.e., $\Delta\vec{\nu} = \frac{\vec{G}}{2}$. Thus if the system starts with $\vec{\nu} = 0$ then it will have a transition to a non-trivial WTI during this process.

During the process of tuning m we see that before we nucleate the Weyl nodes, there is no topological response, and after they annihilate at the BZ boundary there will be a non-trivial Hall response. We now can ask, what is the response in the gapless semi-metal phase? The answer turns out to be simple, we just have the response of Eq. 1.1 with $\vec{\nu} = \vec{b}$ where $2\vec{b}$ is the difference in momentum between the two Weyl nodes [114]. Interestingly, the response coefficient smoothly interpolates between the two insulating end-points. This remarkable result can be extended even further because we also have a notion of a relative energy between the Weyl nodes. Because of this, we can generate a coefficient $\nu_0 = b_0$ in Eq. 1.1 where $2b_0$ is the energy difference between the two Weyl nodes. This enhances the response as now we can have a Lorentz-invariance violating 4-vector response coefficient ν_μ.

The addition of a response proportional to ν_0 is a new feature of the semi-metal since one cannot define a notion of ν_0 in the pure WTI because the low-energy theory is gapped. The reason one can have a spatial vector in the gapped WTI is because of the translation symmetry (and continuous rotation symmetry) breaking lattice structure which gives rise to the reciprocal lattice vector(s) $\vec{G}$. On the other hand, if we had a periodically driven system, i.e., a system evolving according to Floquet dynamics, then, even in the insulating case, we could have a non-zero ν_0 which would be proportional to the driving frequency of the time-dependent field, i.e., the reciprocal lattice vector for time. In the Weyl semi-metal phase, the existence of non-degenerate Weyl nodes immediately gives rise to a Lorentz-breaking 4-vector similar to the kind anticipated by [11, 49] for Lorentz-violation in high-energy physics.

The resulting response from Eq. 1.1 generates an anomalous Hall effect along with a chiral magnetic effect (CME). The chiral magnetic effect occurs when $b_0 \neq 0$, and is anticipated to give rise to a current when a magnetic field is applied to the system, but in the absence of any electric field. For a translation-invariant 3D material with an even number of Weyl nodes, we can determine

$$\vec{b} = \frac{1}{2}\sum_a \chi_a \vec{K}_a, \quad b_0 = \frac{1}{2}\sum_a \chi_a \epsilon_a \tag{1.2}$$

where the sum runs over all of the Weyl nodes, and χ_a, $\vec{K}_a$, and ϵ_a are the chirality, momentum location, and energy of the a-th node respectively. Additionally, from the Nielsen-Ninomiya no-go/fermion-doubling theorem we know there is also the constraint that the total chirality $\sum_a \chi_a = 0$ must vanish [69]. With these definitions, the resulting charge density and current in the semi-metal are given in terms of b_μ and the applied EM fields as

$$\begin{aligned} j^0 &= \frac{e^2}{2\pi h}(2\vec{b}) \cdot \vec{B} && (1.3) \\ \vec{j} &= \frac{e^2}{2\pi h}((2\vec{b}) \times \vec{E} - (2b_0)\vec{B}). && (1.4) \end{aligned}$$

As an aside, we note that while the origin and detection of the anomalous Hall current is well understood, there has been some disagreements in the recent literature about the possibility of a non-vanishing CME. To summarize the results so far, the field theoretical results are somewhat ambiguous because of the dependence on a regularization [34, 35]: a tight-binding lattice calculation has shown a vanishing result [98], while a more recent calculation has indicated the need for a slowly varying magnetic field that eventually tends toward a uniform/constant field [16]. In Section 4.1 we comment on these results and note that having an explicit source of Lorentz violation is a necessity for a non-vanishing CME effect. We also discuss the interpretation of the CME effect from a quasi-1D perspective generated from applying a uniform magnetic field to a Weyl semi-metal. This allows us to map the 3D problem onto degenerate copies of the 1D system, which can be more easily analyzed.

1.1.2 General pattern of quasi-topological electromagnetic response in topological semi-metals

While we have seen it is the case for the Weyl semi-metal, it is generically true that the general pattern of EM response for TSMs with point-nodes in any spatial dimension stems from the existence of the Lorentz-violating vector response coefficient b_μ. In systems with translation symmetry, the vector is connected to the momentum and energy difference between non-degenerate point-nodes (e.g., Dirac nodes in 2D and Weyl nodes in 3D). In general, the vector represents a source of Lorentz-violation in the system because it chooses a preferred direction or frame in the system, and its time and space components can both be non-vanishing. For example, the spatial part of b_μ represents an anisotropic “stacking-direction” similar to the case of the weak TI. Now, let us denote the external electromagnetic gauge field by A_a and its field strength by $F_{ab} = \partial_a A_b - \partial_b A_a$. In odd dimensional space-time ($D+1$ is odd), the effective electromagnetic response action for point-node semi-metals is

$$S[A] = \mathcal{A}_D \int \mathrm{d}^{D+1}x\, \epsilon^{a_1 a_2 \ldots a_{D+1}} b_{a_1} F_{a_2 a_3} \ldots F_{a_D a_{D+1}} \tag{1.5}$$

where the ellipses in the above equation represent further factors of the field strength, and $\mathcal{A}_D$ is a dimension dependent normalization coefficient. We see from this equation that if one calculates the current $j^\mu = \delta S[A]/\delta A_\mu$ then the result always depends on derivatives of b_μ. This is important because it immediately implies that the response of semi-metals in odd dimensional space-time depends crucially on the properties of boundaries or interfaces where b_μ is changing.

In contrast, in even space-time dimensions ($D+1$ is even), the effective action for the quasi-topological electromagnetic response of point-node semi-metals is

$$S[A] = \mathcal{A}_D \int \mathrm{d}^{D+1}x \, \epsilon^{a_1 a_2 \ldots a_{D+1}} b_{a_1} A_{a_2} F_{a_3 a_4} \ldots F_{a_D a_{D+1}} \tag{1.6}$$

where the ellipses in the above equation represent further factors of the field strength. For example in $1+1$-d, we have just $S[A] = \mathcal{A}_1 \int \mathrm{d}^2 x \, \epsilon^{\mu\nu} b_\mu A_\nu$. Now if one calculates the current the result depends depends on the value of b_μ itself (as well as possible derivatives in some cases). This hints that at least part of the response is determined by bulk effects alone and does not involve the properties of surfaces and boundaries. In even dimensional space-times the literature differs on the convention for the choice of the action and some sources use

$$S[A] = \frac{\mathcal{A}_D}{2} \int \mathrm{d}^{D+1}x \, \epsilon^{a_1 a_2 \ldots a_{D+1}} \theta F_{a_1 a_2} F_{a_3 a_4} \ldots F_{a_D a_{D+1}} \tag{1.7}$$

where $\theta \equiv 2 b_\mu x^\mu$. However this second form, while it looks somewhat nicer as far as gauge invariance is concerned, has an implicit breaking of translation symmetry. This comes from the freedom of the choice of origin in the definition of θ as we could have alternatively defined θ to be $\theta \equiv 2b_\mu(x^\mu + x_0^\mu)$ with some constant 4-vector x_0^μ. Because of this, we will always choose the form Eq. 1.6 to avoid the translation symmetry ambiguity. In fact, using the θ-term version of the action leads to spurious effects when the system is not homogeneous, e.g., in the presence of boundaries.

When we consider line-node semimetals however, the 1-form b_μ is replaced by a 2-form $B_{\mu\nu}$ and the pattern continues to hold. In even space-time dimensions, we have the form of the action to be:

$$S[A] = \mathcal{A}_D \int \mathrm{d}^{D+1}x \, \epsilon^{a_1 a_2 \ldots a_{D+1}} B_{a_1 a_2} F_{a_3 a_4} \ldots F_{a_D a_{D+1}} \tag{1.8}$$

while in odd space-time dimensions, we will have:

$$S[A] = \mathcal{A}_D \int \mathrm{d}^{D+1}x \, \epsilon^{a_1 a_2 \ldots a_{D+1}} B_{a_1 a_2} A_{a_3} F_{a_4 a_5} \ldots F_{a_D a_{D+1}}. \tag{1.9}$$

Again, we note how the action naturally interpolates between the response of a second order weak topological insulator and a trivial insulator in a continuous fashion just like in the case of point-node semimetals.

In general, the pattern of response actions for TSMs with nodal Fermi-surfaces is attached to an intrinsic n-form b which is determined from the electronic structure and the nodal manifold. This type of n-form indicates some inherent anisotropy in the electronic structure, and can appear in any dimension. The response of a TSM is only determined up to a quantum determined by the addition of a filled band because the n-forms depend inherently only on the location of the gapless points, and do not change under the addition of an arbitrary number of filled bands that do not change the locations of the nodes. For Weyl semi-metals this indeterminacy is due to the possibility of a contribution of an integer Hall conductance (per layer) from filled bands; the low-energy Fermi-surface physics does not contain information about the Hall conductance of the filled bands [39]. For cases where the response coefficients are connected to Z_2 invariants instead of integers, the ambiguity of contributions from filled bands must be carefully considered, as we do below for the 2D Dirac semi-metal and the line-node semimetal.

The most important feature of the quasi-topological response coefficients of TSMs is that the response coefficients *continuously* change throughout the gapless TSM phase from the quantized values in the insulating phases on either side of the gapless phase. One might expect that when the gap closes there might be some complicated singular behavior in the response coefficients, however, what is special about the TSM phases is that we can continuously track the coefficient through the weak TI-TSM-Trivial Insulator phase diagram. We note that there could be other transport coefficients that do have more complicated singular behavior during the insulator to TSM transitions, but the restricted set on which we focus has this important property.

1.2 Boundary degrees of freedom

The other generic feature of TSM phases is the existence of low-energy boundary modes. It is well-known that topological insulators have robust, gapless boundary modes that exist in the bulk energy gap. A (strong) TI will contain topological boundary states on any surface, while a WTI only harbors topologically protected boundary states on surfaces where $\vec{\nu}$ does not project to zero in the surface Brillouin zone [31]. This is another clear signature of the anisotropy, and it gets passed on to the TSMs that interpolate between the WTI and trivial insulator phases.

TSMs themselves will have low-energy boundary modes, but again, only on surfaces where b_i, B_{ij} do not project to zero in the surface Brillouin zone. That is, there will be surface states on surfaces where the normal vectors are not parallel to the node separation vector $\vec{b}$ or the normal to the plane of existence of the line-node in the case that it is planar. We note that even in cases where $b_i, B_{ij} = 0$ (or b_i, B_{ij} projects to zero on a surface) there can still be surface states because b_i is only well-defined modulo a reciprocal lattice vector. We note that surface states that exist when the semi-metal invariant is zero come from fully filled bands and will exist over the entire Brillouin zone (if the ground state does not carry a strong topological invariant). These surface states are not related to the properties of the semi-metal, and will not crucially depend on the locations of the nodes as they are continuously deformed.

The existence of boundary modes in TSMs is most easily illustrated with a simple example. Let us again resort to the picture of a Weyl semi-metal arising out of a stack of identical 2D Chern (quantum anomalous Hall) insulators and, for simplicity, assume that the layers are stacked in the z-direction. Then, for the WTI phase in the completely decoupled limit, each Chern insulator layer contributes one set of chiral edge modes on surfaces with normal vectors in the $\hat{x}$ and/or $\hat{y}$ directions [2]. This is the simple picture of a WTI, and if each layer has a first Chern number $C_1 = 1$, then the vector invariant $\vec{\nu} = (0, 0, \pi/a)$, where a is the spacing between the Chern insulator layers. If the system has length $L_z = Na$ in the z-direction, then the total Hall conductance is $\sigma_{ij} = -\epsilon_{ijk}\frac{e^2}{\pi h}\nu^k L_z = -N\frac{e^2}{h}$, i.e., an amount e^2/h per stacked layer. When the coupling between layers is turned on, then the bulk and edge states will disperse in the z-direction, but as long as the inter-layer coupling does not close the bulk gap, then the system will remain in the WTI phase with the same Hall conductance.

To further discuss the boundary modes of the topological semi-metal it useful to illustrate with an explicit lattice model. We can represent this system as a tight-binding model on a cubic lattice where each site contains a single electronic orbital with spin-up and spin-down degrees of freedom. A representative Bloch Hamiltonian is

$$H(\vec{k}) = A\sin k_x\sigma^x + A\sin k_y\sigma^y + (2B - m - B\cos k_x - B\cos k_y - C\cos k_z)\sigma^z \tag{1.10}$$

where A, B, C, m are parameters, σ^a represents spin, and we have set the lattice constant $a = 1$. If we choose the parameters $A = B = 2m = 1$ and $C = 0$, this will represent a WTI phase built from decoupled layers of Chern insulator states as discussed above. We can see this from the fact that when $C = 0$ there is no dispersion in the z-direction, and thus we have many copies of a two-dimensional system, one for each allowed k_z, i.e., one for each layer. The important point is that when A, B, m are tuned as above, then, ignoring the z-direction, the resulting two dimensional system is in a Chern insulator phase with $C_1 = 1$ [75], and thus we have decoupled copies of a non-trivial Chern insulator. When the tunneling between the layers is activated, the parameter C will be non-vanishing. With A, B, m fixed as above then for $-1/2 < C < 1/2$ the model will remain in the WTI phase. At $C = 1/2$ the bulk energy gap closes at $\vec{k} = (0, 0, \pi)$. If C is further increased then there will be two points where the gap vanishes, i.e., two Weyl-nodes, and they will occur at $\vec{k} = \left(0, 0, \cos^{-1}\left(-\frac{m}{C}\right)\right)$ where we added the dependence for a variable m parameter back in. Accordingly, when $|m/C| < 1$ the system will exhibit a Weyl semi-metal phase if $A = B = 1$.

As was shown in [108], we can use a model like Eq. 1.10 to create a nice description of the Weyl semi-metal phase. For this picture, it is useful to think about the system as a family of 2D insulators $H_{k_z}(k_x, k_y) \equiv H(k_x, k_y, k_z)$, parameterized by k_z. For parameters representing the fully gapped WTI phase (e.g. $A = B = 2m = 1$, $C = 0$), then for each value of k_z the 2D insulator $H_{k_z}(k_x, k_y)$ is in the Chern insulator phase.

Now, when we tune the C parameter into the Weyl semi-metal phase then the model will contain gapless Weyl-nodes at $\vec{k} = (0, 0, \pm k_c)$, and a separation vector $\vec{b} = (0, 0, k_c)$. To understand the existence of surface states in the semi-metal phase it is again helpful to think of each 2D insulator at fixed k_z being in a trivial $C_1 = 0$ phase when $|k_z| > |k_c|$ and a Chern insulator phase with $C_1 = 1$ when $|k_z| < |k_c|$. Exactly at $k_z = \pm k_c$ there is a gapless "transition" as a function of k_z between the trivial 2D insulator with $C_1 = 0$ and the non-trivial 2D insulator with $C_1 = 1$.

This illustration shows that in the Weyl semi-metal phase we should only expect boundary states to exist over a finite range of k_z, i.e., $|k_z| < |k_c|$ for this particular example. For each k_z in the topological range, the 2D insulator $H_{k_z}(k_x, k_y)$ contributes one propagating chiral fermion mode to the boundary degrees of freedom. These chiral boundary states manifest as incomplete surface Fermi-arcs that connect Weyl points in the surface Brillouin zone for surfaces with normal vectors which are not parallel with $\vec{b}$. The picture of a TSM as a momentum-space transition in a family of lower-dimensional gapped insulators is helpful because similar concepts can be applied to understand the properties of all topological semi-metals.

An entirely analogous picture exists for 2D Dirac semimetals, 3D Dirac semimetals and for 3D line-node semimetals. The surface states however are not chiral in those cases and arise from a non-zero $\mathbb{Z}_2$ invariant which changes as we go across a nodal surface. We have discussed this in detail in the appropriate chapters. This completes the basic review and motivation. To summarize, we have introduced some important physical intuition and concepts pertaining to semi-metals, and during this process reviewed some of the previous work describing the EM response and boundary states of these systems. Now we will begin a more in-depth discussion of the response and boundary states of semi-metals in 1D, 2D, and 3D.

Chapter 2

Semimetal in $1+1$-dimensions

We will begin with a careful study of the properties of a 1D TSM, which in this case is just an ordinary 1D metal, as noted in [93]. As a representative model we can choose a spinless 1-band tight-binding model of the form

$$H_{1D} = -\alpha \sum_n \left[c^\dagger_{n+1} c_n + c^\dagger_n c_{n+1}\right] \tag{2.1}$$

where the sum over n runs over all of the lattice sites, and we will let the lattice constant be a. This familiar model is easy to diagonalize and the energy spectrum is:

$$E(k) = -2\alpha \cos ka \tag{2.2}$$

where $k \in [-\pi/a, \pi/a)$. In the momentum basis the Hamiltonian is just $H_{1D} = \sum_k E(k) c^\dagger_k c_k$.

Establishing a chemical potential μ that lies within the band will fill the system with a finite density of electrons. If we retain translation symmetry, we can calculate the number of particles by counting the number of occupied momentum states

$$N = \sum_{k \in occ.} 1 = \frac{L}{2\pi} \int_{-k_F}^{k_F} dk = \frac{L k_F}{\pi} \tag{2.3}$$

which implies a charge density $\rho = e\frac{k_F}{\pi}$ where k_F is the Fermi wavevector and e is the electron charge. In the language of the previous section we note that this density breaks Lorentz invariance because it establishes a preferred frame, i.e., the rest-frame of the fermion density. Thus, we should expect a Lorentz-violating contribution to the effective action. In fact, we can easily write down this contribution since a background charge density just couples to the scalar EM potential A_0 to give a potential energy term

$$S[A_0] = -\int dx dt \rho A_0. \tag{2.4}$$

In addition to the density, there is the possibility of introducing an electric current that will also break

Lorentz invariance. For a moment, let us consider a generic one-dimensional lattice model with translation invariance, and in the momentum basis. When minimally coupled to an EM field (e.g., through Peierls substitution) we find

$$H = \sum_k c_k^\dagger H(k - \tfrac{e}{\hbar} A_1) c_k \tag{2.5}$$

where $H(k)$ is a Bloch Hamiltonian. The current for this system in the limit $A_1 \to 0$ is given by

$$j = \lim_{A \to 0} \frac{\partial H}{\partial A_1} = -\frac{e}{\hbar} \sum_k \left[\frac{\partial H(k)}{\partial k} n_F \right] \tag{2.6}$$

where n_F is the Fermi-Dirac distribution, which will be a step function at $T = 0$. This can be rewritten at zero temperature as

$$j = -e \sum_{n \in occ} \int_{BZ} \frac{\mathrm{d}k}{2\pi\hbar} \frac{\partial E_n(k)}{\partial k} \tag{2.7}$$

where n runs over the occupied bands. Specializing to the case of our single-band model, the current is equal to $j = -\frac{e}{2\pi\hbar}(E(k_F) - E(-k_F))$ which is non-zero only if $E(k_F) \neq E(-k_F)$. We will discuss two different mechanisms for generating a current in Sections 2.1 and 2.2.

2.1 1D model in an electric field

One way to generate a non-zero electric current is to apply an external electric field. We will apply an electric field by adiabatically threading magnetic flux through the hole of the periodic lattice ring via Faraday's law. This is equivalent to introducing twisted boundary conditions on the wave functions

$$\Psi(x + L) = e^{i\Phi(t)L} \Psi(x) \tag{2.8}$$

where

$$\Phi(t) = \frac{eEt}{\hbar} \tag{2.9}$$

for an electric field E at time t. Using Eq. 2.7 we can easily calculate the electric current to be

$$j = \frac{2\alpha e}{\pi\hbar} \sin(k_F a) \sin(\Phi(t) a). \tag{2.10}$$

For comparison, we numerically calculate the charge density and current for the case when the single band is half-filled. At half-filling $k_F = \pi/2a$, and thus the density should be uniform, time-independent and equal to $\rho = \frac{e}{2a}$, i.e., half an electron per site. At half filling, the current reduces to $j = \frac{2\alpha e}{\pi\hbar} \sin(\Phi(t)a)$. The

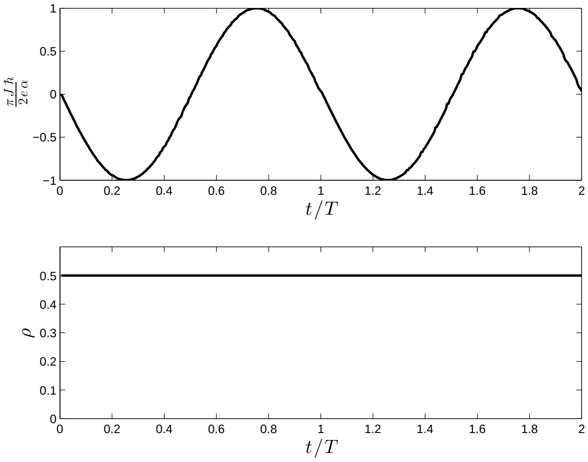

Figure 2.1: The current and charge density of the 1D (semi-)metal are plotted vs time for half filling and for nearest neighbor hopping $\alpha = 1$. The current has a periodic response as expected with a period of 200 time slices for an electric field of strength $E = \frac{h}{eT(200a)}$ for some time-scale T that is long. The charge density is given by $\rho = e\frac{k_F}{\pi} = e/2a$ as expected and shows no time dependent behavior.

numerical calculations are shown in Fig. 2.1, and they agree with the analytic results.

We note in passing that for finite-size lattice models some care must be taken to correctly calculate a smooth electric current response. We have intended to calculate the current of a metallic/gapless system, but there are finite-size gaps in the energy spectrum between each state separated by $\Delta k = 2\pi/L$. Thus, if we want the system to behave as a gapless system should, we must apply a minimum threshold electric field. If too small of an electric field is applied at a given system size, the model will behave like a gapped insulator instead. To avoid this we can simply enforce the canonical momentum $\Pi_x = p_x - eA_1$ to be a multiple of $2\pi\hbar/L$ so that the system remains gapless at each time step. If this is not done, then the system will behave as gapped insulator and we will see steps in the current response. Ensuring that $\frac{e}{\hbar}A_1 = \frac{2\pi m}{L}$ at every time step saves us this trouble, and in our simulations for this section we have always taken $\Phi(t) = eEt/\hbar$ to be a multiple of $2\pi/L$ and never smaller than this value. Physically we understand that, for a system with these finite-size gaps, an infinitesimal adiabatic current-generation will not work. Instead we must turn on a large enough electric field so that there is some non-adiabaticity so that the finite-size gaps can be overcome.

Although we do not present the results here, we have carried out numerical calculations for various filling factors and electric field strengths, and the analytic results match the numerical simulations. If we change the boundary conditions from periodic to open then the charge density remains the same (possibly up to some damped density oscillations near the ends of the wire), but the current vanishes as expected. Hence, we see that in the presence of an electric field with periodic boundary conditions the response action of the

1D (semi-)metal is

$$S[A_\mu] = \int dxdt\,[-\rho A_0 + jA_1] = \int dxdt j^\mu A_\mu \tag{2.11}$$

where $j^\mu = (\rho, j)$, which in our convention already has the electric charge factored in. Other than the presentation, most of what we have done here is elementary, we are just using these results to set the stage for the later sections.

Now, we can re-write the action in a few suggestive ways. First we can define a new 2-vector

$$b_\mu = \frac{\pi}{e}\,(j, \rho) \tag{2.12}$$

such that the action can be re-written

$$S[A_\mu] = \frac{e}{\pi}\int dxdt \epsilon^{\mu\nu} b_\mu A_\nu. \tag{2.13}$$

This is to be compared with Eq. 1.6. Alternatively we can define an axion-like field

$$\begin{aligned} \theta(x,t) &\equiv 2b_\mu x^\mu = \frac{2\pi}{e}(\rho x - jt) \\ &= 2k_F x - \frac{4\alpha}{\hbar}\sin(k_F a)\sin(\Phi(t)a)t, \end{aligned} \tag{2.14}$$

and if the system is homogeneous with no boundaries, we can use $\theta(x,t)$ to rewrite Eq. 2.11 as

$$S[A_\mu, \theta] = -\frac{e}{4\pi}\int dxdt\,\theta(x,t)\epsilon^{\mu\nu}F_{\mu\nu}. \tag{2.15}$$

As mentioned in Section 1.1, using $\theta(x,t)$ breaks space-time translation symmetry due to the arbitrary choice of origin, and thus we must be careful to specify that the system is translation invariant when writing down Eq. 2.15, otherwise spurious response terms will be generated at boundaries and interfaces. Physically we can interpret $\frac{e\theta}{2\pi}$ as the charge polarization since its space and time derivatives are proportional to the charge density and current respectively.

While this method of generating an electric current came from an external effect, i.e. an externally applied electric field, we now move on to a discussion of an intrinsic effect that can produce a current in the absence of an external electric field.

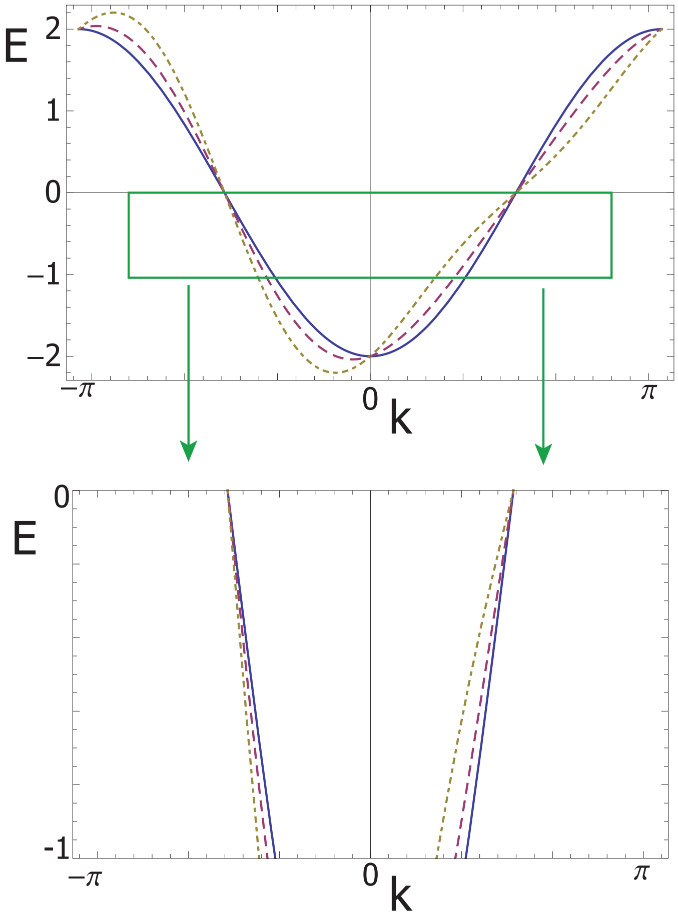

Figure 2.2: (upper) Energy spectrum of the Hamiltonian H_{1Dv} where each curve represents a different value of β. The solid blue line is $\beta = 0$, the magenta dashed line is $\beta = 0.1$ and the dash-dotted tan line is $\beta = 0.25$. All curves have $\alpha = 1$. (lower) This is a zoomed in region of the upper figure slightly below half-filling, which is the regime for our calculation. Exactly at half-filling β has no effect, and the stronger β is, the more the Fermi wave vectors and velocities are modified at a fixed μ.

2.2 1D Model with next-nearest-neighbor(NNN) hopping

In this section we illustrate another way to generate a non-vanishing current. For energies near the Fermi-points, the dispersion of our model is linear, and the modes near each Fermi-point are 1+1-d chiral fermions. In fact, it is well-known that there is a close connection between the physical electric current for a 1D metallic band in an electric field, and the compensating chiral anomalies of the fermion modes near each Fermi-point. The previous section explicitly dealt with these issues, albeit using a less elegant perspective, and in that case an electric current was generated by an external source of Lorentz breaking, i.e. the applied electric field. Here we would like to consider an intrinsic source of Lorentz breaking that will lead to a current as well. By considering this effect, we are trying to make an analogy to the 3D chiral magnetic effect in Weyl semi-metals, where it has been predicted that a current can appear in the presence of an applied magnetic field, but in the absence of an electric field.

The basic idea is that, for the 1D model we have chosen, the chiral fermions near the Fermi-points both have the same velocity, except for the sign, and we want to deform the velocities so that each chiral fermion has a different "speed of light." This is an obvious way to break Lorentz invariance. If the velocities are different (and the spectra were linear for all energies) then it is clear that we should have $E(-k_F) = v_L k_F \neq v_R k_F = E(k_F)$ which suggests the presence of a current. Physically, this just means that if we have 1+1-d chiral fermions with the same non-zero density, but different velocities, then there will be a non-vanishing current. Since we are in 1D, the analog of the 3D chiral magnetic effect predicts that we should find an intrinsic current without the application of a magnetic field or an electric field, and it should be proportional to the intrinsic quantity b_0. In the 3D Weyl semimetal, the number b_0 represents the energy difference between Weyl nodes and has units of frequency. A simple interpretation of the effect seen here in 1D is that a non-vanishing frequency scale b_0 will be generated by the combination of Δv_F, i.e. the velocity difference at the two Fermi points, and a length scale. In our system we have two important length scales: the lattice constant a, and the inverse of the Fermi wave vector k_F. To see which one enters the result we will perform an explicit calculation.

To generate the velocity modification effect we deform the tight binding model in Eq. 2.1 above to include imaginary next-nearest neighbor hopping terms

$$H_{1Dv} = H_{1D} + i\beta \sum_n \left[c^\dagger_{n+2} c_n - c^\dagger_n c_{n+2} \right]. \tag{2.16}$$

The Fourier transform of the Hamiltonian is given by

$$H_{1Dv} = -2 \sum_k (\alpha \cos(ka) - \beta \sin(2ka)) c^\dagger_k c_k. \tag{2.17}$$

For $\beta \neq 0$, inversion symmetry is broken in the model and subsequently we should consider two Fermi-wavevectors k_{FL} and k_{FR} where $k_{FL} \leq k_{FR}$ by definition. Exactly at half-filling $k_{FL} = -k_{FR} = \pi/2a$ for all β (as shown in Fig. 2.2). Thus the electric current is vanishing at half-filling (since $\beta \sin(2a(\pi/2a)) = 0$), and the charge density will be $\rho = \frac{e}{2a}$, i.e. the same as was found when no electric field was applied to the model H_{1D} at half-filling.

Half-filling is just a special point of this model where β has no effect because of our choice of next-nearest neighbor hopping. Instead, let us consider the case where μ is tuned slightly away from half-filling, i.e. $\mu = 0 - \delta\mu$ with $|\delta\mu| \ll \alpha$, and we will also take $|\beta| \ll \alpha$ as we want to consider the perturbative effect of turning on this term. We can define $k_{FL} = -\frac{\pi}{2a} + \epsilon_L$ and $k_{FR} = \frac{\pi}{2a} + \epsilon_R$. By expanding Eq. 2.17 around the Fermi-points we find that consistency requires

$$\epsilon_{L/R} = \pm\frac{\delta\mu}{2a(\alpha \pm 2\beta)} \approx \pm\frac{1}{2a}\frac{\delta\mu}{\alpha}\left[1 \mp \tfrac{2\beta}{\alpha}\right]. \tag{2.18}$$

Thus we can determine that

$$k_{FL/R} \approx \frac{\pi}{2a}\left[\mp 1 \pm \frac{\delta\mu}{\pi\alpha}\left(1 \mp \tfrac{2\beta}{\alpha}\right)\right] \tag{2.19}$$

and can subsequently define $\kappa_F \equiv \frac{\pi}{2a}(1 - \delta\mu/\pi\alpha)$, which would be the Fermi wavevector if $\beta = 0$. Note that the signs in the previous two equations are correlated. From Fig. 2.2 we can see that as β is increased the Fermi-wave vector at a fixed μ (different than half-filling) changes, as well as the velocity of the low-energy fermions. From Eq. 2.7, the response should be

$$\rho = e\frac{k_{FR} - k_{FL}}{2\pi} = \frac{e\kappa_F}{\pi} = \frac{e}{2a}\left(1 - \tfrac{\delta\mu}{\pi\alpha}\right) \tag{2.20}$$

$$j = \frac{2e\beta}{\pi\hbar}\sin(2\kappa_F a). \tag{2.21}$$

This result shows that we find a non-zero electric current even in the absence of an applied electric field, and its magnitude is proportional to the inversion breaking parameter β. This effect, while simple in origin, is the 1D analog of the 3D chiral magnetic effect. It represents a current proportional to an intrinsic frequency scale, but does not require the application of any external electric or magnetic fields. We do note that the definition of the frequency scale does require a non-vanishing Fermi wave-vector, i.e. a non-vanishing background density which cannot arise from a completely empty or filled band. As shown in Fig. 2.3, the numerical calculation of the electric current matches the analytic formula. The response is linear in β as expected from Eq. 2.21 and, although we do not show the charge density, it matches as well. The numerical calculations were done for slightly less than half-filling at $\kappa_F = \pi/2a - \pi/100a$.

Let us take a closer look at the generation of the electric current. The velocity of the chiral fermions at $\pm\kappa_F$ is given by $\hbar v_\pm = \pm(2\alpha a\sin(\kappa_F a) \mp 4\beta a\cos(2\kappa_F a))$, and thus,

$$\Delta v_F = \frac{8\beta a}{\hbar}\cos(2\kappa_F a). \tag{2.22}$$

For our choice of the chemical potential, $\kappa_F = \pi/2a + \delta\kappa_F$, and the current from Eq. 2.21 is approximately

$$j \approx -\frac{8e\beta}{2\pi\hbar}\delta\kappa_F a = -\frac{e}{2\pi}\frac{8\beta a}{\hbar}\delta\kappa_F = \frac{e}{2\pi}\Delta v_F\delta\kappa_F. \tag{2.23}$$

where we used that near $\kappa_F = \pi/2a$ we have $\Delta v_F \approx -\frac{8\beta a}{\hbar}$. Thus $\Delta v_F\delta\kappa_F$ gives a Lorentz-breaking frequency

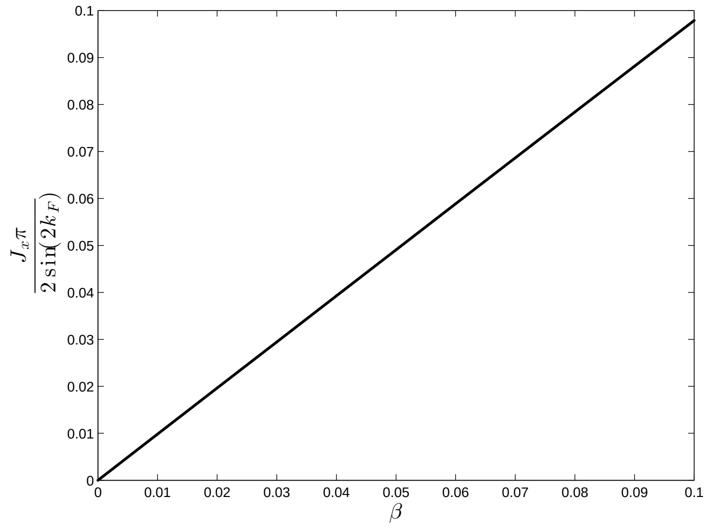

Figure 2.3: The current of H_{1Dv} is plotted vs next-nearest neighbor hopping strength β near half filling. $\kappa_F = \pi/2a - \pi/100a$ was chosen and the nearest-neighbor hopping $\alpha = 1$ with periodic boundary conditions. The current increases linearly as a function of β as expected from Eq. 2.21. Note we have let $a = \hbar = 1$.

scale that will give rise to a non-vanishing b_0-term in the effective response. In fact, the density and current give us the 2-vector $b_\mu = (\frac{1}{2}\Delta v_F \delta\kappa_F, \kappa_F)$ which determines the response action

$$S[A_\mu] = \frac{e}{\pi}\int dxdt\epsilon^{\mu\nu}b_\mu A_\nu. \tag{2.24}$$

To draw an analogy with the previous literature on the Weyl semi-metal response we could also define a $\theta(x,t)$ by

$$\begin{aligned}\theta(x,t) &= \frac{2\pi}{e}(\rho x - jt) = 2\kappa_F x - \frac{4\beta}{\hbar}\sin(2\kappa_F a)t \\ &\approx 2\kappa_F x - \Delta v_F \delta\kappa_F t\end{aligned} \tag{2.25}$$

which couples into the action

$$S[A_\mu, \theta] = -\frac{e}{4\pi}\int dxdt\theta(x,t)\epsilon^{\mu\nu}F_{\mu\nu}. \tag{2.26}$$

2.3 Derivation of the effective response

After our explicit discussion of the different EM responses of the 1D metallic wire, let us elevate our discussion to a field-theoretic calculation. In this section, we use the Fujikawa method to derive the effective response of the low-energy continuum field theory description of the 1D metal in the presence of intrinsic sources of Lorentz invariance violation, e.g. external electromagnetic fields, momentum and velocity shifts of the nodes, and non-zero chemical potential. The derivation is similar to that for 3D Weyl semi-metals found in [114].

To carry out the calculation let us expand the lattice Bloch Hamiltonian given by $H(k) = -2\alpha\cos ka + 2\beta\sin 2ka$ around the chemical potential $\mu = 0 - \delta\mu$ for $|\delta\mu| \ll \alpha$ and $|\beta| \ll \alpha$ as in the previous section. If we expand the right and left-handed chiral branches around $\pm\kappa_F$ respectively we find the approximate continuum Hamiltonian

$$H_{cont} = \left(-\delta\mu + \tfrac{1}{2}\hbar\Delta v_F q\right)\mathbb{I} + \left(\hbar v_F q + \tfrac{1}{2}\hbar\Delta v_F\delta\kappa_F\right)\sigma^z \tag{2.27}$$

where the upper component represents the fermions near k_{FR}, the lower component represents the fermions near k_{FL}, q represents a small wavevector deviation from $k_{FL/R}$, $\hbar v_F \equiv 2a\alpha$, $\Delta v_F \equiv -\frac{8\beta a}{\hbar}$, and $\delta\kappa_F = -\frac{\delta\mu}{2a\alpha}$. The definitions of the parameters are easy to understand by looking at the lattice model in the previous section when expanded around κ_F.

Since we know the behavior of the full lattice model, i.e. the high-energy regularization of the continuum model, we can see that our expansion effectively normal orders the current and density with respect to half-filling. Since the current vanishes exactly at half-filling, the total current is simply $j = \delta j$. The current change away from half-filling is simply given by $\delta j = \frac{e}{2\pi\hbar}\left(E_R(q=0) - E_L(q=0)\right) = \frac{e}{2\pi}\Delta v_F\delta\kappa_F$, which matches the previous section, which does not include the effective normal-ordering. On the other hand, the charge density does not vanish at half-filling. The density change away from half filling is given by $\delta\rho = e\frac{-\delta\mu}{2\pi\alpha a} = e\frac{\delta\kappa_F}{\pi}$, and the full density includes the additional amount $\rho_0 = \frac{e}{2a}$ that arises from all the occupied states up to half filling. This makes the total density $\rho = \rho_0 + \delta\rho = e\frac{k_{FR}-k_{FL}}{\pi}$ as expected. However, if we are just given the continuum model, without reference to an initial lattice model, it only has information about $\delta\rho$ and δj. We note that neither the current, nor the density, depend on the dispersion term $\frac{1}{2}\hbar\Delta v_F q\mathbb{I}$ and so we will drop it from further discussion as it is also higher order in the expansion around the Fermi-points.

From this Hamiltonian it is simple to construct the Lagrangian now using the Dirac matrices $\gamma^0 = i\sigma^x, \gamma^1 = \sigma^y$ and the chirality matrix $\gamma^3 = \sigma^z$. We find

$$\mathcal{L} = \overline{\psi}\left(i\not{\partial} - \not{b}\gamma^3\right)\psi \tag{2.28}$$

where $\not{b} = b_\mu\gamma^\mu$ for $b_\mu = \left(\frac{1}{2}\Delta v_F\delta\kappa_F, \delta\kappa_F\right)$. If we included the EM gauge field, this Lagrangian would be analogous to the Lagrangian derived for the Weyl semimetal in [114], except this is in $1+1$ dimensions. We can now get rid of the b_μ-dependent term by doing a chiral gauge transformation. As is well-known, this transformation can change the measure of the path integral and lead to anomalous terms in the effective action.

We will use the Fujikawa method to derive the effective response due to this change of measure. Performing a series of infinitesimal chiral transformations parametrized by the infinitesimal ds, we can get rid of the b_μ dependent term:

$$\begin{aligned} \psi &\rightarrow e^{-ids\theta(x)\gamma^3/2}\psi && (2.29) \\ \overline{\psi} &\rightarrow \overline{\psi}e^{-ids\theta(x)\gamma^3/2} && (2.30) \end{aligned}$$

where $\theta(x) \equiv 2b_\mu x^\mu$. Note that using this choice of $\theta(x)$ we have made an arbitrary choice of origin which is folded into the calculation. To avoid spurious response terms we need to constrain the system to be homogeneous in space-time so that each choice of space-time origin is equivalent. The Dirac operator $\not{D}$ acts as follows

$$\begin{aligned} \not{D} &= i\not{\partial} - \not{A} - \not{b}\gamma^3(1-s) && (2.31) \\ \not{D}\phi_n(x) &= \epsilon_n\phi_n(x) && (2.32) \end{aligned}$$

where A_μ is the EM gauge field, and ϕ_n are a complete set of eigenstates of the Dirac operator. Let us write out

$$\psi(x) = \sum_n c_n\phi_n(x)\,, \quad \overline{\psi}(x) = \sum_n \overline{c}_n\phi_n^*(x) \qquad (2.33)$$

where c_n are Grassman variables, and we can expand ψ in terms of ϕ_n because they are complete. Considering what the infinitesimal chiral transformation does to the c_n's, from Eq. 2.29, we see that

$$\begin{aligned} c_n' &= \sum_m U_{nm}c_m\,, \quad \overline{c}_n' = \sum_m U_{nm}\overline{c}_m && (2.34) \\ U_{nm} &= \delta_{nm} - \frac{ids}{2}\int d^2x\phi_n^*(x)\theta(x)\gamma^3\phi_m(x). && (2.35) \end{aligned}$$

The Jacobian of this transformation is $J = \det(U^{-2})$. Using the identity that $\det(U) = e^{Tr\ \log(U)}$, we see that

$$J = e^{ids\sum_n\int d^2x\,\phi_n^*(x)\theta(x)\gamma^3\phi_n(x)}. \qquad (2.36)$$

The Jacobian due to the chiral rotation thus induces a term in the effective action given by

$$\begin{aligned} S_{eff} &= \int_0^1 \mathrm{d}s \int \mathrm{d}x dt\, \theta(x) I(x) && (2.37) \\ I(x) &= \sum_n \phi_n^*(x)\gamma^3\phi_n(x). && (2.38) \end{aligned}$$

To evaluate $I(x)$, we can use the heat kernel regularization:

$$I(x) = \lim_{M\to\infty} \sum_n \phi_n^*(x)\gamma^3 e^{-\not{D}^2/M^2}\phi_n(x) \tag{2.39}$$

to arrive at the well-known result that

$$I(x) = -\frac{e}{4\pi}\epsilon^{\mu\nu}F_{\mu\nu}. \tag{2.40}$$

So, the effective action is given by

$$S_{eff}[A_\mu] = -\frac{e}{4\pi}\int \mathrm{d}^2x\, \theta(x)\epsilon^{\mu\nu}F_{\mu\nu}. \tag{2.41}$$

To remove the dependence on the arbitrary origin we can rewrite the action as

$$S_{eff}[A_\mu] = \frac{e}{\pi}\int \epsilon^{\mu\nu}b_\mu A_\nu. \tag{2.42}$$

This expression matches the result we determined from simpler calculations of the lattice model in Sections 2.1,2.2 if we replace ρ with $\delta\rho$ and j with δj.

2.4 Interfaces

Now that we have derived the EM response via two separate methods, we will put it to use in this section where we calculate the properties of interfaces across which b_μ varies. We will show that the response action in Eq. 2.42 predicts results that match numerical simulations, while the θ-term version in Eq. 2.41 gives spurious results due to boundary terms that depend on the arbitrary choice of origin embedded in $\theta(x)$. We want to emphasize that this also happens in the case of the 3D Weyl semimetal and is a generic feature. One might think that one could remove these spurious terms by adding boundary degrees of freedom, however the spurious results to which we refer do not seem to be connected to any anomalies as they can appear on surfaces which do not exhibit gapless boundary modes.

The form of the action to use when studying inhomogeneous systems (i.e., with relaxed translation invariance) is

$$S[A] = \frac{e}{\pi} \int d^2x \, \epsilon^{\mu\nu} b_\mu A_\nu. \tag{2.43}$$

One might complain that this action appears gauge-variant, however, it is not. We note that we can define a current $j^\mu_{(b)} = \frac{e}{\pi}\epsilon^{\mu\nu} b_\nu$. Therefore, the action itself can be written $S = \int d^2x \, j^\mu_{(b)} A_\mu$. If the current is conserved then the action is gauge invariant due to the continuity equation. For the 1D metal, the current $j^\mu_{(b)}$ is exactly the EM charge current and thus is conserved yielding a gauge-invariant response functional.

Now, for the first example of an interface, suppose our 1D metal lies in the spatial region $x > x_0$, and there is only vacuum for $x < x_0$. We model this by choosing $b_\mu(x) = b_\mu \Theta(x - x_0)$ where $\Theta(x)$ is the step-function, and for simplicity we only turn on a non-vanishing b_1. If we look at the charge density the response action would predict, we find

$$\rho(x) = \frac{e}{\pi} b_1 \Theta(x - x_0) \tag{2.44}$$

which is physically correct since the metallic region will have a density equal to this value, and the vacuum will have no density. If we had used the axion-action with $\theta(x,t) = 2b_1(x - x_1)$ for some arbitrary constant value x_1 we would have obtained the density

$$\begin{aligned} \bar{\rho}(x) &= \frac{e}{2\pi}\partial_x \theta(x,t) = \frac{e}{\pi} b_1 \partial_x ((x - x_1)\Theta(x - x_0)) \\ &= \frac{eb_1}{\pi}\left[(x_0 - x_1)\delta(x - x_0) + \Theta(x - x_0)\right]. \end{aligned} \tag{2.45}$$

This predicts a spurious boundary charge located at the interface x_0 and proportional to the distance between the boundary point and our *arbitrary* choice of x_1. This term is clearly unphysical, and simulations show that there is nothing special happening at the interface. Thus, the first action reproduces the correct response and matches numerics for the 1-band lattice metal.

For a more complicated illustration, consider an interface between two different systems such that b_1 is non-vanishing in both, and varies in the x-direction. This will give an x-dependent charge density. A simple way to implement an x-dependent b_1 is to introduce an on-site energy term which is x-dependent. If we had a translationally invariant 1D lattice model with a fixed chemical potential μ, then shifting the onsite energy up or down will decrease or increase the electron density respectively. Let us consider two 1D segments which have a common boundary. Suppose the onsite energies are constant within each region, but are offset between the two regions by ϵ_0. To simplify the description we assume that they are glued periodically so, in fact, there are two interfaces.

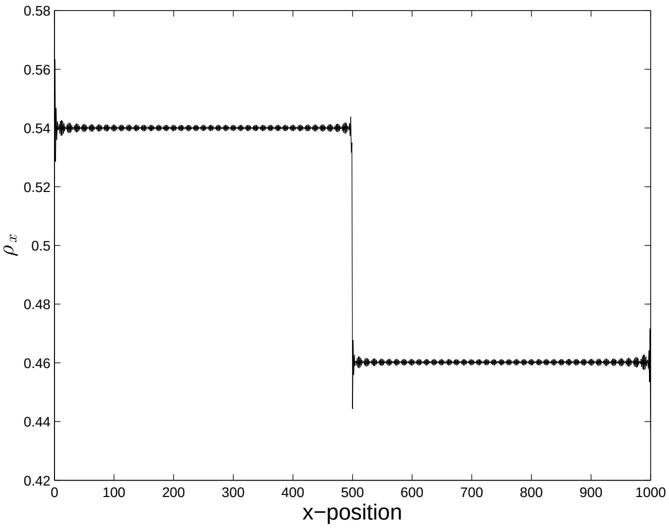

Figure 2.4: Charge density in units of e/a as a function of position for an inhomogeneous system with $N = 1000$ lattice sites where each segment has $L_s = 500$ sites. The chemical potential is $\mu = 0$, and if ϵ_0 was tuned to zero the density would be $\rho = e/2a$. For our choice of $\epsilon_0 = 0.5t$ we have $b_{1(\ell)} = (\pi/a)0.46$, $b_{1(r)} = (\pi/a)0.54$. Away from the interfaces the values match the calculation from the effective response action. Near the interfaces there are damped oscillations due to finite size effects that are not captured by the analytic calculation. Note that the finite-size boundary effects have nothing to do with the spurious "interface"-terms in Eq. 2.45.

For an analytically tractable limit, let us study the case when the offset is not too big when compared to the bandwidth of the system, and with the chemical potential fixed at $\mu = 0$. The Hamiltonian is given by

$$H = -t \sum_n \left[c^\dagger_{n+1} c_n + c^\dagger_n c_{n+1} \right] + \sum_n \epsilon(n) c^\dagger_n c_n \tag{2.46}$$

where $\epsilon(n) = \pm\epsilon_0/2$ when $n \leq N/2$ or $n > N/2$ respectively for a system with an even number of sites N. We want to understand what happens to the charge density in the system, and compare it to what is predicted by the EM response action. With this Hamiltonian the system consists of two segments (labelled by ℓ and r), each of length $L_s = Na/2$ where a is the lattice constant.

We can now compute what $b_{1(\ell)}$ and $b_{1(r)}$ are for each segment since there is a simple relation between charge density and b_1. As the length of the segments approaches the thermodynamic limit, the average charge density will not depend on whether we calculate it with open or periodic boundary conditions, so for simplicity we can calculate the density with periodic boundary conditions for each segment separately. With $\mu = 0$ fixed, the Fermi momentum for the segment ℓ with the offset $+\epsilon_0/2$ is given by

$$0 = \epsilon_0/2 - 2t\cos(k_{F,\ell}a) \implies k_{F,\ell} = \frac{1}{a}\cos^{-1}\left(\frac{\epsilon_0}{4t}\right). \tag{2.47}$$

The Fermi momentum for system r is given by

$$0 = -\epsilon_0/2 - 2t\cos(k_{F,r}a) \implies k_{F,r} = \frac{1}{a}\cos^{-1}\left(\frac{-\epsilon_0}{4t}\right). \tag{2.48}$$

So, we have $\rho_r = e\frac{k_{F,r}}{\pi}$ and $\rho_\ell = e\frac{k_{F,\ell}}{\pi}$ which by definition implies that $b_{1(r/\ell)} = (\pi/e)\rho_{r/\ell} = k_{Fr/\ell}$. Explicitly we have

$$\begin{aligned} b_{1(\ell)} &= \frac{1}{a}\cos^{-1}\left(\frac{\epsilon_0}{4t}\right) && (2.49)\\ b_{1(r)} &= \frac{1}{a}\cos^{-1}\left(\frac{-\epsilon_0}{4t}\right). && (2.50)\end{aligned}$$

In our geometry we have interfaces at $x = L_s$ and $x = 2L_s \equiv 0$ and b_1 varies across the interfaces. The EM response action predicts

$$\begin{aligned} \rho &= \frac{e}{\pi}\left[b_{1(\ell)}(\theta(x) - \theta(x - L_s))\right.\\ &+ \left. b_{1(r)}(\theta(x - L_s) - \theta(x - 2L_s))\right]. && (2.51)\end{aligned}$$

This result matches what is found numerically as shown in Fig. 2.4.

2.5 General comments

Before we move on to discuss the more interesting higher dimensional semi-metals, we will pause to make a few important comments.

(i) Response Action Without Translation Invariance: Initially we parameterized the EM response of the 1D metal through quantities such as the Fermi-wave vector, and the velocity at the Fermi-points, which can only be clearly defined when there is translation symmetry. That is, when the system is homogeneous we can precisely define momentum space and these two quantities. What we have found is that the response is actually more general because we can define it in terms of the sources of Lorentz violation, i.e. an intrinsic charge density and charge current. These two physical quantities can be defined, and measured, without reference to momentum space and thus we can drop all reference to a Fermi wave vector and a Fermi velocity by using the density and current respectively. The fact that the EM response is accurate even without translation invariance is clearly shown when we have an interface as shown in the previous section.

This physical definition of the response is special to 1D because the semi-metal EM response action is just $\int d^2x j^\mu A_\mu$. This type of term will appear in every dimension, but in higher dimensions there are more interesting anisotropic response terms that appear and which we will discuss later. For d-dimensional space-time we can introduce a $(d-1)$-form $b_{\mu_1\mu_2\ldots\mu_{d-1}}$ representing a source of Lorentz breaking. We can furthermore take the dual to generate a current $j^{\mu}_{(b)} = \epsilon^{\mu\mu_1\cdots\mu_{d-1}} b_{\mu_1\mu_2\ldots\mu_{d-1}}$ which represents an intrinsic charge density or charge current which couples to A_μ minimally. This term yields the higher dimensional analog of the 1D semi-metal EM response. We comment later on the possibility to represent higher dimensional response actions without reference to momentum space.

(ii) Response of Filled bands: As is well-known from elementary solid-state physics, a filled band of electrons in a crystal carries no current. Each filled band also contributes a charge density $\rho_{band} = \frac{e}{a}$ or e/Ω where Ω is the size of a unit cell in higher dimensions. The EM response actions of topological semi-metals do not capture density or current contributions from filled bands and thus the response coefficients are ambiguous by a finite quantized amount, i.e., b_μ is ambiguous by the addition of half of a reciprocal lattice vector.

(iii) Symmetries of b_μ in 1D: Let us discuss the transformation properties of b_μ under time-reversal (T), charge-conjugation (C), and inversion symmetry (P). Since in 1D we know that b_0 is proportional to a current and b_1 is proportional to a density we can easily determine their symmetry properties:

$$\begin{aligned} T &: \quad b_0 \to -b_0 \\ C &: \quad b_0 \to b_0 \\ P &: \quad b_0 \to -b_0 \end{aligned} \tag{2.52}$$

and

$$\begin{aligned} T &: \quad b_1 \to b_1 \\ C &: \quad b_1 \to b_1 \\ P &: \quad b_1 \to b_1. \end{aligned} \tag{2.53}$$

Note that they are both even under C which is due to the fact that our convention for b_μ defined in terms of the density and current has the electric charge factored out. Subsequently, the response actions will have factors of electric charge in their normalization coefficients. Note that these symmetry properties only hold in 1D because the transformation properties of b_μ under these discrete symmetries are dimension dependent.

(iv) Connection between 1D and 3D Semi-metals: As mentioned in Section 1.1, the effective response for

a 3D Weyl-semi-metal is

$$S[A_\mu] = -\frac{e^2}{2\pi h}\int d^4x \epsilon^{\mu\nu\rho\sigma} b_\mu A_\nu \partial_\rho A_\sigma. \tag{2.54}$$

To be explicit, consider a system where $b_\mu = (b_0, 0, 0, b_z)$ in the presence of a uniform magnetic field $F_{xy} = -B_0$. In this case the action reduces to

$$\frac{e^2\Phi}{\pi h}\int dtdz\, \epsilon^{ab} b_a A_b = N_\Phi \frac{e}{\pi}\int dtdz\, \epsilon^{ab} b_a A_b \tag{2.55}$$

where $\Phi = -B_0 L_x L_y$ is the magnetic flux and $a, b = 0, z$. From this we see that the 3D action, for this arrangement of b_μ and $F_{\mu\nu}$, reduces to $N_\Phi = |\Phi/(h/e)|$ copies of the 1D action. This connection hints that it could be possible to define the response of the 3D Weyl semi-metal without reference to momentum space, and instead only using physical quantities, e.g., the charge density and current in a uniform magnetic field. It also shows why the symmetry transformation properties of b_μ in 1D are different than those of b_μ in 3D because of the additional factor of Φ in 3D which is odd under time-reversal. We will discuss this more in the section on 3D semi-metals.

Chapter 3

Dirac semimetal in $2 + 1$-dimensions

After our discussion of the simple 1-band metal, we will now move on to a discussion of the 2D Dirac semimetal that has become widely recognized with the experimental discovery of graphene [12]. Graphene is a honeycomb lattice of carbon atoms with a low-energy electronic structure consisting of four Dirac points. These four Dirac points are located in spin-degenerate pairs at the special points K and K' in the hexagonal Brillouin zone. For models like graphene, with both time-reversal and inversion symmetry, the minimum number of Dirac points that can appear in a 2D lattice model is two. Graphene has twice this amount because of the spin-1/2 degeneracy of the electrons due to the time-reversal symmetry with $T^2 = -1$. For our purposes, we will focus on a reduced case of spinless (or spin-polarized) electrons for which (effectively) $T^2 = +1$. To recover results for graphene one could trivially add in the degenerate spin degree of freedom. Later in this section we will discuss a general (even) number of Dirac nodes, but we will always assume they are non-degenerate, for simplicity.

This chapter is organized as follows: (i) we first discuss the construction of weak topological insulators, and subsequently, Dirac semi-metals from wire-arrays of 1D topological insulators; (ii) using the connection to the weak TI state we conjecture a form for the electromagnetic response of a Dirac semi-metal with two nodes, discuss the required symmetries for the robustness of this response, and show that a simple model yields the predicted physical properties; (iii) we derive the conjectured quasi-topological response effective action in the continuum limit using two Dirac nodes; (iv) we provide a physical interpretation of the response action in terms of known electromagnetic quantities, and we discuss the general measurable properties; (v) we discuss the generalization of the continuum calculation to lattice models and an arbitrary (even) number of Dirac nodes; (vi) finally we make some general comments on the nature of the quasi-topological response, the similarities and differences between responses in even and odd space-time dimensions, and connect the results to the properties of Chern insulator with non-zero charge polarization.

3.1 Dirac semi-metal from layered topological insulators

3.1.1 Topological insulator in 1D protected by C or P symmetry

As discussed in Section 1.1, each TSM can be constructed from a collection of lower dimensional TIs which are stacked and then coupled; the Dirac semi-metal (DSM) is no different. To generate a DSM this way we must begin with 1D TI wires. From the classification of 1D TIs we know that to have a robust, non-trivial 1D topological phase we must require the presence of a symmetry to protect the state [75, 82, 57]. This is inherently different than the 3D Weyl semi-metal, which is constructed from stacks of 2D Chern insulators that require no symmetry to have a protected topological phase[1]. There are two possibilities for an appropriate 1D TI symmetry: (i) charge-conjugation symmetry (C) or (ii) inversion/reflection symmetry (P). For C-symmetry the 1D topological wire lies in class D of the Altland-Zirnbauer classification [1, 82, 75], and there is a $\mathbb{Z}_2$ topological invariant that controls the EM response. While, in principle there is no problem with considering insulators with C-symmetry, in practice such a symmetry is approximate and/or fine-tuned. For P-symmetry the wire belongs to the set of inversion-symmetric insulators, and also has a $\mathbb{Z}_2$ topological invariant [111, 94, 47, 72]. In both cases we will call the invariant $\mathcal{Z}_{1D}$. If $\mathcal{Z}_{1D}$ takes its trivial (non-trivial) value $\mathcal{Z}_{1D} = +1(\mathcal{Z}_{1D} = -1)$ then the insulator will have a bulk charge polarization of $P_1 = ne \text{ mod } \mathbb{Z}\text{e}(P_1 = (n + 1/2)e \text{ mod } \mathbb{Z}\text{e})$, and will exhibit an even (odd) number of low-energy fermion bound-states on each boundary point. Let us note that we will use P to label reflection symmetries (inverting a single coordinate) and $\mathcal{I}$ to represent inversion symmetry (reflection in all coordinates). Of course in 1D they are the same, so we will simply use P for 1D systems.

Since it will become important, let us review the EM response of the 1D TI. The response is captured by the effective action

$$S_{eff}[A_\mu] = \frac{1}{2}\int d^2x P_1 \epsilon^{\mu\nu} F_{\mu\nu} \tag{3.1}$$

where P_1 depends on the insulating phase as given above. The requirement of either C or P symmetry enforces a quantization of the polarization in units of half an electron charge [111, 75, 94, 47]. Naively these symmetries should forbid a non-zero P_1 since $P_1 \to -P_1$ under C or under P. However, since the polarization in 1D crystalline insulators is only well-defined modulo integer charge, the allowed values of P_1 are 0 and $e/2$, which both satisfy $P_1 = -P_1$ modulo integer electron charges [56, 75]. Another way to say this is that 1D insulators with polarizations that differ by an integer electron charge are topologically equivalent (or stable topologically equivalent).

---

[1] To be more precise, Chern insulators require a global $U(1)$ charge conservation symmetry for protection, but we will not consider the possibility of superconducting systems.

It will be very useful to have an explicit system in mind when discussing the features of the 1D TI, and the subsequent weak TI and 2D Dirac semi-metal generated by stacking the 1D TIs. Thus, let us choose a simple model which exhibits a 1D TI phase: the 1D lattice Dirac model. For translationally invariant systems, this model has a Bloch Hamiltonian

$$H_{1DTI}(k) = (A \sin ka)\sigma^y + (B - m - B \cos ka)\sigma^z \tag{3.2}$$

where A, B, m are model parameters (we set $A = B = 1$ from now on), a is the lattice constant, and σ^α are the Pauli matrices representing some degrees of freedom within the unit cell. The phases of this model are controlled by the parameter m, and for $m < 0$, or $m > 2$, the system is a trivial insulator with $\mathcal{Z}_{1D} = +1$. For $0 < m < 2$ the system is in a TI phase with $\mathcal{Z}_{1D} = -1$. A benefit of this model is that we can judiciously choose a C operator and a P operator such that the Hamiltonian has that symmetry. For example, if we pick $C = \sigma^y$, then $CH_{1DTI}(k)C^{-1} = -H^*_{1DTI}(-k)$, and if we pick $P = \sigma^z$ then $PH_{1DTI}(k)P^{-1} = H_{1DTI}(-k)$. So, as written, this model is simple enough to have both C and P symmetry, and thus can exhibit a protected topological phase. If we add perturbations to the model that break one of the symmetries, but preserve the other, then the topological phase will remain stable. It is only if we break both symmetries that we can destabilize the 1D TI phase.

Usually, for insulators, a C-symmetry only exists when the model is fine-tuned, but inversion/reflection symmetry can be approximately preserved in real materials. In what follows we will emphasize the inversion or reflection symmetric cases as it is more relevant when considering semi-metal phases that might be realized in materials. We note that this model also has time-reversal symmetry with $T = K$ ($T^2 = +1$). Although this symmetry is not important for the 1D classification, it will become important when we discuss the 2D semi-metal phase.

3.1.2 Weak topological insulator in 2D protected by C, P, or $\mathcal{I}$ symmetry

Before we approach the DSM let us consider the 2D WTI phase generated by stacking a weakly-coupled set of 1D TI wires. To be explicit, suppose that the wires are oriented parallel to the x-axis and stacked perpendicularly to spread into the y-direction. In the limit of decoupled wires, we can determine that the system will have a charge polarization in the x-direction, and will have low-energy boundary states on boundaries with a normal vector in the x-direction (or, in general, on boundaries not parallel to the y-axis). In this limit, a 2D Hamiltonian representing this phase is just multiple copies of H_{1DTI} with a fixed value of $0 < m < 2$ for each wire. These distinguishing topological characteristics remain as long as the coupling between the wires does not close the bulk gap, and as long as the relevant symmetries of the 1D TI are preserved.

We can model this using a square-lattice Bloch Hamiltonian

$$H_{2DWTI}(\vec{k}) = \sin(k_x a)\sigma^y + (1 - m - \cos(k_x a) - t_y \cos(k_y a))\sigma^z \tag{3.3}$$

for a lattice constant a, and a new tunneling parameter t_y. Again, this model has both C and P_x symmetry (reflection with $x \to -x$), with the same operators as above, since the inter-wire tunneling term $-t_y \cos(k_y a)\sigma^z$ preserves both. It also has time-reversal symmetry $T = K$, reflection symmetry in the y-direction with $P_y = \mathbb{I}$, and inversion symmetry with $\mathcal{I} = \sigma^z$. If we pick $0 < m < 2$ then the model remains in the WTI phase as long as no solutions for at least one of

$$\begin{aligned} \cos(k_y a) &= -\frac{m}{t_y} \\ \cos(k_y a) &= \frac{2-m}{t_y} \end{aligned} \tag{3.4}$$

can be found. We immediately see that as long as $|t_y| < |m|$ and $|t_y| < |(2-m)|$, then the system will be gapped, and if additionally $0 < m < 2$, the model will be in the WTI phase.

This WTI is characterized by a 2D topological vector invariant $\vec{\nu} = \left(0, \frac{\pi}{a}\right)$, which is a half-reciprocal lattice vector. The EM response of the 2D WTI depends on this vector and is given by

$$S_{eff}[A_\mu] = \frac{e}{4\pi} \int d^3x\, \nu_\mu \epsilon^{\mu\nu\rho} F_{\nu\rho} \tag{3.5}$$

where $\nu_0 = 0$. This response represents the contribution of a charge polarization $\vec{P}_1$ to the action where $P_1^i = \frac{e}{2\pi}\epsilon^{ij}\nu_j = (\frac{e}{2a}, 0)$. The magnitude of the polarization is due to a contribution of a 1D polarization of $e/2$ (and $e/2$ boundary charge) per wire, as expected, and the total charge on a boundary with normal vector $\hat{x}$ will be $N_y \frac{e}{2}$ where N_y is the number of wire layers. As discussed in Section 1.1, the WTI phase does not give rise to ν_0 because there is no effective Lorentz-breaking in the time-direction for a filled band. One could generate a ν_0 in an insulator by applying a time-dependent periodic field to generate Floquet dynamics, or perhaps by coupling the system to a varying adiabatic parameter that will drive cyclic adiabatic charge pumping [92]. For the latter, this will drive a constant, quantized current along the wires which will result in a non-vanishing ν_0 proportional to the charge pumping frequency. We will prove below that, just like ν_i is connected to the intrinsic charge polarization, ν_0 is related to the intrinsic magnetization, which is why producing currents will generate such a term.

3.1.3 From 2D weak topological insulator To Dirac semi-metal

We will now give an explicit example of a Dirac semi-metal, and in Section 3.2 we will discuss its physical response properties and characteristics. We will then move on to deriving the results for a generic Dirac semi-metal in the subsequent sections.

It is easy to construct an explicit example of a DSM phase from the WTI model we have been using by choosing m and t_y such that at least one of Eq. 3.4 has a solution. To be concrete, let $m = 1/2, t_y = -1$, and $a = 1$, for which $\cos k_y = -m/t_y$ has two solutions: $\pm k_{yc} = \pm\pi/3$, which implies there are Dirac points at $\vec{k} = (0, \pm k_{yc})$. If we expand the Hamiltonian in Eq. 3.3 around these points, we find the continuum Hamiltonians

$$H_{2Dcon} = \delta k_x \sigma^x \pm \frac{\sqrt{3}}{2}\delta k_y \sigma^z \tag{3.6}$$

which are anisotropic Dirac points with δk_x the deviation from $k_x = 0$, and δk_y the deviation from $k_y = \pm k_{yc}$. If we tuned the velocity parameter A in Eq. 3.2 to be $\sqrt{3}/2$ we would find isotropic Dirac points. In Fig. 3.1 we show the energy spectrum of this model, at the parameter values given above, in a strip/cylinder geometry with open boundary conditions in the x-direction, and periodic boundary conditions in the y-direction. We see the Dirac points at the predicted values, and also a flat-band of mid-gap states which are exponentially localized on the edges of the strip.

Despite some superficial differences, the square-lattice model for the DSM captures the same physics as the honeycomb-lattice graphene model. In fact, in Appendix A.1 we show that our square lattice model for the DSM can be continuously deformed to the honeycomb graphene model, and thus we can easily consider graphene to be constructed from layers of 1D TIs if we trivially add spin degeneracy. This matches the well-known result that graphene has anisotropic boundary states that appear only on zig-zag edges and not arm-chair edges, which is a consequence of this layered structure, and the close connection to the WTI model of stacked 1D TIs [12].

3.2 Motivation of quasi-topological Response of 2D Dirac semi-metals

Following the general discussion in Section 1.1, when the DSM is formed, we expect the quasi-topological electromagnetic response to be dependent on the momentum and energy differences between the Dirac nodes. In this sub-section we will present a form of the quasi-topological response that is analogous to Eq. 3.5 for the weak TI, and we will provide physical evidence that our conjecture is correct. In Section 3.3 we will derive the result more systematically.

For our explicit choice of parameters we should have a separation vector $b_\mu = (0, 0, \pi/3)$. As we will prove in Section 3.3, one contribution to the EM response is the analog of Eq. 3.5 for the WTI phase, that is:

$$S_{eff}[A_\mu] = \frac{e}{4\pi}\int d^3x\, b_\mu \epsilon^{\mu\nu\rho} F_{\nu\rho}. \tag{3.7}$$

From the interpretation of the 2D WTI response above, this implies a non-zero charge polarization

$$P_1^i = -\frac{e}{2\pi}\epsilon^{ij} b_j. \tag{3.8}$$

We warn that when there are multiple pairs of nodes, one must be careful when constructing the value of b_i that enters the response due to the $\mathbb{Z}_2$ nature of the polarization. We will discuss this in detail in Section 3.5, but for now we will continue analyzing the simplest case with only two nodes.

3.2.1 Charge polarization in a 2D Dirac semi-metal

Let us now try to understand the origin of the polarization. To illustrate this, we should heuristically view the DSM model Hamiltonian as representing a family of 1D insulators, parameterized by the values of k_y. That is, each value of k_y (except $k_y = \pm k_{yc}$) represents a 1D insulating wire; in the model we have picked the wires are effectively oriented in the x-direction. From our model we see that the 1D wires with k_y values on opposite sides of a Dirac point have opposite values of $\mathcal{Z}_{1D}$, and thus their contributions to the overall charge polarization differ by a quantized amount. We already know that for the completely gapped WTI phase, each wire contributes $e/2$ boundary charge (modulo ne) to an edge normal to the x-axis. In comparison, it is clear that for the DSM only the fraction of the wires between the Dirac nodes contribute $e/2$, while the remainder contribute charge $0(\mod e)$.

We can also see that, physically, the bulk polarization manifests as an observable bound charge on the sample edges. In Fig. 3.2 we show the charge density as a function of position along the open boundary direction for the cylinder geometry mentioned above (see Fig. 3.1). We have subtracted off the average background charge, and two peaks in the charge density can be seen; one on each end of the sample. The amount of charge localized on each end matches the charge density calculated from Eq. 3.7 at an interface where the polarization changes from $P_1^x = -\frac{e}{2\pi}\frac{\pi}{3a} = -\frac{e}{6a}$ to zero (we have temporarily restored the lattice constant). More convincingly, in Fig. 3.3 we show the numerically calculated boundary charge values versus the analytically predicted value of the polarization/boundary-charge over a range of values of m in our square lattice model. The numerical and analytic results match almost exactly except near $m = 1$ where

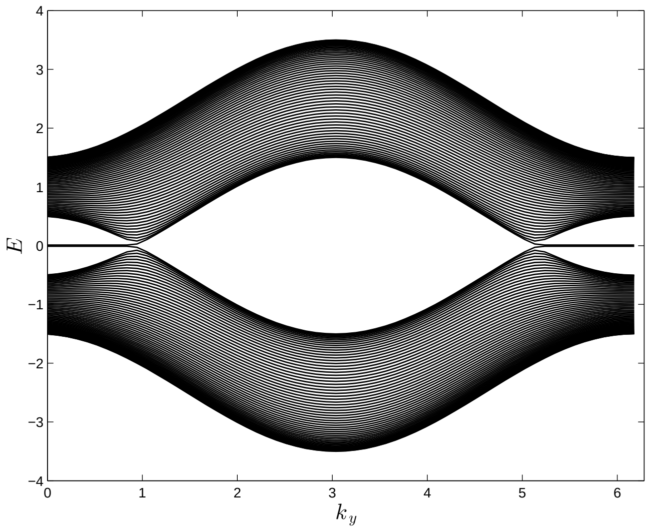

Figure 3.1: The energy spectrum for the Hamiltonian in Eq. 3.3 tuned into the 2D Dirac semi-metal. The figure shows exact diagonalization of this model in a strip geometry (x-direction with open boundaries, and y-direction with periodic boundaries) with $\pm k_{yc} = \pm\pi/3$ and $b_y = \pi/3$. The flat band of states stretched between the Dirac nodes are edge modes.

the analytic result predicts a cusp-like shape that is cut-off in the numerical calculations from finite-size effects. Interestingly we see that even though the system is gapless, the charge polarization calculation gives reasonable, physical results, e.g., it gives a physically meaningful prediction for the boundary charge. This is unusual, but not unprecedented, as [20] has shown that one can have a well-defined polarization in a Chern insulator despite the fact it has gapless boundary modes. We will comment more about this point later.

Already for just two nodes there are some important subtleties to consider when calculating the polarization. The first subtlety has to do with which direction the polarization should point, for example, what determines which boundary has the positive charge in Fig. 3.2, and which end has a negative charge? The answer to this question is well-known: to uniquely specify the polarization we must apply an inversion-breaking (or C-breaking) field that picks the direction of the polarization, and then take the limit as the system size goes to infinity before setting the symmetry-breaking perturbation to zero. This is the conventional paradigm for spontaneous symmetry breaking. Thus, in order to uniquely specify the sign of the polarization, and hence effectively the sign of b_i, we must turn on a small symmetry breaking perturbation before we calculate, and take the limit in which this perturbation vanishes. This issue will arise in Section 3.3 when we try to calculate Eq. 3.7 using field-theoretical methods. To be consistent with the notation in the next section, we will call the inversion symmetry breaking parameter m_A.

The second subtlety is similar in nature, and has to do with determining the value of the polarization in

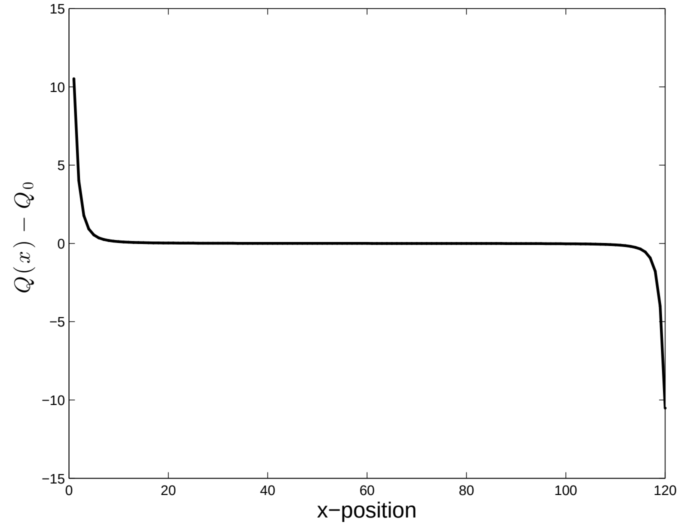

Figure 3.2: We have plotted the deviation of the charge density from the average for $L_x = L_y = 120$ at half-filling in a 2D Dirac semi-metal with $b_y = \pi/3$ (i.e., same parameters as in the previous figure). The average background charge per site is $Q_0 = 120e$. We notice peaks at the boundaries of the system due to the charge carried by localized mid-gap modes. The charge density exponentially decays to the value of $Q_0 = 120e$ within a few lattice sites. The total charge at the boundary calculated from summing the boundary charge near the right edge is $Q_b = -19.6e$ which matches the expected result $Q_b = P_1^x L_y = -\frac{e}{6a}120a = -20e$. The deviation from -20 is a finite-size effect and the result will converge to the analytic value as the system size increases.

a bulk crystalline sample. In fact, in a bulk sample without boundary, since the Brillouin zone is periodic and we have no edge states to reference, we cannot determine a unique value for the polarization of a 2D Dirac semi-metal. For example, in the simplest case of two nodes, how do we determine the magnitude of the polarization if we do not have a preferred way to take the momentum difference between the Dirac nodes? This is a problem because there are multiple ways to subtract the two momenta in a periodic BZ. For our concrete example, our nodes lie at $\vec{k} = (0, \pm\pi/3)$, and so we could let $\vec{b} = \frac{1}{2}(0, 2\pi/3)$ or, e.g., we could subtract the nodes across the Brillouin zone boundary to find $\vec{b'} = \frac{1}{2}(0, 4\pi/3)$. The measurable property of the charge polarization is a boundary charge, which is determined by the occupation of the edge states. For two nodes there are two possible cases for how the edge states traverse the edge BZ. If they go through the origin, we should use $\vec{b} = \frac{1}{2}(0, 2\pi/3)$, or if they instead go through $k = \pi$, then we should use $\vec{b} = \frac{1}{2}(0, 4\pi/3) = (0, \pi) - \frac{1}{2}(0, 2\pi/3)$. These two configurations can be interchanged by first adding a weak topological state, whose edge states will traverse the entire edge BZ, and then coupling it to the DSM which will have the ultimate effect of switching the DSM edge states from one configuration to the other. In Section 3.5 we will see for the general case that, similar to the case of a polarized Chern insulator, the connection between the bulk value of the polarization and the boundary charge can have a more complicated

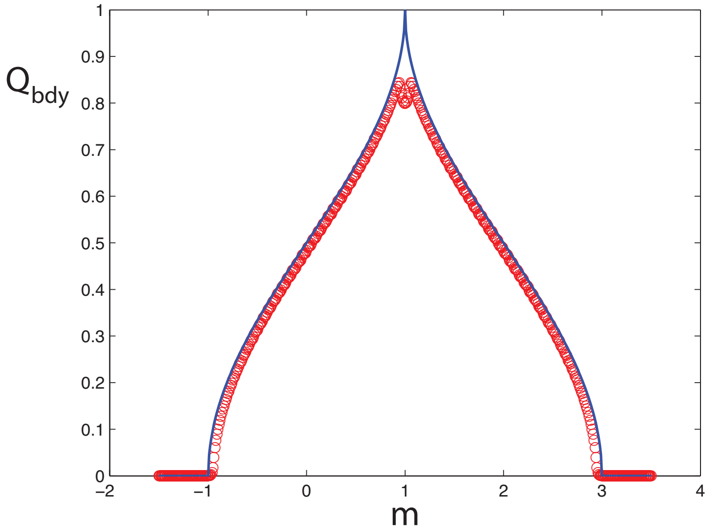

Figure 3.3: The boundary charge is plotted vs. the mass parameter m. The solid blue curve represents $\frac{eb_y}{2\pi}$ where b_y calculated from the solutions to $\cos k_y = -m/t_y$ for a range of m and with $t_y = -1$. The open circles are the numerically calculated boundary charge (per layer) for a system with open boundaries in the x-direction ($L_x = 120$), and periodic boundary conditions in the y-direction. They match except near $m = 1$ where the cusp-like analytic result is cut-off in the numerics due to finite-size effects.

relationship when more than two nodes are present and there are overlapping regions of edge states in the edge Brillouin zone.

3.2.2 Symmetry protection of the response of 2D Dirac semi-metals

Before we move on to discuss the electro-magnetic response due to the time-component b_0, we will address the important issue of symmetry-protection. For the 1D TI, and the 2D WTI constructed from stacks of these 1D TI wires, we have only required inversion symmetry to have a well-defined electromagnetic response. This symmetry quantizes the 1D polarization to be 0 or $e/2$ on each wire, and as shown in [47, 94], this symmetry is also enough to quantize the polarization (per wire) for the 2D WTI. However, it is well-known [4] that for local stability of the Dirac nodes in a DSM, one needs at least the composite $T\mathcal{I}$-symmetry (for $T^2 = +1$). We would like to understand the importance of this seemingly different requirement for the polarization response and the Dirac-node stability. This issue does not arise, for example, in the 3D Weyl semi-metal since the Weyl nodes are locally stable without adding any additional symmetries, and hence, it is important to carefully discuss in the present context.

First, for 1D wires, $T\mathcal{I}$ also quantizes the polarization since P_1 is odd under this symmetry. Thus, we could have already constructed a 1D TI and a 2D WTI using this symmetry instead. In fact, the explicit model we have been considering has $T\mathcal{I}$ symmetry as written, and thus we were able to avoid discussing this issue until now.

Importantly, in dimensions greater than one, $T\mathcal{I}$ symmetry has a crucial effect: it constrains the Berry curvature to satisfy $F(k_x, k_y) = -F(k_x, k_y)$. Since the Berry curvature flux is only defined modulo 2π on a lattice, this requires that for gapped systems either (i) $F(k_x, k_y) = 0$ or (ii) $F(k_x, k_y) = \pi$, and is constant throughout the Brillouin zone (we will only consider the former case[2]). Hence, with this symmetry we expect a vanishing Berry curvature. However, if $F(k_x, k_y)$ is not required to be smooth, we can have singular points in momentum space where $F(k_{xc}, k_{yc}) = \pi$; these are exactly the set of Dirac node locations. Since the Berry flux that passes through a closed manifold, e.g., the BZ, must be a multiple of 2π, this implies that there are an even number of singular points, i.e., fermion doubling. This conclusion immediately implies local stability of the Dirac nodes, because if $T\mathcal{I}$ is preserved and one of the Dirac nodes disappears locally by itself, then there will not be an integer amount of Berry flux in the BZ which is a contradiction.

This constraint, and thus the $T\mathcal{I}$ symmetry itself, is also essential for the 2D charge polarization response of the DSM. Let us illustrate the idea. Suppose we wish to calculate the charge polarization of a crystalline DSM. The physical consequence of a non-vanishing polarization is a boundary charge, so let us specify a particular boundary with a normal vector $\mathbf{G}_N$ in the reciprocal lattice. Let $\mathbf{G}_F$ be the dual vector to $\mathbf{G}_N$, i.e., $G_F^i = \epsilon^{ij} G_N^j$. Then $\mathbf{G}_F$ is the normal vector to a set of lattice lines whose ends terminate on the surface normal to $\mathbf{G}_N$. For example, pick $\mathbf{G}_N = 2\pi\hat{x}$ and $\mathbf{G}_F = 2\pi\hat{y}$. In this case our choice picks out a family of 1D wires parallel to the x-direction and stacked in the y-direction. Consequently, this gives rise to a family of 1D Bloch Hamiltonians parameterized by the momentum along $\mathbf{G}_F$. In this example we have the family $H_{k_y}(k_x)$ which is parameterized by k_y.

To calculate the charge polarization of the DSM with our choice of $\mathbf{G}_N$ (i.e., the polarization parallel to $\mathbf{G}_N$), we can start by asking an important question: how much does the charge polarization of the family of 1D systems $H_{k_y}(k_x)$ vary as k_y is varied? We find

$$\begin{aligned}
& P_1^x(k_{y2}) - P_1^x(k_{y1}) \\
= \;& \frac{e}{2\pi}\int_{-\pi}^{\pi} dk_x a_x(k_x, k_{y2}) - \frac{e}{2\pi}\int_{-\pi}^{\pi} dk_x a_x(k_x, k_{y1}) \\
= \;& \frac{e}{2\pi}\int_{-\pi}^{\pi} dk_x \int_{k_{y1}}^{k_{y2}} dk_y \mathcal{F}(k_x, k_y) \\
= \;& \frac{e}{2}\sum_{a=1}^{N_{enc}} \chi_a
\end{aligned} \tag{3.9}$$

---

[2] The authors do not know of any models which realize the latter case. One must also worry about the fact that the total flux must be a multiple of 2π and thus, to be well-defined we must have an even number of discretized momentum points. This constraint seems a bit artificial so we will not consider this case further.

where we have used Stokes theorem to replace the line integrals over the Berry connection $\mathbf{a}(\mathbf{k})$ by an area integral over $\mathcal{F}(k_x, k_y) = \partial_{k_x} a_y - \partial_{k_y} a_x$, i.e., the Berry curvature, and we have assumed only one occupied band for simplicity. In the last equality we used the fact that for systems with $T\mathcal{I}$-symmetry the Berry curvature only contains contributions from the singular Dirac points, and the sum runs over all enclosed Dirac nodes. The quantity $\chi_a = \pm 1$, which we will call the *helicity* of a Dirac node, indicates whether the flux carried by the node is $\pm\pi$. Thus, two 1D Hamiltonians that are members of the parameterized Hamiltonian family specify cycles in the Brillouin zone, and from this result we see that the polarization can only change if the area of the Brillouin zone enclosed between those two 1D cycles contains Dirac nodes. This restriction is the key feature of a $T\mathcal{I}$-symmetric system that determines the polarization response. As an aside we note that, since the BZ is a closed manifold, there are two possible ways to choose the region "enclosed" by the closed cycles and this is related to one source of ambiguity in the value of the polarization discussed earlier.

This result in Eq. 3.9 is generically true given a general family of Bloch Hamiltonians (with $T\mathcal{I}$-symmetry) with some orientation specified by $\mathbf{G}_N$, and parameterized by momentum along $\mathbf{G}_F$. In fact, given two 1D cycles that are members of a parameterized Hamiltonian family in the Brillouin zone, then any deformation/rotation of the orientation of the lines, i.e., variation of the choice of the direction vector $\mathbf{G}_N$ will not change the difference in polarization between the two parallel lines unless the lines cross Dirac points during the deformation process. This implies that the *changes* in polarization are always quantized in the presence of $T\mathcal{I}$-symmetry, which is crucial for being able to determine the polarization from the nodal data.

Since the changes in polarization between different cycles are quantized, we might now ask about the properties of the total polarization. Since each 1D subspace is mapped onto itself by $T\mathcal{I}$, and the polarization of that 1D system is odd under $T\mathcal{I}$, we see that the polarization of each of the wires/cycles is quantized to be 0 or $e/2$. The other wires in the family of Hamiltonians either have exactly the same polarization, or they differ by a quantized amount. For the case with only two nodes, this argument shows that the (fractional part of the) boundary charge, up to an integer per unit cell, is completely determined by the length of b_i that projects onto the edge BZ, which confirms what is predicted in Eq. 3.7 (more subtleties will arise when we have to consider cases with nodes arising from multiple bands that give rise to overlapping boundary states). The sign of the polarization for two nodes, however, is still ambiguous and can only be determined after a symmetry-breaking parameter is added, and after knowing whether we should project the difference between the nodes through the edge BZ origin or the edge BZ boundary. As we will discuss more carefully below, for two nodes the overall sign and value of the polarization can also be modified by the addition of non-trivial, occupied weak TI bands to the system. As far as the boundary theory is concerned, this

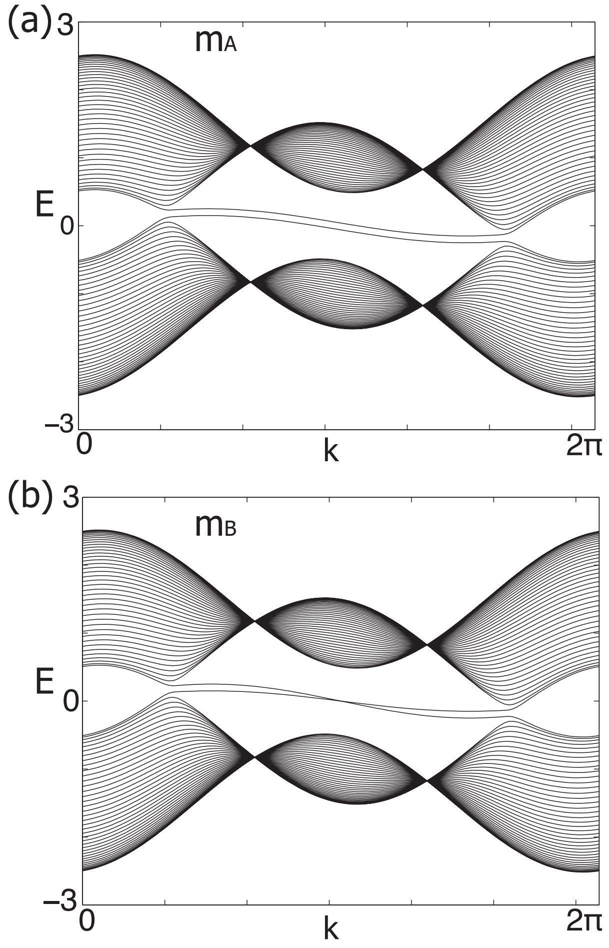

Figure 3.4: The Energy spectrum is shown for the DSM with $b_0 \neq 0$ and different masses turned on. (a) With $m_A \neq 0$, we see that the edge modes split and don't cross as they move between the Dirac nodes. (b) With $m_B \neq 0$, it looks like the edge mode dispersion of a Chern insulator and they cross at $k = 0$.

is equivalent to adding an additional flat band of edge states which traverse the entire Brillouin zone, and because of the $\mathbb{Z}_2$ nature of the polarization this has to be carefully handled.

3.2.3 Magnetization response of a 2D Dirac semi-metal

After finishing our discussion of the symmetry protection, and the importance of $T\mathcal{I}$ symmetry for the charge polarization, let us now move on to a discussion of the response due to a non-vanishing b_0. We have seen that the spatial part of b_μ can be interpreted as a charge polarization, and, as will be shown below, the component b_0 represents an orbital magnetization. Before we provide the explicit proof, let us assume that this is the case and support the conjecture with some physical arguments and numerical calculations.

The physical manifestation of a non-vanishing magnetization is a circulating current bound at the edges of the sample. From our conjecture, we should be able to induce such a magnetization by turning on a b_0.

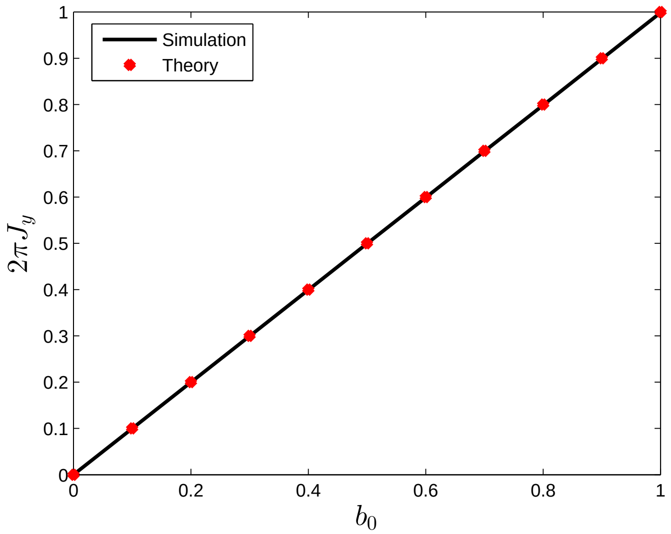

Figure 3.5: The bound current J_y localized near a single edge vs. b_0 is plotted for the model in Eq. 3.3 with $b_y = \frac{\pi}{3}, m_A = 10^{-3}, L_{x,y} = 120$, and periodic boundary conditions in the y-direction. The current matches the field theory prediction.

We can generate a b_0 by adding the term $\gamma \sin k_y \mathbb{I}$ to the Dirac semi-metal lattice Hamiltonian in Eq. 3.3. The value of b_0 generated would be $b_0 = (\gamma/\hbar) \sin k_{yc}$, where $k_y = k_{yc}$ is the location of the Dirac node (and consequently $-k_{yc}$ is the location of the other node). On topological edges we can immediately see that the addition of this term will cause the flat edge modes to disperse (see Appendix A.3 for a proof). This is also seen the numerical calculations in Fig. 3.4a. Thus, the dispersion of the edge modes attached to the Dirac points is exactly what generates the bound current; at least on the edges which actually harbor topological bound states.

Let us try to confirm this result numerically by calculating the current in the lattice model. Just as for the polarization, to properly calculate the response numerically, there is a subtlety about how to fill the edge states. To do this properly we again need to choose a small, non-zero inversion-breaking mass before filling the edge modes. In the language of [20], to properly fill the edge modes in the presence of a non-vanishing m_A we need to use the *adiabatic* filling, not the thermal filling, if we want to calculate the magnetization. One can see the energy spectrum for $b_0 \neq 0$ in Fig. 3.4a with a finite m_A parameter. Adiabatic filling implies filling all of the states, including the edge modes, in the lower half of the spectrum below the energy gap induced by m_A. In Fig. 3.5 we plot the boundary current localized near a single edge vs. b_0. The bound edge current is exactly $\frac{eb_0}{2\pi}$, which corroborates our conjecture that the magnetization is proportional to b_0.

It is interesting to note that in the model in Eq. 3.3 the x and y directions are very different since we have topological wires oriented along x that are stacked in y. This should be contrasted with the fact that an orbital magnetization in 2D implies the existence of a bound current on *any* edge (i.e., any interfaces where the magnetization jumps from a finite value to zero). For the topological edges, with normal vectors parallel to the x-direction, a non-zero b_0 gives the edge modes a non-zero dispersion as shown in Fig. 3.4a. The dispersing edge states produce an exponentially localized current j^y_{bound} that corresponds to the change in magnetization at the edge. However, in the y-direction there are no topological edge modes, and it is interesting to consider what happens to j^x on these edges.

We show the result of a numerical calculation in Figs. 3.6 and 3.7. In the former, we compare the current profiles of the different edge types in two different cylinder geometries corresponding to the two different edge types. In Fig. 3.6a we show the current on a non-topological edge (J_x on an edge normal to $\hat{y}$), which is still localized on the boundary, but has an oscillatory decay. The wavelength of the oscillation in fact matches the wavelength of the Dirac node wave-vectors in momentum space. In Fig. 3.6b we show the current localized on topological edges (J_y on an edge normal to $\hat{x}$) and we can see that each edge carries exponentially localized current with opposite currents on opposite edges.

In Fig. 3.7 we show the current density on a fully open sample, where we see that all of the current is localized near the edges. The colors are associated to the magnitude of the current parallel to a given edge. Essentially this is just a different presentation of the data in Figs. 3.6a,b that shows that on both sets of edges there is a bound current, as expected from the orbital magnetization. Interestingly, on the edges without topological bound states the current oscillates as it decays. However, the magnitude of the current localized near edges of either type is identical, so indeed, even though the model is highly anisotropic, the bulk orbital magnetization generates bound currents on all edges, not just topological ones.

Further, we note that in the case with just two nodes the magnetization has no dependence on whether the edge states go through the origin of the edge BZ or through the boundary of the edge BZ (i.e., at $k_y = \pi$) assuming that the sign of the inversion breaking parameter and the helicities of the nodes remain the same, and only the edge state locations are flipped. This is explicitly demonstrated in Fig. 3.6 where the total currents passing through each edge match exactly for these two cases. To generate the second case, where the edge states pass through π in the edge BZ we can choose our square lattice model with the same parameters as before except letting $A = -1, t_y = -1$. Below we will introduce quantities Θ_i where $i = x, y$ that track whether the edge states pass through the origin of the edge BZ ($\Theta_i = +1$) or the boundary of the edge BZ ($\Theta_i = -1$) for different directions (e.g., $i = x$ or y). As we will see, these signs will enter the expressions for the charge polarizations, but not the magnetization. When there are more than just two nodes the magnetization is affected by the different edge state configuration possibilities, but not the same way as the polarization.

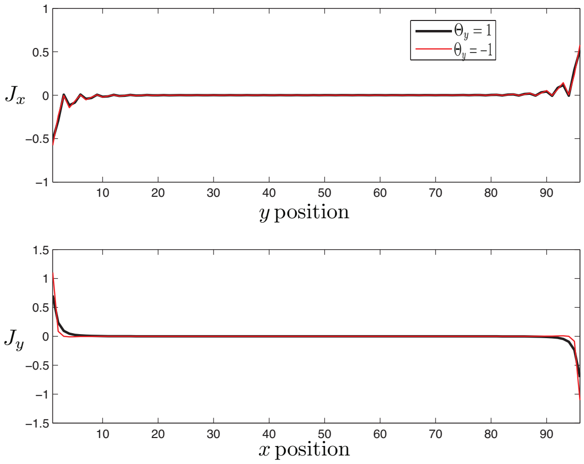

Figure 3.6: Plots of (a) J_x vs. y which is the current on the non-topological edge and (b) J_y vs x which is the current on the topological edge. This is for the Dirac semi-metal considered in previous figures but with a non-zero b_0. For this system $b_y = \frac{\pi}{3}, \gamma = 0.1, m_A = 0.1$, and $L_{x,y} = 96$. There are open boundary conditions in both directions. We note that j_y is exponentially localized whereas j_x is less-sharply localized and oscillates as it decays into the bulk. The oscillation wavelength coincides with the wave-vector location of the Dirac nodes in k-space. With open boundary conditions, we must be careful to properly fill the edge states by using a non-zero inversion breaking mass term m_A. The currents with $\Theta_y = \pm 1$ are plotted in black and red. The total current near the boundaries is identical in both cases and thus the magnetization does not depend on how the edge states traverse on the edge BZ. The slight difference between the current profiles in (b) is due to the fact that the wavefunctions of the occupied edge modes that determine those boundary currents are different in the two cases with $\Theta_y = \pm 1$, however the total current is the same.

Now that we have motivated the electromagnetic response of the DSM using some analytic and numeric results on an example model, we will now prove these claims using a Dirac semi-metal model with two nodes, and then go on to generalize to a generic even number of nodes.

3.3 Derivation of response for continuum Dirac semi-metal in 2D

In the previous section we posited a form for the EM response action of the DSM, and gave some concrete examples in which the numerical simulations in lattice models matched the response derived from the effective action in Eq. 3.7. In this section we will derive the EM response from a continuum model of the DSM using standard linear response techniques. We derived an example of a continuum Hamiltonian for the DSM in Eq. 3.6, and we will use this as our starting point. After tuning the velocity coefficients to be isotropic, we can write the Hamiltonian for two Dirac cones that exist at the same point in the Brillouin zone as

$$H = k_x \mathbb{I} \otimes \sigma^x + k_y \tau^z \otimes \sigma^z \tag{3.10}$$

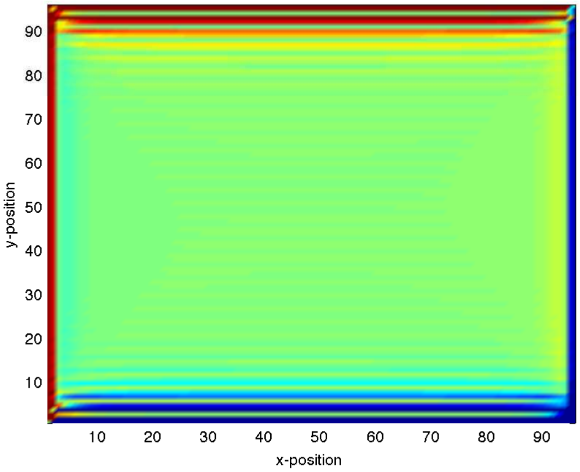

Figure 3.7: With a similar set up to the previous figure, we use a density plot for the current vs x, y position for the 2D Dirac semi-metal with $b_y = \frac{\pi}{3}, \gamma = m_A = 0.1, L_{x,y} = 96$, and we have open boundary conditions in both directions. We calculated the current-density in the x-direction and summed it with the current density in the y-direction to produce this pseudo-color plot. We see that the currents are spatially localized at the edges, strongly for the one moving along the edges parallel to the y-axis and less-strongly and oscillatory for the one moving along the edges parallel to the x-direction. The total magnitude of the current in the neighborhood of each edge is the same, and the current circulates around the boundaries of the sample.

where τ^a are Pauli-matrices representing the two nodes. To this Hamiltonian we will add two perturbations, the first of which is a splitting vector $b_\mu = (b_0, b_x, b_y)$ that shifts the two cones apart in momentum (by $2\vec{b}$) and energy (by $2b_0$). With the inclusion of this vector, which, if needed, we will allow to be slowly varying in space-time, the Hamiltonian becomes

$$H = k_x \mathbb{I} \otimes \sigma^x - b_x \tau^z \otimes \sigma^x + k_y \tau^z \otimes \sigma^z - b_y \mathbb{I} \otimes \sigma^z + b_0 \tau^z \otimes \mathbb{I}. \tag{3.11}$$

The second type of perturbation we will allow for is the coupling to external EM fields, which enter the Hamiltonian via minimal coupling $\mathbf{k} \to \mathbf{k} - (e/\hbar)\mathbf{A}$.

To calculate the linear response we need the current operators that will enter the Kubo-formula calculation. For the EM field the current operators are

$$J_A^x = \frac{\delta H}{\delta A_x} = \frac{e}{\hbar} \mathbb{I} \otimes \sigma^x \equiv \frac{e}{\hbar} \Gamma^x \tag{3.12}$$

$$J_A^y = \frac{\delta H}{\delta A_y} = \frac{e}{\hbar} \tau^z \otimes \sigma^z \equiv \frac{e}{\hbar} \Gamma^y \tag{3.13}$$

$$J_A^0 = \frac{\delta H}{\delta A_0} = \frac{e}{\hbar} \mathbb{I} \otimes \mathbb{I}. \tag{3.14}$$

For the splitting vector b_μ, the associated currents are

$$
\begin{aligned}
J_B^x &= \frac{\delta H}{\delta b_x} = -\tau^z \otimes \sigma^x \equiv \Lambda^x && (3.15)\\
J_B^y &= \frac{\delta H}{\delta b_y} = -\mathbb{I} \otimes \sigma^z \equiv \Lambda^y && (3.16)\\
J_B^0 &= \frac{\delta H}{\delta b_0} = \tau^z \otimes \mathbb{I} \equiv \Lambda^0. && (3.17)
\end{aligned}
$$

We want to calculate the "topological" response terms for the DSM and, in 2+1-d, we will see that such response terms will break either time-reversal or inversion symmetry. It is well known that Dirac fermions in 2+1-d exhibit a parity anomaly that gives rise to a Chern-Simons contribution to the effective action that encodes a non-vanishing Hall conductivity [80, 37]. There is a subtlety: to calculate the non-vanishing coefficient one must introduce a finite, (time-reversal) symmetry-breaking mass parameter that is taken to vanish at the end of the calculation. Since the resulting response coefficient ends up being proportional only to the sign of the symmetry breaking parameter, it remains non-zero even in the limit where the symmetry breaking is removed. This effect is a manifestation of a quantum breaking of symmetry, i.e., an anomaly. One of the main results of this section is that we will show the same is true for an inversion-breaking mass term, not just the time-reversal breaking mass term.

To calculate the responses due to A_μ or b_ν perturbations, we will need to introduce two different types of symmetry-breaking mass terms

$$
\begin{aligned}
\Sigma_A &= \mathbb{I} \otimes \sigma^y && (3.18)\\
\Sigma_B &= \tau^z \otimes \sigma^y. && (3.19)
\end{aligned}
$$

These two different mass matrices commute, and thus they are *competing* mass terms. They both separately anti-commute with the kinetic part of the Dirac Hamiltonian (including the constant momentum shift $\vec{b}$), and thus the spectrum will be gapped as long as the coefficients (m_A, m_B) of (Σ_A, Σ_B) are not equal in magnitude. Explicitly, if both mass terms are activated, the energy spectrum is $\pm E_\pm = \pm\sqrt{(k_x - b_x)^2 + (k_y - b_y)^2 + (m_A \pm m_B)^2}$ which is gapped unless $|m_A| = |m_B|$. These mass terms are very familiar in the literature: Σ_A is essentially the inversion-breaking Semenoff mass term [83], and Σ_B is the continuum version of the time-reversal breaking Haldane mass term [37].

Generically, in linear response, we will find contributions to the effective action of the form

$$
S_{eff}[A_\mu, b_\nu] = \int \frac{d^3 p_1}{(2\pi)^3} \mathcal{A}_\mu^a(p_1) \Pi_{ab}^{\mu\nu}(p_1) \mathcal{A}_\nu^b(-p_1), \tag{3.20}
$$

which has been written in the Fourier-transformed basis, and where $a, b = A, B$, $\mathcal{A}^A_\mu = A_\mu$ and $\mathcal{A}^B_\mu = b_\mu$. The linear response calculation (or equivalently the calculation of the quadratic term in the effective action) amounts to the calculation of the long-wavelength, DC limit of the generalized polarization tensor

$$\Pi^{\mu\nu}_{ab}(\nu, \mathbf{q}) = \frac{\hbar}{2}\int \frac{d\omega d^2p}{(2\pi)^3}\mathrm{tr}\left[J^\mu_a G(\omega+\nu, \mathbf{p}+\mathbf{q}) J^\nu_b G(\omega, \mathbf{p})\right] \tag{3.21}$$

where $\mu, \nu = 0, x, y$; $a, b = A, B$, and $G(\omega, \mathbf{p})$ is the space and time Fourier transform of the single-particle Green function of the unperturbed ($b_\mu = 0, A_\mu = 0$) Dirac model.

The calculation of $\Pi^{\mu\nu}_{ab}$ is sensitive to the choice of symmetry breaking masses m_a. Since we are only interested in extracting the topological terms in the semi-metallic limit, we can consider two cases (i) $|m_A| > |m_B| = 0$ and (ii) $|m_B| > |m_A| = 0$. We will briefly consider the case when both mass terms are non-zero in Section 3.6.

The Fourier transform of the unperturbed Green function in either of these limits will be

$$\begin{aligned} G(\omega, p) &= \frac{1}{\omega - p_x\Gamma^x - p_y\Gamma^y - m_c\Sigma^c} \\ &= \frac{\omega + p_x\Gamma^x + p_y\Gamma^y + m_c\Sigma^c}{\omega^2 - |\mathbf{p}|^2 - m_c^2} \end{aligned} \tag{3.22}$$

where the label $c = A$ or B, and is not summed over. The topological terms in the polarization tensor can be calculated by extracting the terms proportional to odd powers of the symmetry breaking mass:

$$\begin{aligned} \Pi^{\mu\nu}_{ab}(\nu, \mathbf{q}) &= \frac{\hbar}{2}\int \frac{d\omega d^2p}{(2\pi)^3} f(\omega+\nu, \mathbf{p}+\mathbf{q}) f(\omega, \mathbf{p}) \\ &\times \ \mathrm{tr}\left[J^\mu_a m_c\Sigma_c J^\nu_b(\omega + p_x\Gamma^x + p_y\Gamma^y)\right. \\ &+ \ J^\mu_a(\omega + \nu + (p_x+q_x)\Gamma^x \\ &+ \ \left.(p_y+q_y)\Gamma^y) J^\nu_b m_c\Sigma^c\right] \qquad (3.23) \\ f(\omega, \mathbf{p}) &= \frac{1}{\omega^2 - |\mathbf{p}|^2 - m_c^2}. \qquad (3.24) \end{aligned}$$

Now, to be explicit, let us consider case (i) where m_A is the non-vanishing mass term. We can extract the leading term in the external frequency/momentum which we find to be

$$\begin{aligned} \Pi^{\mu\nu}_{ab}(\nu, \mathbf{q}) &= 4\frac{e}{2}m_A\epsilon^{\mu\rho\nu}(iq_\rho)\sigma_{ab}\int \frac{d\omega d^2p}{(2\pi)^3}\left[f(\omega, \mathbf{p})\right]^2 \\ &= \frac{4\pi^2}{(2\pi)^3}\frac{e}{2}\frac{m_A}{|m_A|}\epsilon^{\mu\rho\nu}(iq_\rho)\sigma_{ab} \\ &= \frac{e}{4\pi}(\mathrm{sgn}\ m_A)\epsilon^{\mu\rho\nu}(iq_\rho)\sigma_{ab} \end{aligned} \tag{3.25}$$

where $q_\rho = (\nu, \mathbf{q})$ is the external 3-momentum, $\sigma_{AB} = \sigma_{BA} = 1$, and $\sigma_{AA} = \sigma_{BB} = 0$. This leads to a term in the effective action

$$S^{(A)}_{eff}[A_\mu, b_\nu] = \frac{e}{2\pi}(\text{sgn}\, m_A) \int dt d^2 x \epsilon^{\mu\nu\rho} A_\mu \partial_\nu b_\rho. \tag{3.26}$$

This result exactly matches Eq. 3.7 except for the factor of sgn m_A which we already motivated as being necessary to pick the sign of the charge polarization.

From this continuum calculation for two nodes we can extract the polarization and magnetization in a nice way as

$$(M, \epsilon^{ij}\Theta_i P_i) = \frac{e}{4\pi}(\text{sgn}\, m_A) \sum_{a=1}^{2} \chi_a K_{a,\mu} \tag{3.27}$$

where $K_{a,\mu}$ are the momentum and energy locations of the nodes, and the χ_a are the helicities of the nodes. Even for just two nodes the polarization calculated in the continuum approximation is ambiguous since the edge states connecting the nodes could pass through the origin or boundary of the edge BZ. We have corrected for this in Eq. 3.27 by adding the extra signs $\Theta_i = \pm 1$, $(i = x, y)$ which indicate exactly if the edge states run through the origin on the edge BZ ($\Theta_i = +1$) or through π ($\Theta_i = -1$) as motivated before. In general, when not on the square lattice, there is one value of Θ for each independent spatial direction. These extra signs only enter the formula for the polarization, not the magnetization as mentioned above.

A precise definition of Θ_i can be determined purely from the bulk properties of the system by calculating the Wilson line of the Berry connection along the 1D Bloch Hamiltonian subspace that projects onto $k = \pi$ in the respective edge BZs (it is analogous to calculating the weak invariant ν_i). This Wilson line can only take two values because of the $T\mathcal{I}$ symmetry, and its trivial (non-trivial) value corresponds to $\Theta_i = +1(-1)$. It is important to note that a knowledge of Θ_i is not contained in the manifold of band touchings alone, and requires some knowledge of the occupied bands. For the two node case, this implies that the (fractional part of the) polarization can only be determined up to an overall sign if we only have knowledge of the continuum band touching points and their locations in the BZ. However, the magnetization does not share this particular ambiguity due to Θ_i. This might be attributed to its more isotropic nature.

In this continuum picture we could also imagine having more flavors of fermions with different nodal locations, but with Hamiltonians of essentially the same form as in Eq. 3.10. Since we want to eventually consider lattice models with multiple pairs of nodes we know there must be an even number of total nodes, say $2N$, and an equal number N of them have opposite helicity. From our calculation, the polarization/magnetization for such a system might be trivially generalized as

$$(M, \epsilon^{ij}\Theta_i P_i) = \frac{e}{4\pi} \sum_{a=1}^{2N} g_a \chi_a K_{a,\mu} \tag{3.28}$$

where g_a represents the sign of the symmetry-breaking mass for each Dirac point. Unfortunately, this simple generalization has a few caveats, one example being that it does not take care of the $\mathbb{Z}_2$ nature of the edge states, which becomes important when edge states from different blocks overlap in the edge BZ. We will discuss the details of this generalization in Section 3.5.

If we repeat this calculation for case (ii), where m_B is non-vanishing, the result is almost identical, except for the replacement of the matrix σ_{ab} by the Kronecker δ_{ab}, i.e., the polarization tensor is

$$\Pi^{\mu\nu}_{ab}(\nu, \mathbf{q}) = \frac{\hbar e_a^2}{4\pi}(\text{sgn } m_B)\epsilon^{\mu\rho\nu}(iq_\rho)\delta_{ab} \tag{3.29}$$

where the charge $e_A = e/\hbar$ and $e_B = 1$. Now this gives rise to two terms in the effective action

$$\begin{aligned} S^{(B)}_{eff}[A_\mu, b_\nu] &= \frac{e^2}{2h}(\text{sgn } m_B)\int dtd^2x\epsilon^{\mu\nu\rho}A_\mu\partial_\nu A_\rho \\ &+ \frac{\hbar}{4\pi}(\text{sgn } m_B)\int dtd^2x\epsilon^{\mu\nu\rho}b_\mu\partial_\nu b_\rho. \end{aligned} \tag{3.30}$$

The first term is the conventional Chern-Simons term which yields a Hall conductivity of $\sigma_{xy} = \frac{e^2}{h}(\text{sgn } m_B)$ which consists of $\frac{e^2}{2h}(\text{sgn } m_B)$ from each of the two Dirac cones. This type of response has been discussed extensively in the literature so we will not dwell on it here. The second term, which does not yield an electromagnetic response since it is independent of A_μ, will be discussed later in Appendix A.7.

3.4 Physical interpretation of the Dirac semi-metal response

The topological EM response of the DSM is more complicated than the 1D band metal because the response density and current depend on derivatives of b_μ, not just the vector itself. When the time-reversal mass term m_B dominates, and there are only two nodes, then we just generate the well-known Chern insulator phase [37], or its associated parity anomaly in the limit $m_B \to 0$ [80]. In this section we will consider the less well-known case of when m_A dominates, and the resulting inversion-breaking semi-metal limit. This will help us solidify an appropriate definition of charge polarization and magnetization for 2D Dirac semi-metals, akin to the definition provided for Chern insulators in [20]. In Section 3.6 we will revisit the case when m_B is non-vanishing, and consider the effects of a finite m_A term in the Chern insulator phase.

3.4.1 Response In the Inversion-Breaking Limit (m_A Dominating Regime)

Let us consider the limit in which the inversion breaking mass m_A dominates over the time-reversal mass m_B, and then send them both to zero (with $m_B \to 0$ first). In that limit the response that we derived is given by

$$S_{eff}^{(A)}[A_\mu, b_\mu] = \frac{e}{2\pi}(\text{sgn } m_A) \int dt d^2x \epsilon^{\mu\nu\rho} A_\mu \partial_\nu b_\rho. \tag{3.31}$$

The current from this effective action is given by

$$\begin{aligned} j^\alpha &= \frac{e}{2\pi}(\text{sgn } m_A)\epsilon^{\alpha\mu\nu}\partial_\mu b_\nu \\ \implies \rho &= \frac{e}{2\pi}(\text{sgn } m_A)(\partial_x b_y - \partial_y b_x) \\ j^i &= \frac{e}{2\pi}(\text{sgn } m_A)\epsilon^{ij}(-\partial_0 b_j + \partial_j b_0). \end{aligned} \tag{3.32}$$

To simplify let us assume that $m_A \to 0^+$ so that we can replace $\text{sgn}\, m_A = +1$.

These equations can be more easily interpreted if we replace b_i via the polarization $P_1^i = -\frac{e}{2\pi}\epsilon^{ij}b_j$ to generate

$$\begin{aligned} \rho &= -\partial_i P_1^i \\ j^i &= \partial_0 P_1^i + \frac{e}{2\pi}\epsilon^{ij}\partial_j b_0. \end{aligned}$$

We immediately recognize these equations as the contributions to the charge density and current from gradients and time-derivatives of the polarization. It is also easy to interpret the term involving b_0, as it just represents the contribution to the current from gradients in the magnetization. We can let $M = \frac{e}{2\pi}b_0$ be the out-of-plane magnetization, from which we finally arrive at

$$\begin{aligned} \rho &= -\partial_i P_1^i \\ j^i &= \partial_0 P_1^i + \epsilon^{ij}\partial_j M \end{aligned} \tag{3.33}$$

which are the familiar constituent relations for bound charge density and bound charge current in 2D. Thus we see that, in the limit where m_A dominates over m_B and then tends to zero, the DSM will exhibit an effective polarization and magnetization if b_i and b_0 are non-zero respectively. Bound charge and current manifest at interfaces or boundaries where the bulk values of b_μ are changing, and are the consequence of the topological response.

The relation between b_μ and the bulk magnetization and polarization makes an important physical connection between generic electromagnetic quantities (P_1^i, M), and the quantities $(\epsilon^{ij}b_j, b_0)$ that are determined by the energy and momentum locations of the nodal Dirac points in the electronic spectrum. Accordingly, we can rewrite the effective action as

$$S_{eff}^{(A)}[A_\mu, b_\mu] = \int dt d^2x \left[M(b_\mu)B + P_1^i(b_\mu)E_i\right] \tag{3.34}$$

where we have included the dependence on b_μ. Writing the action this way is interesting because it highlights that the DSM can have a well-defined polarization; something that is usually reserved for gapped insulators. From this we see that one possible signature of a clean DSM with non-degenerate nodes would be a semi-metal phase with $\mathcal{TI}$-symmetry and a non-vanishing charge polarization/magnetization.

3.4.2 Polarization and boundary charge

Using the model for the DSM introduced above, let us revisit the origin of the bound charge and bound current from a more microscopic picture. From the effective action we see that we need b_y to change with x or vice-versa to generate a non-zero charge density. To produce a non-zero current, we need b_0 to vary with x or y. The easiest way to do either of these is to have an interface or boundary. First, suppose we have a boundary where b_y changes with x as $b_y = b_y\Theta(x - x_0)$, where $\Theta(x)$ is a step-function. From the response action we should have a bound charge density

$$\rho = (\text{sgn } m_A)\Theta_y \frac{eb_y}{2\pi}\delta(x - x_0). \tag{3.35}$$

where we recall that the Θ_y in this formula is needed to capture the correct sign of the boundary charge for lattice systems (c.f. Eq. 3.27).

The magnitude of the charge density determined by the bulk response action exactly matches the boundary charge we find in the DSM model from the edge modes stretched between the two nodes. The role of the value of (sgn m_A)Θ_y is to fix which edge has the occupied states, and subsequently, which edge is unoccupied. Due to the inversion breaking mass, each boundary state on one edge will be occupied and contribute $e/2$ charge on that boundary for each edge mode. On the other edge, all of the boundary modes will be unoccupied, and each contributes a deficit charge of $-e/2$. The total number of occupied of states on the edge is given by the distance spanned by the edge states between the two nodes multiplied by $\frac{L_{edge}}{2\pi}$, which, in total, is $L_{edge}\frac{2b_y}{2\pi}$. So, the total charge at the positive edge is given by $L_{edge}\frac{e}{2} \times \frac{b_y}{\pi} = L_{edge}\frac{eb_y}{2\pi}$. This implies a polarization of $\frac{eb_y}{2\pi}$ as expected. Thus, we see that while the charge response in the 1D semi-metal is controlled by the bulk states, here it manifests as a property of the boundary modes. This is due to the charge density depending on derivatives of b_i instead of b_i itself.

3.4.3 Orbital magnetization and boundary current

Next, let us consider the microscopic origin of the magnetization. The bound current that exists on interfaces when b_0 is non-vanishing, i.e., when there is a bulk magnetization, is more delicate. For example, the magnetization, as far as the 2D system is concerned, is isotropic and thus should give rise to bound currents on *any* interface, not just an edge with low-energy modes. We already showed in Figs. 3.6 and 3.7 that, even though the DSM model we have chosen is inherently anisotropic, there are bound currents on all of the edges. Let us now prove that this boundary current is indeed connected to the bulk orbital magnetization.

First, to generate a non-vanishing b_0 in the DSM model, we can add a kinetic energy term $\epsilon(k) = \gamma \sin k_y \mathbb{I}$ to the Hamiltonian $H_{2DWTI}(k)$ in Eq. 3.3. If the Dirac nodes are separated in the k_y direction and located at $\vec{k} = (0, \pm k_{yc})$, as for our earlier parameter choice, then this simple kinetic term will generate an energy difference of $2\gamma \sin k_{yc} \equiv 2\hbar b_0$ between the Dirac nodes. Note that this term breaks both T and $\mathcal{I}$ but preserves the composite symmetry $T\mathcal{I}$ which is required for the local stability of the Dirac nodes. Since it breaks T, in principle, a magnetization would be allowed by symmetry.

Next, we can calculate the magnetization for this model according to the results of [13, 105] using

$$M = \frac{e}{2\hbar} \int \frac{d^2k}{(2\pi)^2} \mathrm{Im}\left[\langle \partial_x u_- | (H(k) + E_-(k)) | \partial_y u_- \rangle - \langle \partial_y u_- | (H(k) + E_-(k)) | \partial_x u_- \rangle\right] \tag{3.36}$$

where $E_-(k), |u_-\rangle$ are the energy and Bloch functions of the lower occupied band, $H(k) = \epsilon(k) + H_{2DWTI}(k)$, and the derivatives are with respect to momentum. To properly calculate this quantity, we need to turn on a small, but finite, m_A and then set it to zero at the end of the calculation. From symmetry, and from the fact that the extra kinetic term is proportional to the identity matrix, the only terms that contribute to the non-vanishing magnetization are those proportional to $\epsilon(k)$, and we find the simplification [105]

$$M = \frac{e}{2\hbar} \int \frac{d^2k}{(2\pi)^2} 2\epsilon(k) F_{xy}(k) \tag{3.37}$$

where $F_{xy}(k)$ is the Berry curvature.

For small m_A we know that F_{xy} is sharply peaked at each of the two Dirac nodes. For example, when $m_A = 0$ then $T\mathcal{I}$ is preserved, and the Berry curvature is a δ-function source at each node. When $m_A \neq 0$ the contributions of the two Dirac points to the Berry curvature have *opposite* signs because of their opposite helicities. Thus, we can see that if $\epsilon(k)$ had the same value for both Dirac nodes then M would vanish. In the semi-metallic limit $m_A \to 0$, which is the limit of physical interest, the magnetization becomes

$$M = (\operatorname{sgn} m_A) \frac{e\Phi_{Dirac}}{4\pi^2\hbar} \sum_{a=1}^{N_{Dirac}} \epsilon(\vec{K}_a)\chi_a \tag{3.38}$$

where $\vec{K}_a$ is the location of the a-th Dirac point, $\epsilon(\vec{K}_a)$ is the energy of the a-th Dirac point, χ_a is the sign of the Berry phase around the Fermi-surface of each Dirac point for an infinitesimally positive chemical potential, and Φ_{Dirac} is the constant Berry curvature flux carried by each Dirac point in the gapless limit, i.e., $\Phi_{Dirac} = \pi$. In terms of b_0 for our single pair of Dirac points, we find $M = (\operatorname{sgn} m_A)\frac{e}{2\pi}b_0$ as expected. While this is the general result for the bulk magnetization, even for a lattice model, the connection to a boundary current must be carefully addressed if there are Dirac nodes with overlapping edge modes that can cancel in a $\mathbb{Z}_2$ fashion. We will discuss this more in Section 3.5.

Now that we have explicitly determined the relationship between bulk magnetization and the energy locations of the nodal points, let us try to connect the response to the edge state properties as mentioned earlier. Consider our simple two-node DSM model with $m_A > 0$ on a cylinder with periodic boundary conditions in the trivial direction (y-direction), and open boundary conditions in the topological direction (x-direction). With this choice of orientation the system will exhibit gapless boundary modes. Let us add in the term $\epsilon(k) = \gamma \sin k_y \mathbb{I}$ to generate a non-vanishing b_0. The sample thus has $b_0 = b_0(\Theta(x) - \Theta(x - L_x))$, where we have chosen the cylinder to lie between $x = 0$ and $x = L_x$. The current density near the left-edge ($x = 0$) is given from the response action by

$$j_L^y = -\frac{e}{2\pi} b_0 \delta(x). \tag{3.39}$$

The total current traveling within a region near $x = 0$ is simply $J_L^y = \int_{-\delta}^{\delta} dx j_L^y = -\frac{eb_0}{2\pi}$. Of course, the *total* current in the y-direction will vanish once we take both edges into consideration.

Now we can use this result to compare to the current carried by the edge states. In Fig. 3.4a we show the energy spectrum for the DSM in a cylinder geometry for a non-zero γ, and a non-zero $m_A > 0$. We see that the edge states are attached to the Dirac nodes (slightly gapped by m_A), and their dispersion is $\epsilon_{edge}(k_y) = -\gamma \sin k_y$ (for a derivation see Appendix A.3). When m_A is identically zero, then at half-filling each edge branch will be occupied up to $E = 0$ (which happens at $k_y = \pi$ for our model), and the boundary currents vanish. When $m_A \neq 0$ then the remaining states on the left edge become occupied which generates a current; the other edge will now have an excess of unoccupied (hole) states which produce a current in the opposite direction. If we take the limit as $m_A \to 0$ then the boundary current will persist since the electrons cannot scatter from one edge to the other as long as translation symmetry is preserved, and the edges remain far enough apart to prevent an inter-edge hybridization gap. The edge electrons will remain in their "adiabatically" filled state (in the language of [20]).

Let us now calculate the magnitude of the edge current in these conditions. Explicitly, the current on the left edge when all of the boundary modes are occupied is

$$\begin{aligned} J_L^y &= \frac{e}{2\pi\hbar}\int_{k_{y0}}^{k_{yc}} dk_y \frac{\partial\epsilon_{edge}(k_y)}{\partial k_y} \\ &= -\frac{e\gamma}{2\pi\hbar}[\sin k_{yc} - \sin k_{y0}] \\ &= -\frac{e}{2\pi}[\tfrac{\gamma}{\hbar}(\sin k_{yc} - \sin k_{y0})] = -\frac{eb_0}{2\pi}, \end{aligned} \tag{3.40}$$

where k_{y0} is the energy up to which the edge state is occupied when $m_A = 0$, and k_{yc} is the point up to which the additional occupied states are filled when the entire edge branch is occupied. Thus, we see that on the sides of the system that have topological edge states, the current is completely accounted for by the boundary modes.

As discussed above, the non-vanishing bulk magnetization also implies there should be bound currents on edges that do not have low-energy topological boundary modes. Current conservation also indicates that on finite-sized systems, where all boundaries are open, the edge currents from a gapless edge must flow somewhere after hitting a corner. Indeed this is confirmed in Figs. 3.6,3.7. Though we do not have a simple argument to derive the magnitude of the edge current on non-topological edges, we found numerically that the magnitudes of the currents localized on each edge are the same.

3.5 General formulation of response for 2D DSM

Let us now consider a generic $\mathcal{TI}$-invariant DSM which harbors an even number of Dirac cones. Each Dirac cone D_a ($a = 1, 2 \ldots 2N$) in the semi-metal is specified by the data $(\chi_a, \hbar\bar{\mathbf{K}}_a, \epsilon_a, g_a)$ which are the helicity, momentum-space location of the Dirac node, energy of the node, and the sign of an infinitesimal local mass term at the Dirac point respectively. The helicity indicates whether the winding of the (psuedo)-spin around a Fermi-surface at a Fermi-energy above the node gives rise to a Berry phase of ±π (i.e., $\chi_a = \pm 1$). All of the response coefficients in which we are interested arise from anomalous terms which, even for gapless Dirac nodes, depend on how the gapless point was approached from a gapped phase; this is why we must include the g_a. Another way to think about this is that the choice of g_a determines the sign of the symmetry breaking response for each pair of Dirac nodes.

Let us now consider the generalization of our earlier continuum formula to the case with many flavors.

Following [38], in the ultra-clean limit we can associate a conserved current $j^{\mu}_{(a)}$ to each Dirac cone, and a matching gauge field $A_{(a)\mu}$. Each Dirac cone contributes a term to the effective response action of the form

$$S^{(a)}_{eff}[A_{(a)}] = \chi_a g_a \frac{e^2}{4h}\int d^3x \epsilon^{\mu\nu\rho} A_{(a)\mu}\partial_\nu A_{(a)\rho}. \tag{3.41}$$

This gauge field contains two pieces: (i) the contribution from the electromagnetic gauge potential, and (ii) the energy-momentum shift of each Dirac node. Thus, we have $A_{(a)\mu} = A_\mu + \frac{\hbar}{e}\bar{K}_{(a)\mu}$ where $\bar{K}_{(a)\mu}$ tells us the energy-momentum location of the node such that $\bar{K}_{(a)0} = \epsilon_a/\hbar$, and A_μ is the true electromagnetic vector potential. With this specified, we can rewrite the action in a more transparent manner:

$$\begin{aligned} &S[A, K_{(a)}] = \\ &\frac{e^2}{4h}\sum_{a=1}^{2N}\chi_a g_a \int d^3x\, \epsilon^{\mu\nu\rho}(A_\mu + \tfrac{\hbar}{e}\bar{K}_{(a)\mu})\partial_\nu(A_\rho + \tfrac{\hbar}{e}\bar{K}_{(a)\rho}). \end{aligned} \tag{3.42}$$

Let us now try to extract the important electromagnetic contributions to the response. The term containing only powers of A_μ, and none of $K_{(a)\mu}$, is simply

$$S_1[A] = \frac{C_1 e^2}{2h}\int d^3x\, \epsilon^{\mu\nu\rho} A_\mu \partial_\nu A_\rho \tag{3.43}$$

where C_1 is the total Chern number given by $C_1 = \frac{1}{2}\sum_{a=1}^{2N}\chi_a g_a$. We will not discuss the extra terms in the effective action which are independent of A_μ here. To understand them better we can reformulate the response theory using an analog of the K-matrix formalism familiar from the Abelian Fractional Quantum Hall(FQH) states [102]. This discussion lies outside the main scope of the text and we defer it a brief discussion in Appendix A.7.

To extract the mixed term that represents the charge polarization and magnetization, we will, for simplicity, restrict ourselves to particular configurations of the g_a. When there are more than two nodes, the concept of a single inversion or time-reversal breaking mass term is not clearly defined when given a full set of g_a. One appropriate generalization of the inversion breaking mass is to have the sign of the mass fixed to be the same for *all* nodes. That is $g_a = +1$ or $g_a = -1$ for all values of a. For this choice let us call $g_a = g$ for all a. This choice has some immediate consequences: (i) the total Chern number vanishes, i.e.,

$$C_1 = \frac{1}{2}\sum_{a=1}^{2N}\chi_a g_a = g\frac{1}{2}\sum_{a=1}^{2N}\chi_a = 0 \tag{3.44}$$

since there is a generic constraint $\sum_a \chi_a = 0$ coming from the $T\mathcal{I}$-symmetry of the lattice model; and (ii) the Chern number for any pair of opposite helicity Dirac nodes vanishes. With this constraint we can determine the polarization and magnetization from the band-touching data as discussed below. On the other hand, if we allowed each g_a to have varying signs, the determination of the polarization can be become more complicated since the Chern number of individual pairs of Dirac nodes need not always vanish (c.f. Section 3.6). [3] Henceforth we will fix the all $g_a = g > 0$.

Now, using this choice for the set of g_a we can extract the mixed contribution to the action

$$S_2[A, b] = \frac{e}{2\pi} \int d^3x \, \epsilon^{\mu\nu\rho} b_\mu \partial_\nu A_\rho. \tag{3.45}$$

where

$$b_\mu = \frac{g}{2} \sum_{a=1}^{2N} \chi_a \bar{K}_{(a)\mu}. \tag{3.46}$$

This is the more general formulation of the two node formulae we had derived previously, and the magnetization and polarization are given as $eb_\mu = 2\pi(M, \epsilon_{ij} P_1^j)$.

Eqs. 3.43, 3.45, and 3.46 are the general continuum results, and are similar to the types of formulae one finds for 3D Weyl semi-metals, for example. However, these formulae only provide the correct *bulk* results for a lattice system if there are an even number of edge state branches (on one edge) that pass through the boundary of the edge BZ. This issue is addressed by simply including an extra sign (Θ_j) in the polarization for each spatial direction as discussed above. Given our choice of an edge, this automatically determines a reciprocal lattice vector normal to the edge $\mathbf{G}_N$, and its dual vector $\mathbf{G}_F$ with components $G_{Fi} = \epsilon_{ij} G_{Nj}$. The $\Theta_{\hat{n}}$, which is essentially a weak index, is determined by the Wilson line integral $\Theta_{\hat{n}} = \exp\left[i \int_{\vec{G}_N} a_i(\vec{k}) dk^i |_{k_{edge}=\pi} \right]$, i.e., the line-integral of the adiabatic connection across the Brillouin zone along the momentum direction normal to the edge, and evaluated at $k_{edge} = \pi$ (where k_{edge} is the momentum tangent to the edge). Physically, the quantity $\Theta_{\hat{n}}$ determines whether or not the effective 1D wire Hamiltonian at $k_{edge} = \pi$ has a trivial ($\Theta_{\hat{n}} = +1$) or non-trivial ($\Theta_{\hat{n}} = -1$) polarization. To be explicit, let us consider an orthogonal lattice basis $\vec{a}_1 = \hat{x}$ and $\vec{a}_2 = \hat{y}$ and pick an edge with normal vector $\vec{a}_1$. We have $\vec{G}_N = 2\pi\hat{x}$, $\vec{G}_F = 2\pi\hat{y}$, and k_{edge} runs over all values of k_y. For this choice we have the definitions $\Theta_x = \exp\left[i \int_{-\pi}^{\pi} dk_x a_{k_x}(k_x, \pi) \right]$ and $\Theta_y = \exp\left[i \int_{-\pi}^{\pi} dk_y a_{k_y}(\pi, k_y) \right]$.

---

[3] There is always an ambiguity in determining the boundary charge from the bulk Dirac point data, but in cases where the g_a can be different from each other the problem worsens. Even if the total Chern number vanishes there can be cases where, depending on exactly how the edge states connect between nodes, the system could realize a non-zero Chern number in some pairs of Dirac nodes (such that the total sum vanishes), and just a non-zero polarization in other nodes, i.e., effectively a mix of time-reversal and inversion breaking mass terms for each pair of nodes. The boundary charge in these cases could be determined by combining the types analyses in Sections 3.5 and3.6, but the connection between this charge and the bulk calculation for the polarization is more challenging to derive.

With this correction we arrive at the bulk values of the polarization and magnetization of a DSM, which are valid even in a lattice model:

$$P^i = \frac{e\epsilon^{ij}\Theta_j}{4\pi}\sum_{a=1}^{2N}\chi_a g_a \bar{K}_{a,j} \tag{3.47}$$

and

$$M = \frac{eg}{4\pi}\sum_{a=1}^{2N}\chi_a \epsilon_a. \tag{3.48}$$

Since the magnetization is isotropic, and can even generate currents on edges without low energy edge state branches, we might have anticipated (and we actually confirmed numerically above) that the formula would not be dependent of the values of the weak-indices Θ_j.

While these results are what one would find via a bulk calculation of the polarization and magnetization, we should check whether or not they satisfy the correct physical properties for these quantities. The physical manifestation of the polarization is due to the surface theorem that implies that the boundary charge is proportional to the dot product between the polarization and the normal vector to the edge. Hence, a useful definition of polarization in a DSM should reproduce the correct boundary charge. Similarly the boundary current should be related to the magnetization. We have already carried out this program for two nodes and found, up to some benign ambiguities, the polarization and magnetizations determined from these bulk formulae match the expected boundary charge and current. Let us now discuss the complications that arise when there are more than two nodes.

Since we have already shown how this works out for two Dirac nodes, our goal is to determine the connection between the bulk value of the polarization in Eq. 3.47, and the boundary charge for a generic (even) number of nodes. Unfortunately, as we will note below, when we go beyond four nodes the connection between the bulk value of the polarization and the boundary charge can be a bit byzantine. Ultimately, the boundary charge is decided by the arrangement, and filling, of the low-energy edge states that span between edge-projected Dirac points. When multiple edge branches overlap, a coupling between them, even if it is only localized on the boundary, can dramatically effect the boundary charge. In the most general configuration of nodes, the polarization can be calculated as a sum of the (signed) momentum-space locations of the Dirac nodes projected into the corresponding edge BZ. Unfortunately, the *signs* that enter the linear combination must be determined from the edge state occupation, and do not generically match the bulk result. This is similar to the complication found in [20] where a precise surface theorem for the bulk polarization in a Chern insulator is only defined when the occupations of the edge branches are included. Here the occupation can change at each Dirac point and thus there can be many possibilities for the boundary charge.

The issue of edge state overlap is challenging to deal with, and can have important effects since the edge

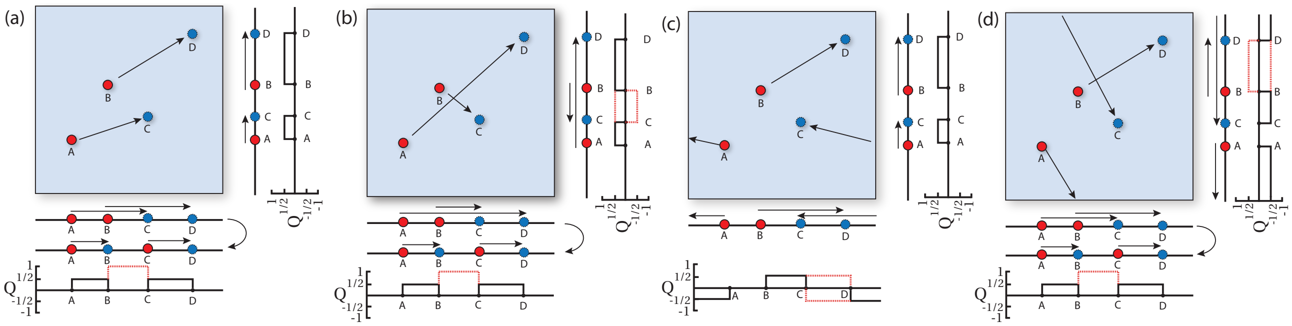

Figure 3.8: In (a) and (b) we show two arbitrary pairings of the four Dirac nodes with opposite (red and blue) helicity in the 2D square lattice BZ. In (c) and (d) we show cases when Θ_i for $i = x, y$ both take their non-trivial values such that the edge states/Dirac node pairing pass through the BZ boundary. Below and to the right of each 2D BZ we show the projection onto the respective edge BZs. In cases where there are overlapping edge states and a $\mathbb{Z}_2$ cancellation we show the resulting modified effective helicities in a second projected edge BZ subfigure. Finally, we show a diagram for each edge state projection showing the calculated boundary charge resolved vs k_{edge} when a uniform half-filled background charge has been subtracted, and in units of e. The black curves show the results after the cancellation of overlapping edge states and the black + red curves show the result if the overlapping edge state regions all contribute. In (c) and (d) there are cases where there are red curves below and above the axes. These are contributions coming from each overlapping edge state which cancel when added together.

states are only stable modulo 2, unlike, for example, the chiral boundary states of a 3D Weyl semi-metal which have an integer classification. If we constrain ourselves to four nodes, then we can determine the correct set of signs that enter the calculation of the boundary charge in the presence of generic couplings between overlapping edge states. We will now present an appropriate $\mathbb{Z}_2$ modified construction that captures a well-defined value for the boundary charge as determined from the bulk nodal data. Our result shows that using Eq. 3.47 is still valid as long as one replaces the set of helicities χ_a with a modified set $\bar{\chi}_a$ (to be defined below) that takes into account the $\mathbb{Z}_2$ cancellation. The modified set of helicities depends on the particular edge projection of interest, and can be easily determined from our construction below.

The construction is as follows. First, given a set of Dirac nodes in the bulk, we choose an arbitrary pairing between the nodes with opposite helicity (the reason they have to be opposite helicity is that the edge states always traverse between nodes with opposite helicity). This is always possible since there are an even number of nodes, and an equal number with positive and negative helicity. The final result will not depend on how this pairing is chosen (modulo the ambiguity of the polarization to adding occupied bands with quantized polarization) as long as the sign of g_a is the same for all nodes (otherwise we have to worry about pairs of nodes contributing a non-vanishing Chern number instead of a polarization). Next, depending on the value of $g = +1(-1)$ we draw oriented lines between each nodal pair with the arrow pointing from the negative helicity to the positive helicity (positive helicity to negative helicity). The oriented lines should not cross the boundaries of the Brillouin zone that is centered at the Γ-point (for now). We show two examples

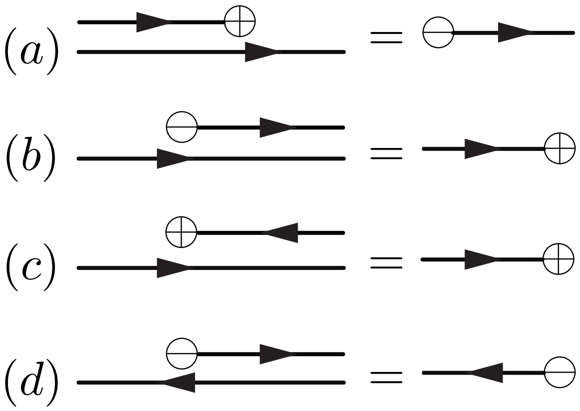

Figure 3.9: Rules for helicity modifications and line removal for use with the determination of the boundary charge for Dirac semi-metals with four nodes. The signs inside the enclosed circles represent the helicities, and the oriented arrows refer to the nodal pairing in the text.

of this in Fig. 3.8a,b for two different choices of nodal pairs.

Now, if we want to calculate the boundary charge, we begin by projecting the energy spectrum onto the associated edge Brillouin zone. This will generate the nodal locations in the edge Brillouin zone, as well as projections of the oriented lines (as shown in the subfigures in Fig. 3.8a,b,c,d). It is at this stage that the complications begin. If the projections of the oriented lines do not overlap at any point in the edge Brillouin zone, then one can calculate the boundary charge by: (i) multiplying the length of the each of the oriented lines in momentum space by $\frac{e}{2}\frac{1}{2\pi}$, (ii) then multiplying the result by a sign that is +1 if the oriented line points from left-to-right in the projected edge Brillouin zone or −1 if it points from right-to-left, (iii) and subsequently adding up all of the contributions for all of the pairs of nodes/oriented lines.

However, if there are some overlapping lines then we have to carefully handle the general $\mathbb{Z}_2$ cancelation, which we can eventually take into account by flipping the helicities of some of the nodes.[4] To determine which helicities should be flipped, we can use the following procedure. For each Dirac node there is one line emanating from itself to its partner. If the number of lines overlapping a Dirac point with the same orientation is even (including its own), then we must flip its helicity, otherwise we leave it unchanged.

In both cases, i.e., whether or not the helicity is flipped, we remove the oriented lines for intervals where there an even number of overlapping lines, which *always* leaves alternating intervals. We show the general rules for flipping helicities in the schematic diagrams in Fig. 3.9. We can subsequently take these newly determined helicities and plug them into Eq. 3.47 to generate a value for the polarization that satisfies the

---

[4] Of course, there could be cases with overlapping edge states that do not cancel each other, but to be generic this will require some symmetry. For example, if one edge state carries spin up, and the other carries spin down, then spin-rotation symmetry could protect from the cancellation. However, this is essentially just converting the edge state stability from $\mathbb{Z}_2$ to $\mathbb{Z}$. Instead, we will consider the generic case without extra symmetries so that the cancellation is taken to always occur for overlapping edge states.

surface theorem normal to the chosen edge. We note that this process must be carried out for each choice of edge individually, and the modified helicities for one edge may not work for a different edge. We see an example of this in Fig. 3.8a where when projected onto the x-axis the helicities of nodes B and C are changed, while for the projection onto the y-axis, none of the nodes have modified helicities. If we now remove the regions over which pairs of overlapping lines exist, as exemplified by the rules in Fig. 3.9, the boundary charge can be determined geometrically from the remaining oriented lines as in the non-overlapping case, or simply by plugging into the polarization formula with the modified helicities.

So far this algorithm still misses an important possibility that we have discussed earlier, namely the possibility that the edge states pass through the boundary of the edge Brillouin zone $k_{edge} = \pi$ instead of the origin. We can take these effects into account in our geometric algorithm above by making a simple extension. If $\Theta_{\hat{n}}$ takes its non-trivial (trivial) value then an odd (even) number of oriented lines should pass through the Brillouin zone boundaries normal to $\mathbf{G}_N$. This generalizes our discussion above where we have shown zero lines (i.e., an even number) passing through the Brillouin zone boundary. We show some examples of non-trivial Θ_x and Θ_y in Fig. 3.8c,d. The results are independent of which oriented lines are chosen to pass through the Brillouin zone boundary (modulo the ambiguities in the polarization discussed above). If one does not want to include any information about the occupied bands, i.e., does not, or is not able to, calculate $\Theta_{\hat{n}}$, then the overall sign of the polarization is ambiguous, as well as the addition of a quanta of $e/2$ boundary charge per unit cell which could arise from fully occupied bands carrying a weak invariant. However, this ambiguity essentially exists anyway since one could layer an extra 2D weak TI on top of the 2D DSM and couple the modes of the weak TI to those of the DSM and effectively change between the different values of $\Theta_{\hat{n}}$. Thus, maybe the main advantage to knowing $\Theta_{\hat{n}}$ is to compare with numerical calculations of model systems where a precise model has been specified, and the total weak invariant of the occupied bands is unambiguously specified.

While this algorithm works for four nodes (some extra details are given in the caption of Fig. 3.8), with six nodes or higher the algorithm is not independent of how the Dirac nodes are chosen to be paired, and it can also give ambiguous results when there are more than two sets of edge states overlapping in a single region. Even if one knows precisely how the edge states connect between the different nodes, e.g., by diagonalizing the system with open boundaries, and thus how the Dirac nodes are "paired," the sign of the polarization due to regions of the edge BZ with more than two overlapping edge states depends in detail on the coupling between those edge states. In fact, one can effectively switch the signs of the helicities of the Dirac nodes in pairs (not necessarily the same pairs that are connected via edge states) by modifying boundary terms that couple the different DSM edge state branches. The final value for the polarization is still a signed sum of the momenta of the bulk Dirac nodes, but the signs that determine the boundary charge have to be determined from the occupation of the edge state branches, similar in spirit to what is done for the Chern insulator in [20]. We expect this type of issue to arise whenever the edge states are $\mathbb{Z}_2$ stable as opposed to $\mathbb{Z}$ stable in the chiral case.

Similar complications can arise for the magnetization. The boundary current can depend on the how different pairs of edge states are coupled to each other, and on the precise filling of the edge states. Since the edge states are dispersing, even more complicated configurations can arise where the edge states enter the bulk bands arising from other sets of Dirac nodes. It quickly becomes tedious trying to numerically match the boundary current calculation to a bulk result since it depends on both the energies and occupations of the edge states, which can be affected in many ways. In some simple cases where the edge states do not enter the bulk bands, and hence, the occupation of the edge states change at the Dirac nodes themselves, then the bulk result can be recovered. We leave it to future work for an exhaustive treatment of generic edge state configurations.

3.6 General comments about the 2D Dirac semi-Metal response

(i) Symmetries of b_μ in 2D: Let us discuss the transformation properties of b_μ under time-reversal (T), charge-conjugation (C), and inversion symmetry ($\mathcal{I}$). Since in 2D we know that b_0 is proportional to a magnetization, and b_i is proportional to a polarization, we can easily determine their symmetry properties:

$$\begin{aligned} T &: \quad b_0 \to -b_0 \\ C &: \quad b_0 \to b_0 \\ \mathcal{I} &: \quad b_0 \to -b_0 \end{aligned} \tag{3.49}$$

and

$$\begin{aligned} T &: \quad b_i \to b_i \\ C &: \quad b_i \to b_i \\ \mathcal{I} &: \quad b_i \to b_i. \end{aligned} \tag{3.50}$$

Note that they are both even under C, which is due to the fact that our convention for b_μ in 2D still has the charge factored out. The other thing to note is that $M \sim \text{sgn}(m_A) b_0$ and $P_1^i \sim \text{sgn}(m_A)\epsilon^{ij} b_j$ and $\text{sgn}(m_A)$ is odd under inversion (and parity). When this is taken into account we find that M and P_1^i transform appropriately. In fact, the symmetry properties of b_μ in 2D match those in 1D.

(ii) Comments on the electromagnetic response: The response actions in this section all essentially depend on derivatives of b_μ. Thus, for a homogeneous system there is no charge or current response. This pattern alternates between spatial dimensions. In 1D, 3D, 5D,. . . , when the low-energy Fermi surfaces are represented by chiral/Weyl nodes, then the electromagnetic response will be a bulk phenomena that does not depend on derivatives of b_μ whereas in 2D, 4D, 6D,. . . when the Fermi-surface arises from Dirac nodes, then the response depends on derivatives of b_μ which are most commonly generated at interfaces and boundaries.

(iii) Dependence of the response coefficients on shifts of the origin of the Brillouin zone or the energy reference point: One might be worried that defining physical quantities in terms of the energy/momentum locations of the nodal points might be problematic since the definitions might depend on arbitrary choices of, e.g., the origin of the BZ or the zero-reference point for energy. Let us consider changing both of these to see what effects they have. In fact, most of the results that follow have been discussed extensively in [13, 20], albeit in a slightly different context, and we go through their arguments here for completeness. For our purpose here we will ignore the complication of the $\mathbb{Z}_2$ cancellations.

To illustrate the point, let us take $\bar{K}_{(a)\mu} \to \bar{K}_{(a)\mu} + \Delta k_\mu$. Let us consider the spatial components of b_μ first, which are related to the polarization $\vec{P}_1$. We can write down the polarization in terms of Bloch wave functions as

$$\vec{P}_{1[\vec{k}_0]} = \frac{e}{(2\pi)^2}\mathrm{Im}\int_{[\vec{k}_0]} d^2k \,\langle u_k|\nabla_k|u_k\rangle \tag{3.51}$$

where we have included the dependence of the origin of the BZ by $\vec{k}_0$. Under a change of the origin from $\vec{k}_0 \to \vec{k}_0 + \Delta\vec{k}$, it can be shown generally [20] that the polarization changes by

$$\vec{P}_{1[\vec{k}_0+\Delta\vec{k}]} = \vec{P}_{1[\vec{k}_0]} - \frac{eC_1}{2\pi}\hat{z}\times\Delta\vec{k} \tag{3.52}$$

where C_1 is the first Chern number. Thus, we see that the polarization itself can seemingly depend on the choice of the origin of the BZ, but only when the Chern number is non-vanishing. When discussing the polarization for the 2D DSM we have been careful to require that $C_1 = 0$ and, hence we never have this problem. However, even for non-vanishing Chern number it turns out that this issue can be resolved. In fact, there is a discussion in [20] about a well-defined polarization for Chern insulators. To make sense of this, those authors showed that we need to recall that what is physically meaningful is the *change* in polarization under an adiabatic change of an internal parameter of the system. They show that as long as the same origin in the BZ is used for measuring the initial and final polarization of the system, the results remain consistent.

It is interesting that in our case we find that a shift of $\vec{k}_0$ in Eq. 3.46 produces exactly the same result as Eq. 3.52. That is, under $\bar{\mathbf{K}}_{(a)} \to \bar{\mathbf{K}}_{(a)} + \Delta\mathbf{k}$, we see that

$$\Delta P_1^i = \frac{e\epsilon^{ij}}{4\pi}\sum_{a=1}^{2N}\chi_a g_a \Delta k_j = \frac{eC_1\epsilon^{ij}\Delta k_j}{2\pi} \tag{3.53}$$

which is the same as Eq. 3.52, even with a non-zero Chern number. Thus, the effective $\vec{b}$ can change when the origin of the BZ is re-defined, but only if the Chern number is non-vanishing. In this case it is shifted according to the formula derived in [20] for the charge polarization in a Chern insulator, and any possible ambiguity can be dealt with along those arguments without any issues.

Now, we look into what happens with the time component of b_μ. Increasing b_0 at a Dirac node is equivalent to reducing the chemical potential at the node or shifting the reference of zero-energy for that point. For the purposes of calculations we can interpret a shift in the global reference point in energy as a global change to the chemical potential for the overall system. The magnetization for a Bloch system is defined to be

$$\begin{aligned} M = {} & \frac{e\epsilon^{ij}}{2\hbar}\int\frac{d^2k}{(2\pi)^2} \\ & \times \mathrm{Im}\sum_n \int_{\epsilon_{nk}\leq\mu} \langle\partial_{k_i}u_{nk}|H_k + \epsilon_{nk} - 2\mu|\partial_{k_j}u_{nk}\rangle. \end{aligned} \tag{3.54}$$

Following [13], we see from this relation that

$$\begin{aligned} \frac{dM}{d\mu} &= -\frac{eC_1}{h} \\ \implies \Delta M &= -\frac{eC_1\Delta\mu}{h}. \end{aligned} \tag{3.55}$$

In fact, this general result exactly matches what we find from our definition of b_μ. Under $\bar{K}_{(a)0} \to \bar{K}_{(a)0} - \frac{\Delta\mu}{\hbar}$, we see that

$$\begin{aligned} \Delta b_0 &= -\frac{1}{2\hbar}\sum_{a=1}^{2N}\chi_a g_a \Delta\mu \\ \implies \Delta M &= -\frac{eC_1\Delta\mu}{h}. \end{aligned} \tag{3.56}$$

Thus, we again see that b_0 changes under a redefinition of the origin of energy, but only when the Chern number is non-zero. In this case it changes in the exact same way as a non-trivial Chern insulator.

(iv) Polarization in a Chern Insulator: Finally, before moving onto the 3D cases, we will discuss a related system with just two Dirac nodes, and non-vanishing time-reversal and inversion-breaking masses. This case, which represents a Chern insulator with broken inversion symmetry, was discussed in [20, 13] where they have defined an electric polarization/magnetization for a Chern insulator. The exact details of the model they considered are a bit different since they use the honeycomb Haldane model [37] with both a nonzero inversion breaking Semenoff mass, and a time reversal breaking Haldane mass. In fact, they tune the size of the Haldane mass by changing an adiabatic parameter α. What this translates to in the context of our DSM model on the square lattice is that they are working with both an m_A and an m_B turned on. In our language the analogous Hamiltonian is

$$H = \sin k_x \sigma^x + (-m_A + m_B(\alpha) \sin k_y)\sigma^y + (1 - m - \cos k_x - \cos k_y)\sigma^z \tag{3.57}$$

where $m_B = m_A(1 + \alpha)$ is tuned as a function of the adiabatic parameter α.

Now let us describe the polarization of this system in terms of the edge state filling. As shown in Appendix A.2, the energy of the edge states, on edges parallel to the y-direction, is given by $E_{L/R}(k_y) = \pm(m_B \sin k_y - m_A)$ where the ± signs are correlated with the left/right edges. In the limit that $m_B \neq 0, m_A = 0$, we have a Chern insulator which is completely inversion symmetric. If we fill all the states with $E \leq \mu = 0$ on the edge, then there will be an equal number of filled edge states on both edges, and hence a vanishing polarization. When we turn on an m_A, the energy of the edge states is shifted, and filling all the edge states with $E \leq \mu$ creates an imbalance between the two edges depending on how large m_A is. In this case, there are more edge states filled on one edge compared to the other, which leads to a polarization (and possibly magnetization if the nodal energies are shifted). This effect is illustrated in Fig. 3.10 where we compare the edge spectrum with and without an m_A turned on. The plot has parameters $b_y = \pi/3, m_A = 0, 0.1$ and $m_B = 0.2$. The crossing of the edge states moves to the right as we start increasing the m_A.

In the case when both the masses are finite, we can think of this polarization/magnetization as still arising from an energy and momentum difference, but modified from its original value of b_μ to new a value we will call Φ_μ. The spatial component is given by $\Phi_i = \sin^{-1} \frac{m_A}{m_B}$. When there is a $T\mathcal{I}$-breaking term $t_p \sin k_y \mathbb{I}$ in our Hamiltonian, we will also generate a magnetization dependent on $\Phi_0 = t_p \frac{m_A}{m_B}$. Of course, since the edge states exist between the bulk Dirac nodes this heuristic description only makes sense when Φ_μ is lesser than the b_μ coming from the original gapless bulk Dirac nodes. In the semi-metallic limit where $m_A, m_B \to 0$, the polarization/magnetization will actually depend on the ratio of the masses $\Xi = m_A/m_B$ as they are tuned to zero. When the time reversal breaking mass is much greater than

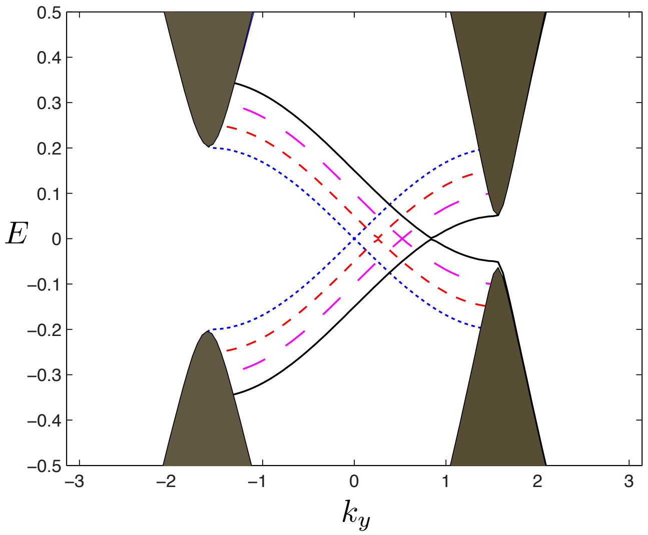

Figure 3.10: We illustrate the dispersion of the edge states of the model $H = \sin k_x \sigma^x + (m_B \sin k_y - m_A)\sigma^y + (1 - m - \cos k_x - \cos k_y)\sigma^z$ in the limits $m_A = 0, 0.05, 0.10, 0.15, m_B = 0.2$ with various dashed lines. The Dirac nodes are located at $\pm\frac{\pi}{2}$. The crossing point has shifted to a nonzero k_y once we turn on an inversion breaking mass and moves towards one of the Dirac points as m_A is increased further. This leads to a non-zero polarization which is decided by the ratio of m_A and m_B, while the sign of the polarization is decided by m_A.

the inversion breaking mass, the polarization and magnetization depend on the quantity Φ_μ instead of b_μ. However, in the limit that the inversion breaking mass is much greater than the time reversal breaking mass, the polarization/magnetization will depend only on the b_μ derived from the locations of the Dirac nodes in the gapless limit as we have discussed throughout this section. There is a switch between the two different behaviors when $m_A = m_B \sin k_c$ where k_c is a location of a Dirac node in the gapless limit. In either case, there is no polarization/magnetization without turning on an inversion-breaking mass.

In our general discussions above, if we allowed for the set g_a to take generic values, then to calculate the polarization we would have to use a combination of the results for vanishing Chern number and non-vanishing Chern number on a case by case basis for each region of the edge BZ with edge states.

Chapter 4

3D point-node topological semimetals

There has been a series of recent works that lay out the theory of electromagnetic response in Weyl semimetals(WSM) [114, 34, 98, 16, 38, 15, 96] and build on the seminal ideas of Nielsen and Ninomiya from three decades ago [69]. We will compliment these results in several ways. First, we include lattice-regularized numerical calculations of the response, which show precisely under what conditions the continuum field-theory response calculations can be applied, and most notably when a non-zero current due to the Chiral Magnetic Effect (CME) can be observed in lattice models. We connect the numerical results with our earlier discussion of the 1D semi-metal using a map between the 3D Weyl semi-metal in a uniform magnetic field, and many degenerate copies of the 1D semi-metal, which can be applied at low-energy. We also provide an analytic description of the boundary modes for a lattice model of the Weyl semi-metal, the response behavior of a hetero-junction between two different Weyl semi-metals, and a discussion of the anomaly cancellation which connects the bulk and surface response.

Following this we move on to consider the response of 3D Dirac semi-metals in Section 4.2. Since there is not a similar Nielsen-Ninomiya no-go theorem for lattice Dirac fermions, the Dirac semi-metals can come in different varieties. The first type has the Dirac node(s) appearing at the special time-reversal invariant momenta in the Brillouin zone. This type is reported to have been realized in Cd_3As_2 [68, 101]. The other variety is more closely related to the WSM, and is essentially a time reversal and inversion symmetric version of the WSM where each Weyl node, which exists at generic points in the Brillouin zone, is replaced by two copies of the Weyl node, but with opposite chirality, i.e., Weyl nodes are replaced by 3D Dirac nodes at generic points in the Brillouin zone. These have recently been confirmed experimentally in Na_3Bi [60].

It is this second type, which was recently dubbed a Z_2 non-trivial 3D DSM [107], to which our response theory applies, and unfortunately it is yet to be realized in real material samples. We will predict a quasi-topological electromagnetic response for these materials which is related to the known electromagnetic response of the quantum spin Hall insulator [74, 75]. In particular, we discuss the response of the 3D DSM when there is a magnetic film in contact with the sample surface. Magnetization domain walls on the surface can generate a line of zero modes along the domain wall and hence give rise to some transport phenomena in these materials including bound charge and currents. We have seen that when discussing Dirac semi-metals, we must enforce extra symmetries to provide local stability for the nodes. In 3D, to guarantee local stability of the Dirac nodes, one must require several preserved spatial symmetries, and only certain crystalline space groups support stable nodes [110, 107], though we will not focus much more on this in thisthesis.

4.1 Response for 3D Weyl semi-Metal

A simple model for the WSM phase can be formulated with two bands

$$H_{WSM} = \gamma \sin k_z \mathbb{I} + \sin k_x \sigma^x + \sin k_y \sigma^y + (2 - m - \cos k_x - \cos k_y - \cos k_z)\sigma^z. \tag{4.1}$$

This model has two Weyl nodes at $(k_x, k_y, k_z) = (0, 0, \pm\cos^{-1}(-m))$. The identity matrix term generates a difference in energy between the nodes. Around the two nodes, we have linear dispersion $\epsilon_\pm \approx \pm v_F|\mathbf{k}|$, and each of the nodes acts as a monopole of Berry curvature. The Berry curvature flux contained in a Fermi-surface surrounding each node can be $\pm 2\pi$ depending on whether the node enclosed is of positive or negative chirality. This property also leads to surface states whose Fermi-surfaces consist of open line-segments traveling between the projections of the nodes onto the surface Brillouin zone [99]. As mentioned before, we follow the convention used in [114] and define $\vec{b}$ as half the momentum separation in the Weyl nodes, and b_0 to be half the energy difference between them (when there are more than two nodes this needs to be appropriately generalized). So, in the two band model we have here, $b_z = \cos^{-1}(-m)$ and $b_0 = (\gamma/\hbar)\sin b_z$.

To calculate the electromagnetic response we can use a continuum description of two Weyl nodes. Following the calculation in [114], in the continuum approximation we have the following low-energy four-band Hamiltonian

$$H = \tau^z \vec{\sigma} \cdot \vec{k} + \tau^z b_0 + \vec{\sigma} \cdot \vec{b}. \tag{4.2}$$

When written as a Lagrangian density coupled to an electromagnetic gauge field the four vector $b_\mu = (b_0, \vec{b})$ appears as an axial gauge field in the action

$$S[b, A] = -\int d^4x\, \overline{\psi}(i\partial\!\!\!/ - eA\!\!\!/ - b\!\!\!/\gamma^5)\psi, \tag{4.3}$$

just as it does in the one dimensional case. We can remove the field b_μ through a chiral rotation, and hence use the Fujikawa method to evaluate the chiral anomaly which appears due to the non-invariance of the measure under this finite chiral transformation. This is very similar to the derivation we had for the one dimensional model. This calculation gives us a hint that breaking Lorentz invariance, as we have done in the 1D model, is an essential part of the mechanism to produce a non-zero response. The response action was calculated to be [114]

$$S_{eff}[A] = -\frac{e^2}{2\pi h}\int d^4x\,\epsilon^{\mu\nu\rho\sigma}b_\mu A_\nu \partial_\rho A_\sigma. \tag{4.4}$$

We can easily interpret the form of the effective response action since it appears just like an interpolation between the WTI phase generated from a stack of 2D Chern insulators, and the normal insulator phase, as was discussed in Section 1.1. The current and charge density, assuming b_μ is homogeneous in space-time, are given by

$$\rho = \frac{e^2}{\pi h}\vec{b}\cdot\vec{B} \tag{4.5}$$

$$\vec{j} = \frac{e^2}{\pi h}\left(\vec{b}\times\vec{E} - b_0\vec{B}\right). \tag{4.6}$$

The term in the current involving the electric field is the anomalous QHE of the WSM. The other terms depend on the magnetic field $\vec{B}$, and can be easily interpreted using an analogy to the 1D semi-metal as we will now show.

4.1.1 Understanding the Weyl semi-metal response using a quasi-1D description

To make the mapping to the 1D system we need to apply a uniform magnetic field to the 3D WSM. Consider the two band model with $b_z \neq 0$. Let us assume that we have a magnetic field turned on in the z-direction so that we have $F_{xy} = -B_z$. It is well-known, and we reproduce the calculation below, that a Weyl node in a uniform magnetic field has a low-energy zeroth Landau level with dispersion $E_0 = \chi k_z - b_z$ near the Weyl node with chirality χ. It is this level that is responsible for the low-energy electromagnetic response in Eq. 4.5. We see that the zeroth Landau level only disperses along the magnetic field direction, and passes through the Weyl node with the direction of the Fermi velocity given by the chirality of the node. Thus, the application of the uniform magnetic field generates a quasi-1D mode at low-energy. For a pair of Weyl nodes, as would be found in the simplest WSM, there are two low-energy branches, which, together, effectively form the same low-energy theory as many copies of the 1D (semi-) metal discussed earlier. Thus, the low-energy description is almost identical to the previous 1D semi-metal discussion, except that each state has a degeneracy which is set by the total flux of the magnetic field through the x-y plane. We denote this degeneracy by $N_\Phi = \frac{B_z L_x L_y}{\Phi_0}$ where $\Phi_0 = \frac{h}{e}$ is the fundamental flux quantum. Thus, in a uniform magnetic field, the low-energy physics of the WSM is equivalent to multiple copies of the 1D semi-metal. As will be seen below, the description is even more apt because, in a lattice regularized model, the zeroth Landau level modes arising from each Weyl node connect at high energy and form multiple copies of the usual 1D tight-binding bandstructure.

Let us try to reproduce the charge density predicted in Eq. 4.5 by using the 1D model. There is a subtlety as to how the states are filled. Of course, if the zeroth Landau level is completely filled or completely empty, then there will be no interesting response. In this case there will be a background charge density of some integer charge per unit cell, but no current will flow in the filled band, and thus there will be no static chiral magnetic effect. This was discussed in detail in [98]. While a filled band can give rise to Lorentz violation because of the inherent lattice structure (e.g. the spatial components of b_μ can be half a reciprocal lattice vector), the field theory calculations for the semi-metal are not sensitive to this. In fact, they can only predict the response from a partially filled band which provides an explicit fractional amount of Lorentz violation (fractional meaning a fraction of a fully-filled band). This is similar to the idea of [39] in which the low-energy structure only determines the fractional part of the response. To match the field-theory calculation we need to assume that the zeroth Landau level is only filled to a chemical potential $\mu = 0$, which implies the band is partially filled. For example, to calculate the density response we need to count the number of states filled in the zeroth Landau level which is simply

$$Q = N_\Phi e L_z \int_{-b_z}^{b_z} \frac{dk_z}{2\pi} \tag{4.7}$$

$$\implies \rho = \frac{e^2 b_z B_z}{\pi h} \tag{4.8}$$

which matches Eq. 4.5. Before we attempt to understand the properties which lead to a nonzero current, let us look at the zeroth Landau level structure of the WSM in more detail to see how b_0 fits into the discussion.

4.1.2 Zeroth Landau Level Structure in a Weyl Semi-metal

In this Section, we proceed to show that b_0 can be thought of in a similar way as what we discussed in Sec. 2 for the 1D model. In the usual case a b_0 is produced by shifting the Weyl nodes in energy with respect to each other. We will show that when this is the case, the zeroth Landau level is shifted in momentum parallel to the magnetic field. So, shifting the nodes in energy acts like an electric field (k is shifted) on the zeroth Landau level. As in 1D we can also generate a b_0 by adding an intrinsic term which generates a velocity difference in the dispersion at the two Weyl nodes; we will discuss this case as well. We will now show some continuum calculations to justify these statements, and then reproduce the same by a simple numerical lattice calculation.

Consider a four band continuum model for the Weyl semi-metal (a single pair of nodes) where only $b_z \neq 0$ [114]. A possible Hamiltonian is given by

$$H = \tau^z \otimes \sigma^x k_x + \tau^z \otimes \sigma^y k_y + \tau^z \otimes \sigma^z k_z + b_z \mathbb{I} \otimes \sigma^z. \tag{4.9}$$

To illustrate the effects of a non-vanishing b_0 (which will be introduced below), we need to include a magnetic field with $k_i \to k_i - eA_i$ and $A_y = B_z x$, where B_z is the uniform magnetic field in the z-direction. We note that we have broken translation invariance in the x-direction with our choice of Landau gauge, and the eigenvalue equation will be a differential equation in x where we have to replace $k_x \to -i\partial_x$. From now on, this is implicitly assumed. The time independent Schrodinger equation reads

$$H\psi = E\psi. \tag{4.10}$$

Following the usual strategy, we can apply H to ψ again to produce $H^2\psi = E^2\psi$. We can evaluate the left hand side to find

$$H^2\psi = [k_x^2 + eB_z \mathbb{I} \otimes \sigma^z + (eB_z)^2(x + k_y/eB_z)^2 + k_z^2 + 2b_z k_z \tau^z \otimes \mathbb{I} + b_z^2]\psi. \tag{4.11}$$

The wave function ψ can be taken to be an eigenstate of σ^z for the spin sector, and τ^z for the orbital sector. Let us denote the eigenvalue of σ^z as $\zeta = \pm 1$, and the eigenvalue of τ^z as $\chi = \pm 1$. Then Eq. 4.11 is just the harmonic oscillator eigen-equation and has the following energies:

$$E_n(\zeta, \chi, k_z) = \pm \left[2eB_z(n + \frac{1}{2}) + (k_z + \chi b_z)^2 + eB_z\zeta\right]^{1/2} \tag{4.12}$$

with the corresponding wave functions given by

$$\Phi_n(\zeta, \chi, \vec{x}) = N_n \zeta \mathrm{e}^{-ik_y y - i(k_z + \chi b_z)z} F_n(x + k_y/eB_z) \times \eta \tag{4.13}$$

where N_n is a normalization constant, $F_n(x)$ are the Hermite polynomial wave functions, and $\eta = \Lambda(\sigma^z) \otimes \Lambda(\tau^z)$ is a four-component spinor where $\Lambda(\pm 1)$ mean the eigenvectors of σ^z, τ^z given by $\left(\begin{smallmatrix}1\\0\end{smallmatrix}\right), \left(\begin{smallmatrix}0\\1\end{smallmatrix}\right)$.

To be precise, we need to verify that all of these solutions satisfy Eq. 4.10. This consistency check eliminates half of the *zero-mode* solutions, and we end up with the result that the zeroth Landau levels have energy

$$E_0 = \chi k_z - b_z \tag{4.14}$$

which depends on the chirality χ of the Weyl node. This dispersion hits zero energy at $k_z = \pm b_z$, i.e. the location of the Weyl nodes, as expected. These modes also have a degeneracy of N_Φ for each value of k_z as noted above. In a lattice regularization the zeroth Landau levels of the two Weyl nodes will be connected to each other at high-energy (c.f. the energy spectrum in Fig. 4.1).

Now, to turn on a b_0 we can add the extra term $\delta H = b_0 \tau^z \otimes \mathbb{I}$, which commutes with the initial Hamiltonian. Since it commutes with the original Hamiltonian its primary effect is to shift the energies of the eigenstates. We note that acting on the zeroth Landau level wavefunctions the energy is shifted by $b_0\chi$, thus leading to the dispersions

$$E_0 = \chi(k_z + b_0) - b_z. \tag{4.15}$$

This is just a shifted version of the original zeroth Landau level dispersions, and they cross zero energy when $k_z = -b_0 \pm b_z$. So, the conclusion is that b_0 shifts the low-energy spectrum of the zeroth Landau level to the right in momentum space, which is the same effect that an external electric field E_z would have. Thus, if the band is partially filled, i.e. when we have explicit Lorentz violation due to the background charge density, this will lead to a non-vanishing current in the presence of an applied B-field, but in vanishing applied electric field, which is essentially the chiral magnetic effect.

Further pushing the 1D description, let us also show that modifying the relative velocities of the two Weyl points will lead to a similar effect. Consider the Hamiltonian given by

$$H = \tau^z \otimes \sigma^x k_x + \tau^z \otimes \sigma^y k_y + \tau^z \otimes \sigma^z k_z + \mathbb{I} \otimes \sigma^z \alpha k_z + \mathbb{I} \otimes \sigma^z b_z \tag{4.16}$$

where $\alpha \ll 1$. This α-dependent term modifies the velocities of propagation in the z-direction of the two Weyl nodes. It effectively changes $b_z \to b_z + \alpha k_z$ from our previous analysis. The entire argument for the energies of the zeroth Landau levels from before carries through here too, and we find a modified zeroth Landau level dispersion of

$$E_0 = \chi k_z - b_z - \alpha k_z. \tag{4.17}$$

This dispersion crosses zero at $k_z = b_z/(\chi - \alpha) \approx \chi b_z - \alpha b_z + \mathcal{O}(\alpha^2)$. So, near zero energy this term behaves like a momentum shift in the Landau level, and this should give us a non-zero current as we have shown in the 1D model in Section 2.

To verify these continuum results, we can perform calculations using a simple lattice regularization of

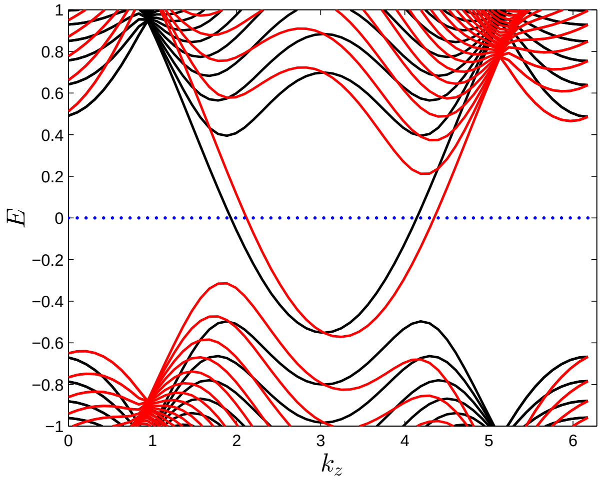

Figure 4.1: The zeroth Landau level of the Weyl semi-metal in a uniform magnetic field is plotted vs k_z before(in black) and after(in red) switching on a γ which gives us $b_0 = (\gamma/\hbar)\sin 2\pi/3 = 0.17$. The blue line is shown to indicate $E = 0$. The model parameters have $b_z = 2\pi/3, m = 1/2$, and $L_x = L_y = L_z = 60$ with the magnetic flux per unit cell given by $\phi = 2\pi/60$. b_0 was then switched on to plot the curve in red. We see that the Landau level is simply shifted in momentum space and is akin to turning on an external electric field in the 1D model.

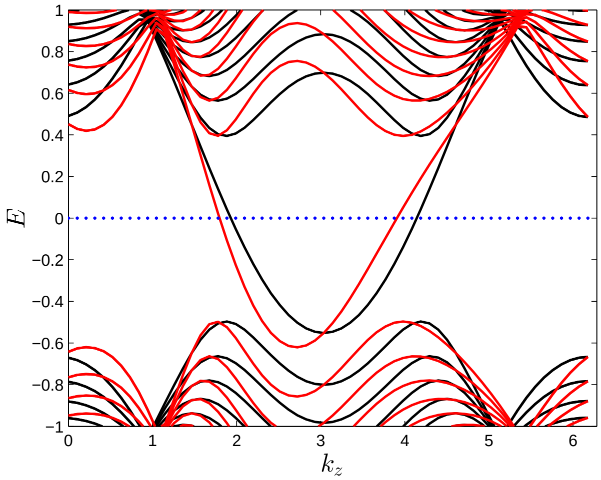

Figure 4.2: The zeroth Landau level is plotted vs k_z before(in black) and after(in red) switching on a b_0 using the NNN velocity term. The blue line is shown to indicate $E = 0$. The model had $b_z = 2\pi/3, m = 1/2$, and $L_x = L_y = L_z = 60$ with $\phi = 2\pi/60$. We then switch on a term to change the velocity of the two Weyl nodes with $t_{NNN} = 0.2$. The shift we expect is then given by $2t_{NNN}m \approx 0.2$ as seen in the figure. In effect, near $E = 0$ the zeroth Landau level is shifted.

the above continuum model. The Hamiltonian is given by

$$H = \gamma \sin k_z \mathbb{I} + \sin k_x \sigma^x + \sin k_y \sigma^y + (2 - m - \cos k_x - \cos k_y - \cos k_z - t_{NNN} \sin 2k_z)\sigma^z \tag{4.18}$$

where the term proportional to γ will cause a shift in energy of the Weyl nodes, and the next nearest neighbor term proportional to t_{NNN} causes a change in the velocity of the zeroth Landau level near the two Weyl nodes.

For $\gamma = 0$ and $t_{NNN} \neq 0$ the Weyl nodes are given by solving

$$\cos k_z + t_{NNN} \sin 2k_z = m, \tag{4.19}$$

which gives us two solutions for k_z. Let us try to extract the low-energy Hamiltonians near the nodes in the limit that $t_{NNN} \ll 1$ by writing the two solutions as $k_z = \pm\kappa_z + \delta k$. We have

$$\cos(\pm\kappa_z + \delta k) + t_{NNN} \sin(\pm 2\kappa_z + 2\delta k) = m. \tag{4.20}$$

We can subtract the two equations to find

$$2 \sin \kappa_z \sin \delta k - 2t_{NNN} \cos 2\delta k \sin 2\kappa_z = 0. \tag{4.21}$$

Using the small angle approximations $\sin \delta k \approx \delta k, \cos 2\delta k \approx 1$, we are left with

$$\delta k = 2t_{NNN} \cos \kappa_z \approx 2t_{NNN} m. \tag{4.22}$$

Thus we see that a non-zero velocity change will lead to a momentum shift of $2t_{NNN}m$ at the nodal energies. Comparing with the continuum calculation we see that $\alpha b_z = -2t_{NNN}m$.

We show the numerical results of $\gamma = 0.2$, $t_{NNN} = 0$ in Fig. 4.1, and $\gamma = 0$, $t_{NNN} = 0.2$ in Fig. 4.2. In both cases we see that near $E = 0$ the zeroth Landau levels are shifted.

4.1.3 Response and anomaly cancellation in Weyl semimetals with inhomogeneous b_μ

So far, all of the response properties that we have considered for the WSM have assumed b_μ was constant in space-time. This will not be the case in systems which have boundaries or interfaces across which b_μ will naturally change. In this section, we closely examine what the bulk action implies for the surface/interface action, and how the whole system remains gauge invariant. We recall that the response action is

$$S = -\frac{e^2}{2\pi h} \int \mathrm{d}^4x\, \epsilon^{\mu\nu\rho\sigma} b_\mu A_\nu \partial_\rho A_\sigma. \tag{4.23}$$

Now, when we take the functional derivative of S with respect to A_α to extract the current, we have to be careful about the behavior of b_μ

$$j^\alpha = \frac{e^2}{\pi h}\epsilon^{\alpha\mu\rho\sigma} b_\mu \partial_\rho A_\sigma + \frac{e^2}{2\pi h}\epsilon^{\alpha\mu\rho\sigma} A_\sigma \partial_\rho b_\mu. \tag{4.24}$$

This gives us the usual current we expect for the AHE and CME, along with a term which depends on derivatives of b_μ, but is not manifestly gauge invariant since it depends directly on A_μ. This signals the presence of an anomaly that will arise whenever b_μ changes.

The Callan-Harvey mechanism provides a straightforward way of understanding this result [10]. To be explicit, let us assume we have an interface in the x-direction, located at $x = x_0$, where b_z jumps from a finite value to zero. This is the case in the lattice models we studied in the previous section. Under a gauge transformation ($A_\mu \to A_\mu - \partial_\mu \lambda$) the action transforms as

$$\begin{aligned}
\delta_\lambda S &= -\frac{e^2}{2\pi h}\int \mathrm{d}^4x\, \epsilon^{\mu\nu\rho\sigma} b_\mu(-\partial_\nu\lambda)\partial_\rho A_\sigma \\
&= -\frac{e^2}{2\pi h}\int \mathrm{d}^4x\, \epsilon^{\mu\nu\rho\sigma} \partial_\nu b_\mu \partial_\rho A_\sigma \lambda \\
&= \frac{e^2}{2\pi h}\int \mathrm{d}^4x\, \epsilon^{zx\rho\sigma} b_z \delta(x-x_0)\partial_\rho A_\sigma \lambda \\
&= \frac{e^2 L_z b_z}{2\pi h}\int \mathrm{d}y dt\, \epsilon^{\rho\sigma}\partial_\rho A_\sigma \lambda \neq 0.
\end{aligned} \tag{4.25}$$

Thus, in order for the system to be gauge invariant there must be localized fermion modes where b_z jumps (except in the case when it jumps in the z-direction, since $\delta_\lambda S = 0$ in that case). In fact, for the simple WSM models we have considered, we know that there are such surface/interface states, and they are just straight-line Fermi-arcs that stretch between the Weyl nodes projected onto the surface/interface BZ. For a non-zero b_z, and a surface with normal vector $\hat{x}$ (just like the interface considered in the previous paragraph), the surface states have a chiral dispersion given by $E(k_y, k_z) = k_y$ at low-energy. These chiral modes give rise to the usual chiral anomaly. There is an independent chiral fermion for each value of k_z, but the surface states only exist in-between the Weyl nodes, i.e., only for $-b_z \leq k_z \leq b_z$. Each 1D chiral mode generates an anomalous contribution to the variation of the boundary/interface action under a gauge transformation [46, 10]

$$\delta_\lambda S_{bdry} = -\frac{e^2}{2h}\int dydt \epsilon^{\rho\sigma}\partial_\rho A_\sigma \lambda \tag{4.26}$$

where $\rho, \sigma = 0, y$. To calculate the total variation due to all of the modes we can convert the sum over the independent k_z modes to an integral which generates a factor of $\frac{L_z}{2\pi}2b_z$. We thus find

$$\delta_\lambda S^{(Tot)}_{bdry} = -\frac{e^2 L_z b_z}{2\pi h}\int dy dt \epsilon^{\rho\sigma}\partial_\rho A_\sigma \lambda \tag{4.27}$$

which exactly cancels the variation coming from the bulk action. Eq. 4.27 is called the consistent anomaly. The consistent anomaly leads to an anomalous Ward identity for current conservation on the edge

$$\partial_\mu j^\mu_{bdry} = -\frac{e^2 L_z b_z}{2\pi h}\epsilon^{\rho\sigma}\partial_\rho A_\sigma = -\frac{e^2 N_c}{2h}\epsilon^{\rho\sigma}\partial_\rho A_\sigma \tag{4.28}$$

where N_c is the total number of modes in the interface/boundary Fermi-arc.

Going back to the bulk current response in Eq. 4.24, we see that the current naturally splits into two terms: (i) $j^\alpha_{bulk} = \frac{e^2}{\pi h}\epsilon^{\alpha\mu\rho\sigma} b_\mu \partial_\rho A_\sigma$ and (ii) $\tilde{j}^\alpha_{bdry} = \frac{e^2}{2\pi h}\epsilon^{\alpha\mu\rho\sigma} A_\sigma \partial_\rho b_\mu$. For our interface configuration we find

$$\tilde{j}^\alpha_{bdry} = -\frac{e^2}{2\pi h}\epsilon^{\alpha z x \sigma} A_\sigma b_z \delta(x - x_0). \tag{4.29}$$

If we integrate this current density over x and z we can combine this current with the current from the consistent anomaly to arrive at the Ward identity for the covariant anomaly (the anomaly that contains all contributions to the boundary current)

$$\partial_\alpha (j^\alpha_{bdry} + \tilde{j}^\alpha_{bdry}) = -\frac{e^2 L_z b_z}{\pi h}\epsilon^{\alpha\sigma}\partial_\alpha A_\sigma. \tag{4.30}$$

This covariant anomaly precisely matches the bulk-current inflow from j^x_{bulk} into the boundary/interface. Note that although we have assumed a model which has simple Fermi-arcs, the chiral anomaly result is very robust and does not depend on the exact form of the surface state dispersion, or any other details, only that the states are chiral. Thus we expect it to hold in any generic model, even in the cases when the Fermi-arcs are not straight line segments, but are curved. This result clearly shows that while the bulk action would predict a gauge-variant response, it is compensated by the surface Fermi-arcs states. The same is true when we do not have a physical boundary, but a region in which b_μ varies in space-time. When b_μ varies there are two contributions to the boundary current, one arising from the bulk action itself, and the other from the consistent anomalous current required of the boundary states in order to preserve gauge invariance of the bulk and boundary.

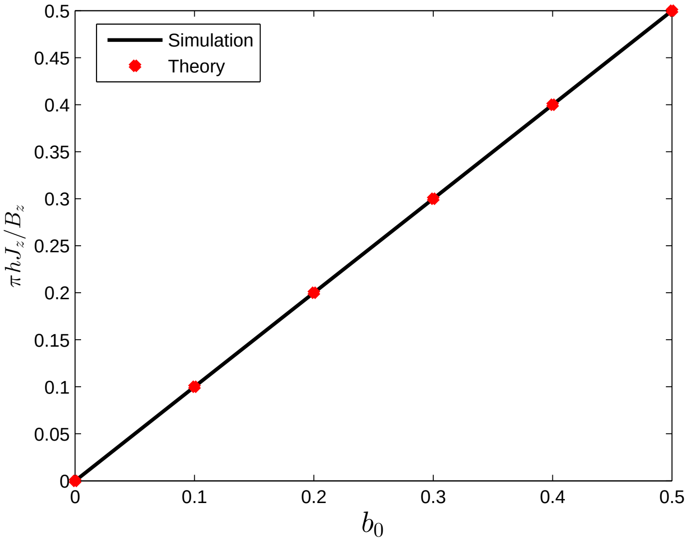

Figure 4.3: The current is plotted vs b_0 for the two band model of the Weyl semimetal. The current is linear and the slopes match almost exactly. This plot is generated for $L_x = 30$ and the flux per plaquette is $\phi = -2\pi/L_x$. We use $L_y = 30$, $L_z = 30$, and $b_z = \frac{\pi}{2}$ to generate this plot.

4.1.4 Numerical Results

After these analytic arguments let us explicitly test the predictions with numerical calculations. For illustration, we will probe two effects: (i) the CME, which we have tried analyzing using a mapping to the 1D model, and (ii) the charge density response in a system with an inhomogeneous $\vec{b}$. We do this in the context of the two band WSM lattice model

$$H = \gamma \sin k_z \mathbb{I} + \sin k_x \sigma^x + \sin k_y \sigma^y + (2 - m - \cos k_x - \cos k_y - \cos k_z)\sigma^z \tag{4.31}$$

where γ generates a nonzero b_0. It is important to note that to perform our numerical calculations we fill the states up to $E = 0$, i.e. all states with $E \leq 0$ are filled. To illustrate an example of the CME, in Fig. 4.3, we have plotted the current along the z direction as a function of b_0 in the presence of a uniform magnetic field, but no electric field. The predicted current density from the model, assuming a magnetic field in the z direction, is given by

$$j_z = -\frac{e b_0 B_z}{\pi h}. \tag{4.32}$$

The lattice calculation is shown in Fig. 4.3, and we find exactly this result. For this calculation the magnetic field is implemented using Peierls substitution. We use a Landau gauge to retain translation invariance in one of the directions in the xy plane, and the z direction is also translation invariant. The magnetic field is

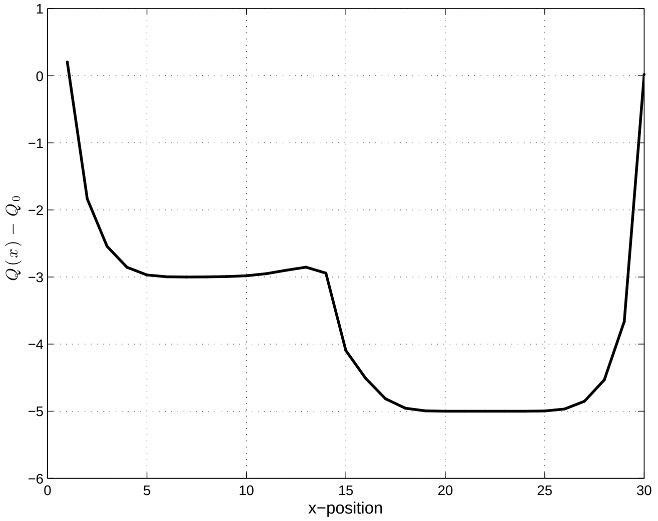

Figure 4.4: The charge density is plotted vs. position in the x-direction with open boundary conditions. The system is comprised of a Weyl semimetal with $b_{z,L} = \pi/5$ for $0 < x < L_x/2$ and $b_{z,R} = \pi/3$ for $L_x/2 < x < L_x$. The total number of sites in the x-direction was $L_x = 30$ with magnetic flux per unit cell in the $x - y$ plane $\phi = -2\pi/30$. Also, $L_z = 30$ and $L_y = 30$. The bulk charge density is given by $N_x = -L_z L_y b_z B_z/4\pi^2 = -3, -5$ as is predicted by the action.

restricted to have rational flux per unit cell for the spectrum to remain periodic in momentum space.

Another simple effect to test is the density response at an interface where $\vec{b}$ changes. With $B_z \neq 0$, we should have

$$\rho = \frac{e b_z B_z}{\pi h}. \tag{4.33}$$

So, if we vary b_z in the x-direction (with open boundary conditions the xz surfaces host nontrivial surface states) one would expect a varying charge density. In fact, one can see this is exactly reproduced in numerics and the resultant charge density is plotted in Fig. 4.4. The bulk charge follows what is predicted by the action in the continuum calculation.

4.2 Electromagnetic response of a 3D Dirac semi-metal

There has been a lot of recent work predicting and measuring materials candidates for 3D Dirac semi-metals [110, 60, 68, 101, 100], however we are interested in the so-called Z_2 non-trivial 3D Dirac semi-metals [60, 107] where the Dirac nodes appear in pairs, and can exist at generic points in the Brillouin zone, as recently measured in Na_3Bi. In this section, we will discuss an interesting electromagnetic probe of this type of 3D DSM, and show that it can be derived from the response properties of the 2D time-reversal invariant quantum spin Hall insulator [54, 7, 55, 59, 74, 75].

In fact, analogous to all of our previous constructions, we can think of the 3D DSM as a layered 2D topological insulator, and in this case it is formed from coupled layers of the QSH system. The layer construction has aided the discussion and analysis of the other topological semi-metals, and we will see that it is very helpful in this case as well. Thus, we begin this section by first examining the response of the Quantum Spin Hall(QSH) insulator itself, since the results can immediately be generalized to stacks of QSH insulators, and hence the 3D DSM. After reviewing the response of the QSH insulator, we will discuses the analogous properties of the DSM, and numerically validate our analytical calculations.

The QSH system has an unusual electromagnetic response given by [74, 75]

$$S[A] = \frac{e}{2\pi}\int d^3x\,\epsilon^{\mu\nu\sigma}A_\mu\partial_\nu\Omega_\sigma \tag{4.34}$$

where Ω_μ is a gauge field which encodes configurations of inhomogeneous adiabatic perturbations. We will clearly define what this means in the following section. Essentially, the configurations of Ω_μ are related to possible mass-inducing perturbations of a Dirac-type Hamiltonian. As a consequence of this response term, a magnetic film deposited at the edge of the QSH insulator can generate a localized charge density or adiabatic current if the magnetization is space or time dependent respectively [74, 75]. The edge of the QSH insulator is itself a robust 1D massless Dirac fermion if we preserve time-reversal symmetry. A magnetization on the edge will open a gap, and through the well-known Jackiw-Rebbi mechanism [51], a spatial domain-wall in the magnetization will trap a low-energy mid-gap mode. This mode signals a bound charge of $Q_b = \pm e/2$. Additionally, ff the magnetization on one side of the domain wall begins to rotate as a function of time, a quantized adiabatically pumped charge current can flow along the edge through the magnetic junction. [75] showed that both of these phenomena could be derived from Eq. 4.34. This is the electromagnetic signature of the QSH insulator, and is closely tied to the response of the 3D DSM.

Now we can construct a stack of QSH insulators. If the layers are weakly coupled then we will get the conventional WTI state [31, 65, 81]. If we increase the strength of the inter-layer coupling so that we close the bulk gap we will generate the 3D DSM phase. Just as with the WSM, the edge states of the QSH layers forming the DSM will survive in a certain region of momentum space and will connect the various 3D Dirac nodes with Fermi-surface arcs. We can easily extrapolate the response action of the QSH insulator to the 3D DSM to find

$$S[A] = \frac{e}{2\pi^2}\int d^4x\,\epsilon^{\mu\nu\rho\sigma}b_\mu A_\nu\partial_\rho\Omega_\sigma. \tag{4.35}$$

We will discuss the consequences of this action below, but first we will more carefully recount the analysis for the 2D QSH insulator since its formulation is not as widely known, and we wish for thisthesis to be relatively self-contained.

4.2.1 Response from the Second Chern number

The discussion in this Section closely follows the arguments in [75], although we will only reproduce the necessary ingredients for our discussion of the 3D DSM, and leave out some of the details which can be found in the aforementioned reference. In general the response of the QSH insulator is derived from the second Chern number C_2, which is a four dimensional topological invariant. Since the QSH exists in 2D, the Bloch Hamiltonian is only parameterized by two numbers k_x, k_y, which is not enough to generate a non-zero C_2. Thus, to probe the electromagnetic response properties of the QSH state, we need to couple the system to two additional parameters $\theta(\mathbf{x}, t), \phi(\mathbf{x}, t)$, which represent adiabatic parameters which vary slowly in space and time so that momentum space is still approximately well-defined. The gauge field Ω_μ introduced above is a function of space and time, but only through its dependence on θ and ϕ.

To be explicit, consider the QSH Hamiltonian given by

$$H_{QSH}(\mathbf{k}, \hat{n}) = \sin k_x \Gamma^1 + \sin k_y \Gamma^2 + (\cos k_x + \cos k_y - 2)\Gamma^0 + m \sum_{a=0,3,4} \hat{n}_a \Gamma^a \tag{4.36}$$

in which $m > 0$, Γ^a are the 4×4 Dirac matrices, and $\hat{n} = (n_3, n_4, n_0)$ is a 3D unit vector. The $\Gamma^{1,2,3,4}$ are all odd under inversion and time-reversal ($T^2 = -1$), while Γ^0 is even under both. The unperturbed QSH insulator will have $n_3 = n_4 = 0$ but $n_0 \neq 0$. If we let $\hat{n}$ vary slowly as a function of space-time we can parameterize it using two adiabatic space-time dependent parameters via $\hat{n}(\mathbf{x}, t) = (\sin\theta(\mathbf{x}, t)\cos\phi(\mathbf{x}, t), \sin\theta(\mathbf{x}, t)\sin\phi(\mathbf{x}, t), \cos\theta(\mathbf{x}, t))$. The results of [75] show that in the low-energy continuum limit of H_{QSH} expanded around the Γ-point, the gauge curvature of Ω is directly related to the skyrmion density of the unit vector $\hat{n}$ as

$$\partial_\mu \Omega_\nu - \partial_\nu \Omega_\mu = \frac{1}{2} \hat{n} \cdot \partial_\mu \hat{n} \times \partial_\nu \hat{n}. \tag{4.37}$$

Using Eq. 4.34 we can write down the current in terms of this skyrmion density as

$$j^\mu = \frac{e}{8\pi} \epsilon^{\mu\nu\rho} \hat{n} \cdot \partial_\nu \hat{n} \times \partial_\rho \hat{n}. \tag{4.38}$$

Now let us consider an important example case. Assume that we have a QSH sheet with a static edge parallel to the y-direction and a pair of static magnetic films next to each other on the edge. If the magnetizations of the two films are opposite, this will produce a domain wall on the edge with a magnetization that varies as a function of y. In that case we find the parameterization $\theta = \theta(x)$ and $\phi = \phi(y)$. At the location of a θ domain wall between $\theta = 0$ and $\theta = \pi$ there will be an edge. At the location of a ϕ domain wall between $\phi = 0$ and $\phi = \pi$ there will be a magnetic domain wall. In this geometry we find

$$\begin{aligned} j^0 &= \frac{e}{4\pi}\hat{n}\cdot\partial_x\hat{n}\times\partial_y\hat{n} \\ &= \frac{e}{4\pi}\sin\theta\times\frac{d\theta}{dx}\frac{d\phi}{dy}. \end{aligned} \tag{4.39}$$

Due to the dependence on the derivatives of θ and ϕ, the charge density is localized wherever $\theta(x)$ and $\phi(y)$ are *both* changing. If we have a sharp magnetic domain wall on a sharp edge, then all of the charge density will be localized at the magnetic domain-wall, i.e., where the θ and ϕ domain walls intersect. The total charge in the neighborhood of this intersection can be calculated by integrating over x, y. The integration is easily performed since the integrand is a total derivative in x and y. We just get the integral over the solid angle swept out by θ and ϕ, which for this configuration is half the sphere, i.e. $\pm 2\pi$. This yields a bound charge $Q_b = \pm 2\pi\frac{e}{4\pi} = \pm\frac{e}{2}$.

We can similarly find an adiabatic pumping current by having a static edge ($\theta = \theta(x)$), and sweeping the relative magnetization between the two magnetic films on the edge as a function of time ($\phi = \phi(t)$) [74]. Everything carries through in exactly same way and we find

$$j^y = \frac{e}{4\pi}\sin\theta\times\frac{d\theta}{dx}\frac{d\phi}{dt}. \tag{4.40}$$

We can again integrate over x, t to get the total charge transported as the relative magnetization angle sweeps through a full cycle to find, as $\phi : 0 \to 2\pi$, we have $\Delta Q = e$. This current is localized wherever θ has a sharp change in its value, i.e. on the edge.

We can understand the physics underlying the QSH response from the microscopic behavior of the edge states. In the low energy limit near the Dirac point, we can write down the Hamiltonian for one of the edges of the QSH system (say an edge at $x = 0$) as

$$H_{edge}(k) = k\sigma^z \tag{4.41}$$

where k is the momentum of the coordinate along the edge, and we have set the edge velocity to unity. Coupling the magnetic layer to the edge will induce a gap from the proximity exchange (Zeeman) coupling.

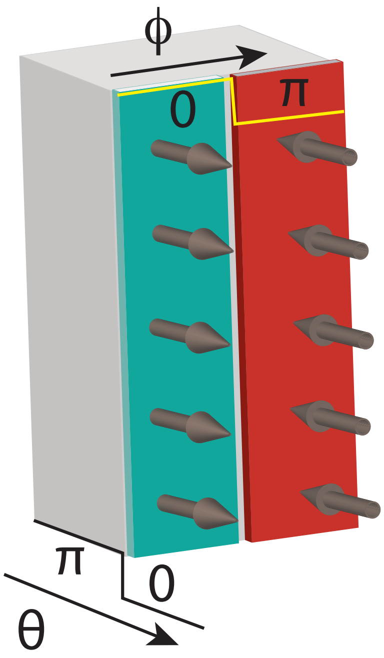

Figure 4.5: Setup to generate an electromagnetic response in a 3D Dirac semi-metal. To get a non-zero response there must be two adiabatic parameters θ and ϕ. The parameter θ represents an interpolation between a 3D Dirac semi-metal with, for example, $b_z \neq 0$ to a trivial insulator with $b_z = 0$. The parameter ϕ represents a magnetization domain-wall on the xz surface plane. There will be a branch of low-energy fermion modes trapped on the domain wall which can bind charge or can carry current if $b_0 \neq 0$.

If the magnetization lies in the plane, then the effective Hamiltonian becomes

$$H_{edge} + H' = k\sigma^z + m_x\sigma^x + m_y\sigma^y. \tag{4.42}$$

Let us choose a configuration with $m_x = 0$ and $m_y = m(y)$ is a shifted step-function which goes from a negative value to a positive value at $y = 0$. It is well-known [51] that this Hamiltonian has an exponentially localized zero mode at the domain wall of $m(y)$ given by

$$\psi = \mathrm{e}^{-\int_0^y m(y')dy'} \frac{1}{\sqrt{2}} \begin{pmatrix} 1 \\ 1 \end{pmatrix} \tag{4.43}$$

when the mass jumps from negative to positive as y increases. On a periodic edge, $m(y)$ will have to have two domain walls to maintain the proper boundary conditions, and the edge will have two zero modes, one at each domain wall. These localized zero modes carry a half charge each. This is the same result found from Eq. 4.39. To complete the story in the language above, the QSH system itself has a non-trivial value of the Z_2 invariant $\theta = \pi$ [55, 75]. Thus, its boundary gives a natural place where θ has a jump from π to

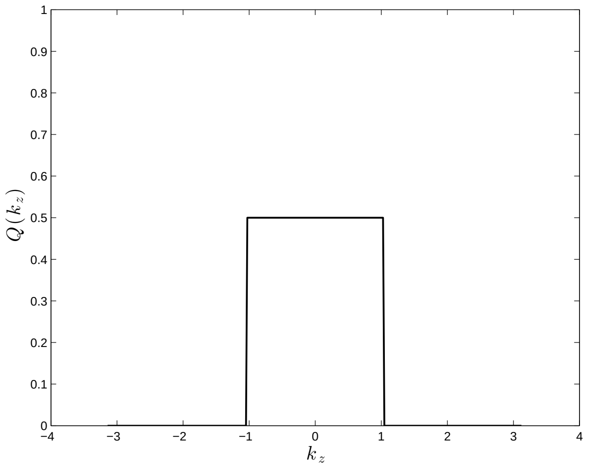

Figure 4.6: The localized charge on a magnetic domain wall on the surface of a 3D DSM resolved vs. k_z, i.e., the direction in which the Dirac nodes are separated in momentum space. We note that there is a half charge bound at the domain wall only for each state satisfying $|k_z| < \cos^{-1} m$. In the plot, we have used $m = 0.5$ which means $b_z = \frac{\pi}{3}$.

0. The spatial dependence of the ϕ parameter is due to the magnetization induced mass.

We can also generate an adiabatically pumped current. To see this we can add a slow, time-dependent perturbation to the edge Hamiltonian in the following way

$$H_{edge}(k) = k\sigma^z + m \sin\phi(t)\,\sigma^y + m\cos\phi(t)\,\sigma^x \tag{4.44}$$

where $\phi(t) = 2\pi t/T$. The mass terms are periodic in time with a period of T. From the original work by Thouless [92] we know that as $\phi \to \phi + 2\pi$ an integer amount of charge will be pumped, in this case just a single electron per cycle. This is the same current which is reported in Eq. 4.40.

4.2.2 Response of the Dirac semi-metal

Now that we have finished the discussion for a single QSH layer we are ready to move on to the 3D DSM. We can start from the QSH Hamiltonian, but we need to modify it to include tunneling in the z-direction due to the coupled layers. The following model can be used

$$H_{DSM3}(\mathbf{k}, \hat{n}) = \sin k_x\Gamma^1 + \sin k_y\Gamma^2 + (\cos k_x + \cos k_y + t_z \cos k_z - 3)\Gamma^0 + m \sum_{a=0,3,4} \hat{n}_a\Gamma^a. \tag{4.45}$$

If the 2D layers are in the QSH phase, then when the tunneling term t_z is weak, the system will be in a WTI phase. As it becomes stronger eventually the gap will close at one of the time-reversal invariant

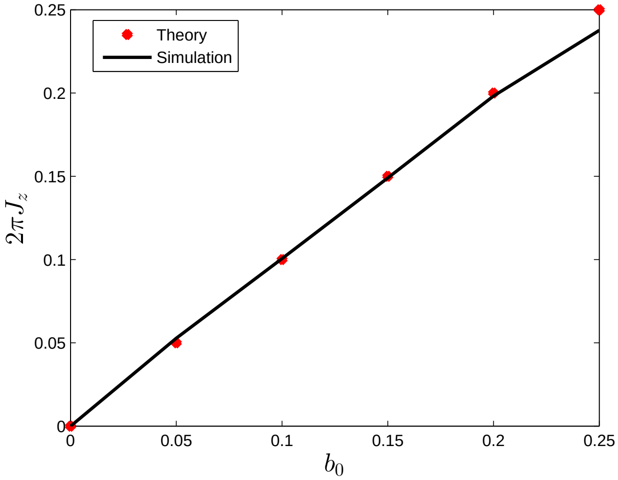

Figure 4.7: The total current localized at the magnetic domain wall is plotted vs b_0 for the 3D DSM. The expected value of the total current localized on the domain wall is $\frac{eb_0}{2\pi}$. The system size is a cube of $L = 30$ lattice sites in every direction with $b_z = \frac{\pi}{2}$. We used open boundary conditions in both the x, y directions and periodic boundary conditions in the z direction. The red dots are the theoretical result and the black line is the numerical result. The deviation arises due to the importance of lattice effects at larger values of b_0.

momenta along the k_z axis and generate a pair of Dirac nodes, hence entering the 3D DSM phase. In a recent work [107] this has been called a Z_2 non-trivial Dirac semi-metal. From the previous patterns of the electromagnetic response, and the known response of the QSH insulator, we can immediately write the response action

$$S_{3D} = \frac{e}{2\pi^2} \int d^3x\, dt\, \epsilon^{\mu\nu\rho\sigma} b_\mu A_\nu \partial_\rho \Omega_\tau \qquad (4.46)$$

for the 3D DSM, where $2b_\mu$ is the energy-momentum separation of the Dirac nodes. We now have a natural family of 2D Bloch Hamiltonians parameterized by k_z $H_{k_z}(k_x, k_y)$. Each of the 2D Hamiltonians, for k_z not at a Dirac node, represents at 2D time-reversal invariant insulator and is classified by the same Z_2 invariant as the QSH insulator. As k_z passes through a Dirac node the Z_2 invariant jumps from trivial to non-trivial, or vice-versa. Thus, one of the regions of k_z between the Dirac nodes will harbor non-trivial topological QSH insulators and thus generate edge states. For each k_z in the topological range we will have a contribution of one layer of QSH to the total electromagnetic response. This is the meaning of Eq. 4.46. [107] has shown that this type of semi-metal requires a uniaxial rotation symmetry to locally stabilize the Dirac nodes. Our model has such a symmetry (C_4 rotation around the z-axis), and thus represents a stable Z_2 non-trivial DSM. We will leave a more general symmetry analysis of the electromagnetic response to future work.

Let us look at some examples of the physical phenomena associated to Eq. 4.46. Just like the case of a single QSH layer, to get a non-trivial response we need to apply a magnetic film to a boundary with non-trivial surface states. As shown in Fig. 4.5, for Dirac nodes separated in k_z we can coat the xz boundary plane with a magnetic layer. A translationally invariant magnetic domain wall parallel to the z-axis in the magnetic layer (see Fig. 4.5) will create a line of low-energy modes which do not disperse with k_z. Thus for each k_z that contributes a boundary mode we will bind a half charge. We numerically calculated the bound charge at a domain wall as a function of k_z and the result is shown in Fig. 4.6. In this figure we see exactly $e/2$ charge contributed for each value of k_z between the Dirac nodes. For this calculation we used the mass parameter $m = 0.5$, and varied ϕ and θ as functions of y and x respectively according to Eq. 4.45.

The bound charge response will also occur in a time-reversal invariant WTI system, however a new phenomenon which is not available in the WTI is the generation of a current along the domain wall in the direction along which the Dirac nodes are separated. This can occur if the Dirac nodes are not at the same energy, and it is the 3D DSM analog of the chiral magnetic effect in Weyl semi-metals.

We can generate an energy difference, i.e. $2b_0$, in our Hamiltonian by adding the term $\gamma \sin k_z \mathbb{I}$ to the Hamiltonian in Eq. 4.45. When we have a magnetic domain wall and a non-zero b_0, the localized domain wall states will disperse with energy $E_{dw} = 2\gamma \sin k_z$ and this leads to a non-zero current. We calculated this current numerically as shown in Fig. 4.7. With a $b_0 \neq 0$, the current is being generated due to the dispersion of the localized edge modes which now have to traverse between the two Dirac nodes in a continuous fashion. The total current localized on the domain wall is given by

$$\begin{aligned} J_z &= \frac{eb_0}{2\pi^2} \int d^2x \, (\partial_x \Omega_y - \partial_y \Omega_x) \\ &= \frac{eb_0}{2\pi^2} \int d\theta d\phi \, \frac{1}{2} \sin\theta = \frac{eb_0}{2\pi} \end{aligned} \tag{4.47}$$

which matches the numerical calculation well until b_0 is large enough for lattice effects to become important. This mechanism for current generation is reminiscent of the orbital magnetization generation due to currents produced by dispersing edge states in the 2D Dirac semi-metal.

Chapter 5

Line node semimetal in $3+1$ dimensions

The EM response of *point*-node TSMs is generally characterized by an intrinsic 1-form $b = (b_0, b_i)$ which is related to the locations of the nodes in momentum and energy space [114, 78]. The actual dependence of the EM response on b depends on the type of point-node semimetal, and can generate a wide variety of effects in 2D and 3D TSMs. We expect the EM response of a line-node topological semimetal (LTSM) to be characterized by an analogous 2-form $B_{\mu\nu}$, which is an *intrinsic* property of the electronic structure of LTSMs that is determined by the geometry of the nodal submanifolds, and is the analog of a secondary weak invariant, though for a gapless phase. In this chapter, we show that the effective quasi-topological electromagnetic response action for LTSMs is given by

$$S[A, \mathcal{B}] = \frac{e}{16\pi^2} \int d^4x \, \epsilon^{\mu\nu\rho\sigma} \mathcal{B}_{\mu\nu} F_{\rho\sigma}. \tag{5.1}$$

Crucially, we show that $\mathcal{B}_{\mu\nu}$ can be determined from the geometry of the nodal Fermi surfaces in energy-momentum space. From the form of Eq. 5.1 we see that the components of $\mathcal{B}_{\mu\nu}$ can be related to the magnetization and polarization of the LTSM via $e\mathcal{B}_{0i} = 4\pi^2 M_i$ and $e\mathcal{B}_{ij} = 4\pi^2 \epsilon_{ijk} P^k$ for $i = x, y, z$. We note that $\mathcal{B}_{\mu\nu}$ also includes components where μ, ν are in the time direction, which can be generated in a gapless system, but are not available for a time-independent gapped system. However, such components would appear in cyclically-driven gapped systems where they would take values dependent on the driving frequency.

5.1 Motivation using two band model

To aid our discussion it will be helpful to consider an explicit model. Let us consider the 3D Bloch Hamiltonian

$$H_3(k) = \sin k_x \sigma^y + (1 + \beta + \gamma - m - \cos k_x - \beta \cos k_y - \gamma \cos k_z)\sigma^z, \tag{5.2}$$

which has inversion $\mathcal{I} = \sigma^z$ and time reversal $\mathcal{T} = \sigma^z K$ symmetries, where σ^a represent two (non-spin) degrees of freedom, and the lattice constant $a = 1$. When $\beta = \gamma = 0$, and $|m| \neq 1$, this model reduces to decoupled 1D insulators aligned parallel to the x-direction. Since each 1D wire is inversion symmetric, their polarizations will be quantized (and all equal). In the topological phase ($|m| < 1$), the polarization of a single wire will be $P_x(k_y, k_z) = \frac{e}{2\pi}\int \mathrm{Tr}[\mathcal{A}_x(\vec{k})]dk_x = e/2 \bmod e$ [111, 56], where $\mathcal{A}_i(\vec{k})$ is the adiabatic connection matrix $\mathcal{A}_i^{ab}(\vec{k}) = -i\langle u_{a,k}|\frac{d}{dk_i}|u_{b,k}\rangle$, where a, b run over the occupied bands. If each insulator was instead in a trivial state ($|m| > 1$), we would have $P_x(k_y, k_z) = 0 \bmod e$.

In addition to the bulk topological properties, the 1D TIs have degenerate mid-gap modes localized at opposite ends of the system, the filling of which determines the bound surface charge. To unambiguously determine the sign of the bulk polarization, and hence the sign of the surface charge, one must break the degeneracy by adding an infinitesimal (inversion) symmetry breaking mass, e.g., $m_{\mathcal{I}}\sigma^y$ and take the limit as $m_{\mathcal{I}} \to 0$. Hence, for $\beta = \gamma = 0, |m| < 1$ this model represents a secondary weak TI phase protected by inversion symmetry, and the EM response is given by Eq. 5.1, but for the special case when $\mathcal{B}_{yz} = \mathrm{sgn}\, m_{\mathcal{I}}(\frac{1}{2}\mathbf{G}_y \wedge \mathbf{G}_z) \implies P_x = \mathrm{sgn}\, m_{\mathcal{I}} \frac{e}{2a_y a_z}$.

Now, we can find a simple example of a gapless phase if $\gamma = 0$ and β is increased until we effectively create layers of 2D Dirac semimetals. This gapless system will have two gapless lines in the Brillouin zone (BZ) at $k_y^{\pm} = \pm\cos^{-1}\frac{\beta - m}{\beta}$ for each value of k_z. These FLs are locally stable in the BZ as long as the composite $\mathcal{TI}$-symmetry is preserved. The response is given by Eq. 5.1 with $\mathcal{B} = \mathrm{sgn}\, m_{\mathcal{I}}(b_y \wedge \mathbf{G}_z)$ where $2b_y = k_y^+ - k_y^-$, and is a special case of our general results. We could also reverse the role of β and γ and find a phase with $\mathcal{B} = \mathrm{sgn}\, m_{\mathcal{I}}(\mathbf{G}_y \wedge b_z)$ instead.

Now let us consider a more generic/isotropic case by increasing the tunneling strengths γ, β large enough so that the insulating gap closes and a single closed FL inside the BZ forms. Performing an expansion around the origin, gaplessness will imply the constraints $k_x = 0, \pi$ and $\beta k_y^2 + \gamma k_z^2 = 2m$, i.e., the equation for an ellipse. Assuming that $\beta, \gamma > 0$ to be explicit, this constraint only has a solution when $m > 0$. Now to be concrete, we expand the Hamiltonian by assuming $\beta = \gamma = 2m = 2$ so that there is a only a single FL circle located in the $k_x = 0$ plane, and none at $k_x = \pi$. It is convenient to switch to cylindrical coordinates: $(k_x, k_y, k_z) \to (k_x, \kappa, \theta)$ where θ winds around the FL, and κ represents the (signed) radial distance *away* from the FL in the $k_y k_z$-plane. Using this definition, $(k_x = 0, \kappa = 0, \theta)$ lies on the FL and we find the Hamiltonian near the FL is

$$H_{FL}(k) \approx \delta k_x \sigma^y + (1/2(\delta k_x)^2 + 2\delta\kappa)\sigma^z \approx \delta k_x \sigma^x + m(\delta\kappa)\sigma^z \tag{5.3}$$

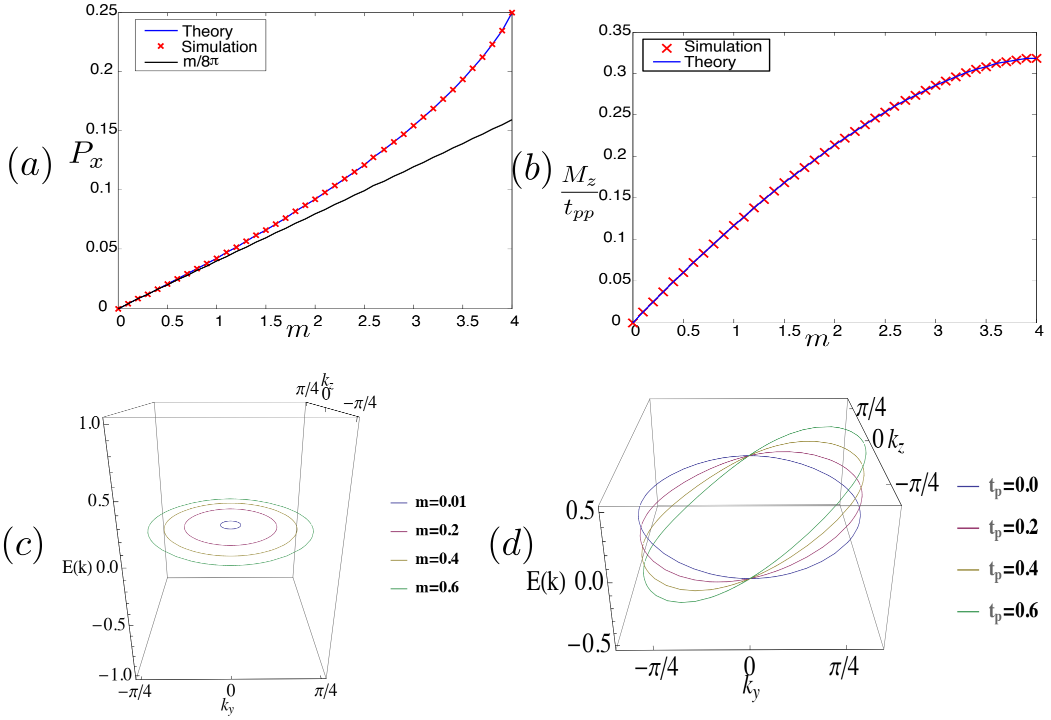

Figure 5.1: (a) The polarization for the model in Eq. 5.2 is plotted vs. the parameter m in the model with $\beta = \gamma = 2$. (b) The magnetization for the model in Eq. 5.2 with the extra term $t_{pp} \sin k_y \mathbb{I}$ is plotted vs various values of m for $\beta = \gamma = 2$. (c) The location of the line node is plotted in the $E - k_y - k_z$ space with $k_x = 0$ for $t_{pp} = 0$ and various values of m with $\beta = \gamma = 2$. The polarization is proportional to the area enclosed by the FL. (d) The location of the line node is plotted in the $E - k_y - k_z$ space with $k_x = 0$ for $m = 1$ and various values of t_{pp} with $\beta = \gamma = 2$. The magnetization is proportional to integral of the energy around the FL in momentum space.

where the mass function $m(\delta\kappa) \equiv 2\delta\kappa$, and nothing depends on θ. Thus, near the Fermi surface we find a family of 1D Dirac Hamiltonians along the x-direction with masses depending on the radius in k-space away from the Fermi-surface ($\delta\kappa$) in the $k_y k_z$-plane which can be positive or negative. This expansion shows that at each (k_y, k_z) we have the Hamiltonian of a massive 1D Dirac model, and the sign of the mass (and thus topological phase) changes as a function of (k_y, k_z) as one passes through the FL. This validates our perspective of a LTSM as a collection of 1D wires where the FL represents the topological phase transition between contiguous regions of wires in the BZ. We expect the low-energy Hamiltonian near any non-degenerate FL to take a similar form, regardless of the microscopic lattice model from which it emerges. One immediate conclusion we can draw from this analysis is that this model will have a surface charge from the localized topological modes at the ends of the wires in the topological region in momentum space, i.e., the region either inside or outside the FL.

5.2 General arguments for polarization/magnetization response

Now, let us step away from our example model and generically determine the polarization of a LTSM in some fixed direction $\hat{n}$. It is useful to treat our 3D Bloch Hamiltonian as a family of 1D Bloch Hamiltonians $H_{\vec{k}_\perp}(k_\parallel)$ parameterized by $\vec{k}_\perp, k_\parallel$, which are the components of the momentum perpendicular and parallel to $\hat{n}$. Generically, the family $H_{\vec{k}_\perp}(k_\parallel)$ is a set of 1D gapped Bloch Hamiltonians except when the point $(k_\parallel, \vec{k}_\perp)$ lies on one of the FLs (which only occupy a set of measure zero in the 3D BZ). Note that while the FLs in our model are planar, our results below apply to non-planar cases as well. To calculate the charge polarization we first need to first calculate the quantity [56]

$$\Theta_\parallel(\vec{k}_\perp) = \frac{e}{2\pi} \int dk_\parallel \mathrm{Tr}\left[\mathcal{A}_\parallel(k_\parallel, \vec{k}_\perp)\right] \tag{5.4}$$

where $\mathcal{A}_\parallel$ is the component of the Berry connection along $\hat{n}$. Let us first consider a special case where we evaluate $\Theta(\vec{k}_\perp)$ at $\vec{k}_\perp = \vec{\Lambda}_a$, where $\vec{\Lambda}_a$ is any inversion-invariant momentum in the $\vec{k}_\perp$ plane, i.e., $\vec{\Lambda}_a = -\vec{\Lambda}_a \mod \vec{G}$. Then $\Theta(\vec{\Lambda_a})$ is quantized to be 0 or $e/2 \mod e$, if $H_{\vec{\Lambda}_a}(k_\parallel)$ is gapped, since this 1D Bloch Hamiltonian has inversion symmetry. We then consider a deviation away from $\vec{k}_\perp = \Lambda_a$ which is still in the plane normal to $\hat{n}$, and such that the Hamiltonian $H_{\vec{\Lambda}_a+\delta\vec{k}_\perp}(k_\parallel)$ is gapped. However, this 1D Bloch Hamiltonian does not have to be inversion invariant, and thus it is not immediately obvious how to evaluate $\Theta_\parallel$. However, we can use the following general argument to simplify the calculation. Let us evaluate the difference in the 1D polarizations

$$\Delta\Theta_\parallel = \Theta_\parallel(\vec{\Lambda}_a + \delta\vec{k}_\perp) - \Theta_\parallel(\vec{\Lambda}_a) = \frac{e}{2\pi}\int_S \mathrm{Tr}\left[F\right] \tag{5.5}$$

where the last expression is a surface integral of the Berry curvature 2-form F over the region S bounded by the two closed circles located at $\vec{\Lambda}_a$ and $\vec{\Lambda}_a + \delta\vec{k}_\perp$, and spanned by $k_\parallel$ through the cycle of the BZ in the $\hat{n}$ direction. Crucially, since our system has $\mathcal{TI}$ symmetry, the only sources of Berry curvature are the π-flux lines carried by the FLs. Thus, generically $\Delta\Theta_\parallel$ itself is quantized to be either 0 or $\frac{e}{2} \mod e$ depending on the parity of the number of Dirac line-nodes enclosed in the surface S. The quantization of $\Delta\Theta_\parallel$ is completely general and does not rely on starting at an inversion-invariant momentum, it only relies on the existence of $\mathcal{TI}$ symmetry. The ability to start at an inversion-invariant momentum just informs us that the global constant needed to determine the full $\Theta_\parallel(\vec{k}_\perp)$ from the knowledge of only the $\Delta\Theta_\parallel(\vec{k}_\perp)$ is either 0 or $\frac{e}{2}$; data which is ultimately encoded in the secondary weak invariant ν_{ij} of the occupied bands.

For a system with a single FL we see that $\mathcal{B}_{ij}$, and hence, the overall charge polarization is simply proportional to the projected area of the FL in the $\hat{n}$ boundary BZ, i.e.,

$$e\mathcal{B}_{ij} \equiv 4\pi^2 \epsilon^{\hat{n}ij} P_{\hat{n}} = \int_{\perp BZ} d\vec{k}_\perp \Theta_\parallel(\vec{k}_\perp) = (-1)^{\nu_{ij}} \frac{e}{2} \Xi\, \Omega_{ij} \tag{5.6}$$

where Ω_{ij} is the area of the FL projected onto the ij-plane of the boundary BZ, $\Xi = \chi(\operatorname{sgn} m_{\mathcal{I}})$, $\chi = \pm 1$ corresponds to the FL helicity, i.e., the clockwise/counterclockwise flow of the Berry flux along the FL with respect to the normal $\hat{n}$, and ν_{ij} is the secondary weak invariant defined as the holonomy of the Berry gauge field of the occupied bands along the line $k_i = k_j = \pi$. This is a bulk calculation for the polarization, and only holds up to the addition of a quantum of polarization [56]. Also, changing the secondary weak invariant ν_{ij}, can change the polarization by a quantum, and/or a sign, since it can switch the projected area to its complement in the surface BZ. For a single FL this effect is already taken into account in Eq. 5.6. However, for more than one FL, the bulk calculation will result in the sum of the projected areas of all the FLs modulo regions where an even number of FLs have overlapping projections. As shown in Appendix B.1, when FLs have overlapping projected areas, the connection between the bulk result and the surface charge requires some knowledge of the filling of the boundary states [20, 78].

One corollary of these general arguments is that, while it is not forbidden to have just a single closed FL in systems with $\mathcal{TI}$ symmetry, it is forbidden to have only one FL (or an odd number) which traverses a non-trivial cycle of the BZ and meets itself. We can see this because calculating any component of the polarization would indicate that the polarization must jump on either side of the FL, however this is not compatible with the periodicity of the BZ, and thus must be forbidden. This is a 3D line-node generalization of the fermion doubling theorem for Dirac nodes in 2D with $\mathcal{TI}$ symmetry.

To illustrate these results with our example model we calculate the polarization numerically in Fig. 5.1a where P_x of $H_3(k)$ is plotted vs. m with the corresponding geometry of the FL shown in Fig. 5.1c. We choose $\beta, \gamma = 2$ so that there is a single FL in the $k_x = 0$ plane and centered around the origin of the BZ. P_x should be proportional to the area enclosed by the FL given by $\cos k_y + \cos k_z = 2 - m/2$. For small values of m, the FL is approximately a circle of radius $\sqrt{m}$ and $P_x \approx \operatorname{sgn} m_{\mathcal{I}} \frac{m}{8\pi}$. This approximation works well when m is small, but underestimates P_x as m is increased. At $m = 4$, the FL given by $\cos k_y + \cos k_z = 0$ will enclose half the area of the BZ. The polarization has the symmetry $P_x(m) = \frac{e}{2} - P_x(8 - m)$ since for $m > 4$, the FL is just centered around $(k_y, k_z) = (\pi, \pi)$ on the boundary BZ instead of $(0, 0)$. Hence, we only show $0 \leq m \leq 4$ in Fig. 5.1a.

Now let us move on to studying the contributions of $\mathcal{B}_{0i}$ to the EM response. Similar to the 2D Dirac TSMs, which have a non-vanishing orbital magnetization when there is an energy difference between the Dirac nodes, LTSMs can also have a magnetization that depends on how the band touching lines are embedded in energy/momentum space. To produce this effect in our model, we need to change the energy along the nodal submanifold while preserving $\mathcal{TI}$, and we can do this, e.g., by adding an extra kinetic energy term $\epsilon(\vec{k})\mathbb{I}$ to $H_3(k)$. However, before calculating the result for our explicit model we will evaluate the magnetization in a generic system with $\mathcal{TI}$ symmetry.

Following [85, 13], the orbital magnetization is given by

$$M^a = \frac{e\epsilon^{abc}}{2\hbar}\int \frac{d^dk}{(2\pi)^d}\sum_{\alpha=1}^{M}\mathrm{Im}\,\langle\partial_b\alpha|H(k)+\epsilon_\alpha(k)|\partial_c\alpha\rangle \tag{5.7}$$

where we have absorbed the dependence on the chemical potential μ into $H(k)$ and $\epsilon_\alpha(k)$, assumed M occupied bands, and a total of N bands with $M \leq N$. $\epsilon_\alpha(k)$ is the energy of the α-th band, and $|\alpha\rangle$ is shorthand notation for the Bloch state $|u_{\alpha,\mathbf{k}}\rangle$. This sum can be simplified as follows. First, consider the terms which depend on the band energies $\epsilon_\alpha(k)$ and rewrite them as

$$\sum_{\alpha=1}^{M}\mathrm{Im}\,\epsilon_\alpha(k)\langle\partial_b\alpha|\partial_c\alpha\rangle = \sum_{\alpha=1}^{M}\Big[\mathrm{Im}\,\epsilon_\alpha(k)\langle\partial_b\alpha|P_E(k)|\partial_c\alpha\rangle + \mathrm{Im}\,\epsilon_\alpha(k)\langle\partial_b\alpha|P_G(k)|\partial_c\alpha\rangle\Big],$$

where $P_E(k)$ and $P_G(k)$ are the projectors onto the unoccupied and occupied bands respectively at each value of k, and they satisfy $P_G(k)+P_E(k)=\mathbb{I}_{N\times N}$. Then, we see that the first term is related to the $U(M)$ Berry curvature of the occupied bands since $\epsilon_\alpha(k)$ is real-valued and [75]

$$\mathcal{F}^{\alpha\alpha}_{bc}(k) = \mathrm{Im}\left[\langle\partial_b\alpha|P_E(k)|\partial_c\alpha\rangle\right].$$

So, we have $\sum_{\alpha=1}^{M}\epsilon_\alpha(k)\mathcal{F}^{\alpha\alpha}_{bc}(k) + \sum_{\alpha=1}^{M}\mathrm{Im}\,\epsilon_\alpha(k)\langle\partial_b\alpha|P_G(k)|\partial_c\alpha\rangle$.

To simplify further let us consider the terms with $H(k)$. We can rewrite $H(k)=\sum_{\gamma=1}^{N}\epsilon_\gamma(k)|\gamma\rangle\langle\gamma|$. Then we have the sum $\sum_{\alpha=1}^{M}\sum_{\gamma=1}^{N}\mathrm{Im}\,\epsilon_\gamma(k)\langle\partial_b\alpha|\gamma\rangle\langle\gamma|\partial_c\alpha\rangle$. We note that $\langle\partial_b\alpha|\gamma\rangle = -\langle\alpha|\partial_b\gamma\rangle$. Using this on both of the matrix elements, we have $\sum_{\alpha=1}^{M}\sum_{\gamma=1}^{N}\mathrm{Im}\,\epsilon_\gamma(k)\langle\alpha|\partial_b\gamma\rangle\langle\partial_c\gamma|\alpha\rangle$. Now, we note that this is the same as $-\sum_{\alpha=1}^{M}\sum_{\gamma=1}^{N}\mathrm{Im}\,\epsilon_\gamma(k)\langle\partial_b\gamma|\alpha\rangle\langle\alpha|\partial_c\gamma\rangle$ with the overall minus sign coming from taking the complex conjugate. Next, the sum over α can be done to give us $P_G(k)$. So, we have $-\sum_{\gamma=1}^{N}\mathrm{Im}\,\epsilon_\gamma(k)\langle\partial_b\gamma|P_G(k)|\partial_c\gamma\rangle$.

Combining both sets of terms we find: $\sum_{\alpha=1}^{M}\epsilon_\alpha(k)\mathcal{F}^{\alpha\alpha}_{bc}(k) - \sum_{\beta=M+1}^{N}\epsilon_\beta(k)\overline{\mathcal{F}}^{\beta\beta}_{bc}(k)$ where we have used the fact that $\overline{\mathcal{F}}^{\beta\beta}_{bc}(k) = \mathrm{Im}\,\langle\partial_b\beta|P_G(k)|\partial_c\beta\rangle$ is the $U(N-M)$ Berry curvature of the unoccupied bands. So, the magnetization is given by:

$$M^a = \frac{e\epsilon^{abc}}{2\hbar} \int \frac{d^dk}{(2\pi)^d} \left(\sum_{\alpha=1}^{M} \epsilon_\alpha(k) \mathcal{F}^{\alpha\alpha}_{bc}(k) - \sum_{\beta=M+1}^{N} \epsilon_\beta(k) \overline{\mathcal{F}}^{\beta\beta}_{bc}(k) \right). \tag{5.8}$$

So far this expression is generic and does not use the $\mathcal{TI}$ symmetry that is present in the models we consider, but there is a key simplification in the Berry curvature $\mathcal{F}^{\alpha\alpha}_{bc}(k)$ in the presence of this symmetry: $\mathcal{F}^{\alpha\alpha}_{bc}(k) = -\mathcal{F}^{\alpha\alpha}_{bc}(k)$ [39]. Similarly, we have $\overline{\mathcal{F}}^{\beta\beta}_{bc}(k) = -\overline{\mathcal{F}}^{\beta\beta}_{bc}(k)$ under $\mathcal{TI}$. Thus, nominally the (diagonal matrix components) of the Berry curvature vanish everywhere in the Brillouin zone. However, as discussed earlier, stable band touchings can act as sources of quantized Berry curvature. For example, if bands α_1 and α_2 touch along a FL they will have $\mathcal{F}^{\alpha_1\alpha_1}_{bc} = -\mathcal{F}^{\alpha_2\alpha_2}_{bc} = \Xi\pi\delta(\mathbf{k} - \mathbf{k}_0)$ (recall $\Xi = \pm 1$). Bands can touch each other along FLs with a crossing which can be linear as we consider in this section, quadratic or any higher order. The higher order band crossings will act as sources of Berry curvature with higher multiples of π, but they are not stable without the addition of more symmetries, and can be broken down to a number of linear crossings with the minimal, non-vanishing flux quantization. Bands which do not touch any other bands in the BZ, or touch along accidental crossings, will have vanishing Berry curvature at each point of the BZ and will not contribute to the magnetization. Since we are only interested in LTSMs we will not consider cases with point-like sources of Berry curvature coming, e.g., from Weyl or Dirac nodes, and instead only calculate the contributions from FLs.

Before we move on, we quote a technical result, derived in Appendix B.2, which is needed for further analysis:

$$\mathrm{Im}\,\langle \partial_b \alpha_1 | \alpha_2 \rangle \langle \alpha_2 | \partial_c \alpha_1 \rangle = -\mathrm{Im}\,\langle \partial_b \alpha_2 | \alpha_1 \rangle \langle \alpha_1 | \partial_c \alpha_2 \rangle$$

when $\mathcal{TI}$ symmetry is enforced. Hence $\mathrm{Im}\,\langle \partial_b \alpha_1 | \alpha_2 \rangle \langle \alpha_2 | \partial_c \alpha_1 \rangle = 0$ or $\pi\Xi\delta(k - k_0)$ when the α_1-th and α_2-th band either do not touch, or touch at k_0 respectively. If we consider the full non-abelian Berry curvature $\mathcal{F}^{\alpha\alpha}_{bc} = \sum_{\beta=M+1}^{N} \mathrm{Im}\,\langle \partial_b \alpha | \beta \rangle \langle \beta | \partial_c \alpha \rangle$, we see that terms involving bands $\beta \in M+1, \ldots, N$ that do not touch the α-th band along FLs drop out in the sum because they are zero. The ones that do touch satisfy the δ-function property. In the case that α touches a *single* band $\overline{\alpha}$ among the unoccupied bands along a FL, we have $\mathcal{F}^{\alpha\alpha}_{bc} = \pi\Xi\delta(k - k_{\alpha\bar{\alpha}})$ where $k_{\alpha\bar{\alpha}}$ is the location of the appropriate line node. This follows by looking at the only non-zero element in the sum and its properties under $\mathcal{TI}$. If we had more bands touching the α-th band along a nodal line, we have $\mathcal{F}^{\alpha\alpha}_{bc} = \sum_{\beta\,\mathrm{touch}\,\alpha} \pi\Xi_{\alpha\beta}\delta(k - k_{\alpha\beta})$. Similar properties hold for those unoccupied bands which form the FLs with the occupied ones, i.e., $\overline{\mathcal{F}}^{\beta\beta}_{bc} = -\sum_{\alpha\,\mathrm{touch}\,\beta} \pi\Xi_{\alpha\beta}\delta(k - k_{\alpha\beta})$.

In the magnetization integral, we have to integrate $\sum_{\alpha=1}^{M+1} \epsilon_\alpha \mathcal{F}_{bc}^{\alpha\alpha} - \sum_{\beta=M+1}^{N} \epsilon_\beta \overline{\mathcal{F}}_{bc}^{\beta\beta}$. For each δ-function in the first term, there is a corresponding δ-function in the second term with an opposing sign. Further, since the only contributions to the Berry curvature are at band touching points, the energies of the two bands must coincide $\epsilon_\alpha = \epsilon_{\overline{\alpha}}$. Crossings which are completely beneath the Fermi level do not contribute to the magnetization since they will cancel out in the sum over occupied bands from Eq. 5.8. Combining these results, we find that the quantity that needs to be integrated is $2\epsilon_\alpha \mathcal{F}_{bc}^{\alpha\alpha}$ for each band α that has a FL crossing the Fermi level. Thus, the expression for the magnetization can then be written as:

$$M^a = \sum_{\alpha \in \text{bands that cross at } \mu=0} \frac{e\epsilon^{abc}}{2\hbar} \int \frac{d^3k}{(2\pi)^3} 2\epsilon_\alpha \mathcal{F}_{bc}^{\alpha\alpha} \tag{5.9}$$

$$= \sum_{\alpha} \frac{e}{4\pi\hbar} \int_{\partial R_\alpha} \epsilon_\alpha(\mathbf{k})\, dk^a \tag{5.10}$$

where ∂R_α denotes the location of the line-node arising from the α-th band in the BZ at the Fermi level; $\partial R_\alpha = \varnothing$ if there is no band crossing for the α-th band at the Fermi level. Our result now shows the appropriate generalization to FLs of the energy difference between point-nodes that was previously shown to contribute to the EM response Weyl and Dirac semimetals. Thus, for each FL we can define the mixed space and time components of the 2-form:

$$\mathcal{B}^{0a} = \frac{\pi\Xi}{\hbar} \int_{\partial R} \epsilon(\vec{k}) dk^a = \frac{4\pi^2}{e} M^a \tag{5.11}$$

where the integration is over the nodal line. The total magnetization, and total 2-form, include a sum over all FLs that cross the Fermi-level. This is a 3D generalization of the results of [105, 78] that relate the magnetization of the 2D Dirac semimetal to the energy differences between the band-touching points. As an explicit illustration, in Appendix B.3 we calculate the magnetization for a generic two-band model and show that the results match our calculation.

One can give a microscopic argument for the existence of the magnetization/boundary currents for surfaces that harbor protected, low-energy modes. The surface states of $H_3(k)$ are initially flat-bands that do not disperse, and $\epsilon(k)$ will impart a dispersion as a function of (k_y, k_z). In general, this will create a bound surface current in the $y - z$ plane which is the consequence of a non-vanishing bulk magnetization density. There will be similar currents on surfaces without low-energy modes, but there is not as simple of an interpretation [78].

We confirm this result numerically by adding an extra term $t_{pp} \sin k_y \mathbb{I}$ to $H_3(k)$ and plotting the magnetization vs. m in Fig. 5.1b. The magnetization has the symmetry $M_z(m) = M_z(8-m)$, and we restrict

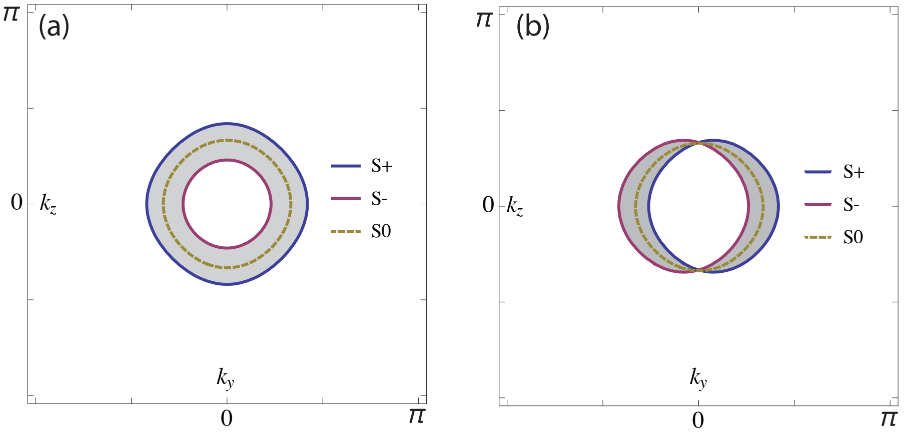

Figure 5.2: Dotted yellow lines represent initial four-fold degenerate Fermi-line ($S0$). Purple and blue solid lines represent spin-split Fermi-surfaces ($S+, S-$) with (a) a majority and minority spin Fermi-line induced by certain $\mathcal{T}$-breaking terms (b) spin-split Fermi-lines with equal sizes for each spin reminiscent of a Rashba-type splitting from spin-orbit terms induced by strain/inversion breaking. For both panels the gray shaded region represents the magnitude of the polarization in the x-direction from the projected areas of the Fermi lines after Z_2 overlap cancellation.

ourselves to $0 \leq m \leq 4$ in Fig. 5.1b. The magnetization is given by $\frac{M^z(m)}{t_{pp}} = \operatorname{sgn} m_{\mathcal{I}} \frac{e}{4\pi\hbar} \int_{-k_0}^{k_0} \sin k_y \, dk_z$. Again we have fixed $\beta, \gamma = 2$ so that there is only one FL, which has $\chi = +1$. The magnetization for this case can also be evaluated analytically from Eq. 5.11 since the energy only depends on k_y. The limits to which k_z extends for the FL can be calculated using the equation for the nodal line ($\cos k_y + \cos k_z = 2 - m/2$). Hence, on the nodal line, k_y is a function of k_z. The maximum value of $\cos k_y = 1$, and this means that the maximum/minimum k_z is given by $\pm k_{z0} = \pm \cos^{-1}(1 - m/2)$. This is valid only when $m < 4$, while for $m > 4$, the FL is centered around (π, π) instead of the origin. The magnetization is a function of m, and does not have a simple closed form expression. However, it does have a linear profile in the regime when m is small.

We have now completed our goal of showing that the LTSM EM response given by Eq. 5.1 can be related to the geometry of the line-nodes in energy momentum space. To conclude, we comment on the applicability of our results to real materials. The magnetic heterostructure proposed in [9, 71] breaks $\mathcal{T}$ explicitly, hence the spins are not degenerate, and the line nodes occur with just two overlapping bands. Thus, this model corresponds precisely to an effectively spinless case that has been described throughout this section, and our results can be directly applied. We expect, and have confirmed numerically, that this system will have a charge polarization. It is worth noting that the two form $\mathcal{B}_{\mu\nu}$ explicitly enters the continuum Hamiltonian of this system as, for example, $H = \vec{k} \cdot \vec{\Gamma} + i\mathcal{B}_{yz}\Gamma^0\Gamma^{yz}$ where Γ^μ are a set of Dirac matrices. One could pursue a continuum diagrammatic calculation of our result using this spinful system, but we will not do so in this thesis. In the case of spin degenerate models, which are found, for example, in the carbon allotrope materials in [67, 103], a further reflection symmetry is required to stabilize the LTSM arising from four overlapping bands as shown in [26]. For doubly-degenerate bands the charge polarization, being a $\mathbb{Z}_2$ quantity, is trivial. However, we can break spin degeneracy by including certain $\mathcal{T}$-breaking terms, or inducing additional spin orbit terms via strain, with the requirement that the FLs are not completely destabilized to a gapped, or point-node, phase. If we take two copies of our model, one for each spin, then two illustrations of initially spin-degenerate FLs (in the $k_x = 0$ plane) split by two types of spin-dependent terms are shown in Fig. 5.2. In these cases, the polarization P_x can be nontrivial and is not completely $\mathbb{Z}_2$ canceled. In fact, in both cases, the shaded areas correspond to the magnitude of the polarization, assuming a vanishing secondary weak invariant. The magnetization, on the other hand, is not a $\mathbb{Z}_2$ quantity and can be non-vanishing even for four-fold degenerate FLs. Hence, we expect that these systems would exhibit charge polarization when the FLs are spin-split via strain or other spin-dependent perturbations.

Chapter 6

Topological Crystalline Insulator

After the periodic table was complete, and after many exciting materials predictions and discoveries [54, 7, 58, 44, 64, 104, 113, 14], the classification of topological crystalline phases (TCIs) with point/space-group symmetries, such as reflection and discrete rotation, was initiated and continues to be an active area of research [30, 91, 29, 47, 94, 27, 90, 86, 3, 66, 18, 28, 48, 95, 112, 52, 87]. One highlight of this line of research was the prediction and experimental confirmation of a 3D TCI phase in PbSnTe [45, 88, 106, 23]. The topological properties of this system are protected by mirror symmetry, and it exhibits an insulating bulk with an even number of symmetry-protected Dirac-cone surface states on mirror-symmetric surfaces. The goal of thisthesis is to predict a characteristic electromagnetic response property that can be observed in PbSnTe and similar 3D TCIs protected by mirror symmetry (mTCIs).

Three-dimensional mTCIs are characterized by integer invariants: the mirror Chern numbers C_M [91]. To define and illustrate the consequences of the C_M let us consider a system with mirror symmetry $\mathcal{M}_z$ in the z-direction with $\mathcal{M}_z^2 = -1$. We can label eigenstates in the $k_z = 0$ and $k_z = \pi$ planes of the Brillouin zone (BZ) with the eigenvalues $\pm i$ of $\mathcal{M}_z$, and this allows one to define mirror Chern numbers $C_M(\Lambda) = \frac{C_{+i}(\Lambda) - C_{-i}(\Lambda)}{2}$, where $C_{\pm i}(\Lambda)$ is the usual Chern number of each mirror sector in the plane $\Lambda = 0, \pi$. When a C_M is non-vanishing, then, on mirror-invariant surfaces, say one normal to $\hat{x}$, there will be Dirac cones protected by the mirror symmetry. Furthermore, these cones lie in mirror invariant lines in the surface BZ projected from the corresponding Λ planes. The number of *stable* Dirac cones on each mirror line is given by $C_M(\Lambda)$ [91]. If we allow for broken translation symmetry, then the total number of stable surface cones is $\mathcal{C}_M \equiv C_M(\Lambda_1) + C_M(\Lambda_2)$. We illustrate the case with $C_M(0) = 2, C_M(\pi) = 0$ in Fig. 6.1 where we have two stable Dirac nodes on the surface perpendicular to $\hat{x}$ on the $k_z = 0$ plane.

In this chapter, we will show that mTCIs have a robust electromagnetic (EM) response that is determined by both a topological property (the existence of stable surface states determined by $\mathcal{C}_M$), and a geometrical property (the momentum and energy locations of the surface nodes) and are closely related to the EM response theory we have elucidated for the $2+1$ dimensional DSM. To show this, we first provide a lattice model for a mTCI built from two copies of a 3D time-reversal invariant TI on a cubic lattice. By itself, this system has a trivial topological magnetoelectric effect, but when coupled to a field b_μ which preserves the mirror symmetry, yet splits the surface Dirac nodes in energy-momentum space, an additional EM response is generated. In this thesis we only consider systems which also retain $\mathcal{T}$ symmetry since the experimentally realized mTCIs have $\mathcal{T}$-symmetry, and it will simplify some discussions.

For the simplest case with $\mathcal{C}_M = 2$, and with $\mathcal{T}$-symmetry, we can obtain a response theory of the mTCI via analogy with the 3D TI. In the continuum limit, the field b_μ in which we are interested couples to the theory precisely as a valley gauge field for the two species of surface Dirac cones/valleys. By performing a diagrammatic calculation in the continuum limit, we find that the effective response action is given by:

$$\mathcal{S}_{\text{TCI}}[A, b] = \frac{e}{8\pi^2} \int \mathrm{d}^4x \, \epsilon^{\mu\nu\rho\sigma} \Theta f_{\mu\nu} F_{\rho\sigma}, \tag{6.1}$$

where $\Theta = \pi$ inside the bulk of the mTCI, and $f_{\mu\nu}, F_{\mu\nu}$ are the field-strengths of b_μ and A_μ. The surface of the mTCI, can be thought of as a domain wall of Θ from π to 0, and Eq. (6.1) implies a surface response $S_{2D}[A, b] = \frac{e}{4\pi} \int_{\text{surf}} d^3x \epsilon^{\mu\nu\rho} b_\mu \partial_\nu A_\rho$ bound to the Θ domain wall. This surface response matches an EM response of a 2D Dirac semi-metal (DSM) with broken inversion symmetry if we identify b_μ with the energy/momentum separation of the Dirac node valleys [78, 5]. This might have been anticipated, since the even number of Dirac nodes on the surface of the mTCI is similar to the electronic structure of a 2D DSM. However, we find precisely half the coefficient that would occur in a 2D DSM with mirror and $\mathcal{T}$ ($\mathcal{T}^2 = -1$) symmetries, which makes it anomalous. Ultimately, the EM response of the mTCI implies localized charge and/or current density bound at defects in the b_μ field on the surface. To verify the validity of the result Eq. (6.1) obtained in the continuum limit, we explicitly calculate the microscopic origin of the response from a lattice model bound state calculation. Finally, we discuss experimental proposals and predictions.

6.1 Lattice model for TCI

Let us begin with the lattice Hamiltonian for a single copy of TI given by [76]:

$$H_{\text{TI}} = \sin k_x \Gamma^x + \sin k_y \Gamma^y + \sin k_z \Gamma^z - m(k_x, k_y, k_z)\Gamma^0, \tag{6.2}$$

where $m(k_x, k_y, k_z) = m + \cos k_x + \cos k_y + \cos k_z$ and m controls the bulk gap, and hence the topological phase. The matrices Γ^μ satisfy a Clifford algebra, and are given by $\Gamma^0 = \tau^x s^0$, $\Gamma^x = \tau^y s^0$, $\Gamma^y = \tau^z s^x$, $\Gamma^z = \tau^z s^z$, and $\Gamma^5 = \tau^z s^y$, where the zeroth components τ^0 and s^0 are identity matrices. We can take τ to be an orbital degree of freedom and s is spin; hence the time-reversal operator is $\mathcal{T} = is^y K$ where K is complex

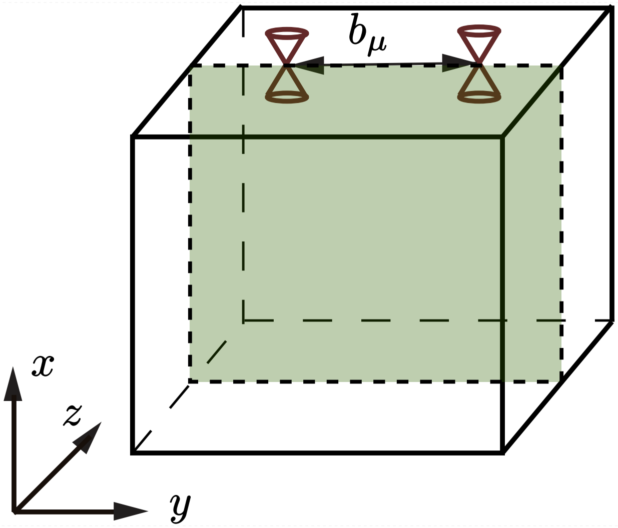

Figure 6.1: An illustration of a topological crystalline insulator in 3D with two surface Dirac cones localized on the surface perpendicular to the x-direction. $b_\mu = (b_0, b_y)$ is the energy-momentum separation of the Dirac nodes. For the model that we construct, the Dirac nodes are stabilized by $\mathcal{M}_z$ symmetry. We show the mirror plane in the bulk, and mirror lines on the surfaces by the green rectangle and its dashed boundary.

conjugation. Further, this model has mirror symmetries along the i-th directions with $\mathcal{M}_i = \Gamma^i\Gamma^5$ where $i = x, y, z$, and importantly $\mathcal{M}_i^2 = -1$. For example, we have $\mathcal{M}_z H_{\text{TI}}(k_x, k_y, k_z)\mathcal{M}_z^{-1} = H_{\text{TI}}(k_x, k_y, -k_z)$

To introduce a lattice model of the TCI, let us strictly enforce $\mathcal{M}_z$, and add an additional flavor degree of freedom σ^μ to the TI model (6.2). We will start with a block diagonal form, $H_{\text{TCI}}^{(0)} = \sigma^0 \otimes H_{\text{TI}}$. The topological phases and surface states of $H_{\text{TCI}}^{(0)}$ are determined by m. Without loss generality, we consider a case where $-3 < m < -1$; in this case there are two Dirac nodes (one for each copy) centered at the Γ-point on any surface (see Supplementary Material (SM) Sec. IIIA). $\mathcal{T}$-symmetry enforces $C_{+i}(\Lambda) = -C_{-i}(\Lambda)$, and this model has $C_M(0) = 2, C_M(\pi) = 0$, and $\mathcal{C}_M = 2$.

To produce our phenomena of interest various $\mathcal{M}_z$ preserving perturbations should be added to $H_{\text{TCI}}^{(0)}$. [1] Including some such perturbations we can write down a more generic lattice model for the TCI :

$$H_{\text{TCI}} = \sin k_x \sigma^0\Gamma^x + (\sin k_y \sigma^0 + b_y\sigma^y)\Gamma^y + \sin k_z \sigma^0\Gamma^z - (m + \cos k_x + \cos k_y + \cos k_z)\sigma^0\Gamma^0 + b_0\sigma^y, \quad (6.3)$$

where tensor products are implicit, and we will omit σ^0 from now on for compactness. One can verify that the Hamiltonian (6.3) is invariant under $\mathcal{M}_z$ and $\mathcal{T}$ (when $b_0 = 0$). One can also introduce b_x and b_z terms that couple to the Hamiltonian in a similar fashion to b_y, and will fill out the entire $b_\mu = (b_0, b_x, b_y, b_z)$ field. Specific mirror symmetries will enforce some entries to be zero, for example $\mathcal{M}_z$ enforces $b_z = 0$. We have

---

[1] We have continued using $\mathcal{T} = is^yK$ in the doubled TCI model as well. This is a basis choice that affects the necessity of using σ^y instead of σ^z in coupling b_μ to the model. However, one could use σ^z in the coupling instead, and use $\mathcal{T} = i\sigma^x s^y K$ as the definition of time-reversal operator acting on the Bloch Hamiltonian.

left out a non-zero b_x, and some other possible $\mathcal{M}_z$ and $\mathcal{T}$-invariant terms since we will usually specialize to a particular surface ($\hat{n} = \hat{x}$) for convenience, and these additional terms, when small, will not impact our analysis. We note that b_0 breaks time reversal, but not mirror, and we include it in the Hamiltonian because it leads to an interesting EM response contribution. We show in the Sec. C.5.1 that b_0 and b_y move the zero-energy Dirac nodes in the surface BZ from the Γ-point to $(E, k_y, k_z) = (\pm b_0, \pm b_y, 0)$, which, from Eq. (6.1), is exactly what we need to generate a non-vanishing EM response.

6.2 Electromagnetic response of TCI

For our choice of m the TCI Hamiltonian (6.3) is naturally expanded in the continuum limit around the Γ-point. For $b_0 = b_y = 0$, the continuum Hamiltonian has two identical copies, each with eigenvalue $\sigma^y = \pm 1$ [2] given by

$$H^{(a)} = k_x\Gamma^x + k_y\Gamma^y + k_z\Gamma^z + m'\cos\theta^{(a)}\Gamma^0 + m'\sin\theta^{(a)}\Gamma^5 \tag{6.4}$$

where $m' > 0$, $a = 1, 2$ corresponds to the two TI sectors with $\sigma^y = \pm 1$, and we have introduced a new angle parameter $\theta^{(a)}$ for each TI block. Under mirror symmetry $\mathcal{M}_z = \Gamma^z\Gamma^5$, the Hamiltonian satisfies: $\mathcal{M}_z H^{(a)}(k_x, k_y, k_z, \theta^{(a)})\mathcal{M}_z^{-1} = H^{(a)}(k_x, k_y, -k_z, -\theta^{(a)})$. Thus, mirror symmetry enforces $\theta^{(a)}$ to take quantized values of 0 or π. Indeed, our lattice model (6.3) maintains $\theta^{(a)} = \pi$ throughout the mTCI phase with $\mathcal{C}_M = 2$.

The topological magnetoelectric response [76, 25, 24] of such a system, which is obtained by gapping the surface Dirac nodes with a $\mathcal{T}$-breaking mass, is trivial since we have two copies of the usual TI. However, we now show that there is a response characteristic of a mTCI, once a $\mathcal{M}_z$-breaking mass term is added instead. To calculate the response in the continuum limit we couple each of the continuum Hamiltonians to its own gauge field $A_\mu^{(a)}$ via $\mathbf{k} \to \mathbf{k} + \mathbf{A}^{(a)}$. A diagrammatic calculation similar to those in [10, 76] shows that

$$S[A_\mu^{(a)}] = \frac{1}{32\pi^2}\int d^4x\, \theta^{(a)}(x)\epsilon^{\mu\nu\rho\sigma}F_{\mu\nu}^{(a)}F_{\rho\sigma}^{(a)} \tag{6.5}$$

where $F_{\mu\nu}^{(a)} = \partial_\mu A_\nu^{(a)} - \partial_\nu A_\mu^{(a)}$ is the curvature associated with the gauge field $A_\mu^{(a)}$. The symmetric combination of the gauge fields $A_\mu^{(1)}$ and $A_\mu^{(2)}$ represents the usual EM field A_μ, while the antisymmetric combination generates the energy-momentum separation of the Dirac nodes b_μ, i.e., $eA_\mu = \frac{1}{2}(A_\mu^{(1)} + A_\mu^{(2)}), b_\mu =$

---

[2] Note that, while it is more conventional to refer to $\sigma^z = \pm 1$ as two copies, we have chosen $\sigma^y = \pm 1$. This is merely a basis choice, and we have done so to preserve time-reversal symmetry, as the real materials examples do.

$\frac{1}{2}(A_\mu^{(1)} - A_\mu^{(2)})$. Thus, the total effective response action is given by:

$$S[A,b] = \frac{1}{32\pi^2}\int d^4x\, \epsilon^{\mu\nu\rho\sigma}\Big[e^2(\theta^{(1)}+\theta^{(2)})F_{\mu\nu}F_{\rho\sigma} + 2e(\theta^{(1)}-\theta^{(2)})f_{\mu\nu}F_{\rho\sigma} + (\theta^{(1)}+\theta^{(2)})f_{\mu\nu}f_{\rho\sigma}\Big] \tag{6.6}$$

where $f_{\mu\nu} = \partial_\mu b_\nu - \partial_\nu b_\mu$ is the curvature of the b_μ. The first (topological magnetoelectric effect) and second terms (the mTCI response of interest) both generate EM observables, though the former has a trivial/doubled coefficient. The current and charge responses depend on changes of the $\theta^{(a)}$ which naturally appear at surfaces, and with signs determined by symmetry breaking mass terms on the surface. A $\mathcal{T}$-breaking mass $m_R\Gamma^5$, similar to that for a TI [76], will generate $\Delta\theta^{(1)} = \Delta\theta^{(2)}$, while a $\mathcal{M}_z$-breaking but $\mathcal{T}$-preserving mass $m_A\sigma^y\Gamma^5$ will generate $\Delta\theta^{(1)} = -\Delta\theta^{(2)}$. The former will generate a (trivial) magnetoelectric response, while the latter will generate the mixed response:

$$S[A,b] = \frac{e}{8\pi^2}\int d^4x\,\Theta(x)\epsilon^{\mu\nu\rho\sigma}f_{\mu\nu}F_{\rho\sigma}, \tag{6.7}$$

where $\Theta(x) \equiv \theta^{(1)}(x) = -\theta^{(2)}(x)$. For our model we need to introduce the mass term $m_A\sigma^y\Gamma^5$. As noted, the preservation of $\mathcal{T}$ ensures the first term of Eq. (6.6), a surface Hall effect, vanishes. The sign of the m_A term also fixes the sign of $\Theta = \pi\mathrm{sgn}(m_A)$. The same effective action can also be derived in a direct diagrammatic calculation by evaluating the diagram in Fig. C.1 of the SM.

Let us illustrate the physical consequences of Eq. 6.7. The surface of the mTCI can be thought of as a domain wall of $\Theta = \Theta(\vec{x})$ where Θ changes from π to 0 traversing from the mTCI to vacuum. The effective action now reduces to a response localized at the Θ domain wall: $S_{\mathrm{TCI}} = e\mathrm{sgn}(m_A)/(4\pi)\int_{\mathrm{surf}} d^3x\epsilon^{\mu\nu\rho}f_{\mu\nu}A_\rho$. Taking a derivative of the effective action with respect to A_μ, i.e., $j^\mu = \delta S/\delta A_\mu$, we obtain the responses:

$$\begin{aligned} j^0{}_{\mathrm{surf}} &= -\frac{e\mathrm{sgn}m_A}{2\pi}\partial_z b_y, \quad j^z_{\mathrm{surf}} = -\frac{e\mathrm{sgn}m_A}{2\pi}\partial_0 b_y, \\ j^y{}_{\mathrm{surf}} &= \frac{e\mathrm{sgn}m_A}{2\pi}\partial_z b_0. \end{aligned} \tag{6.8}$$

These equations are analogs of the Streda formula and Ohm's law for a Hall current, where $\partial_z b_y$, $\partial_0 b_y$, and $\partial_z b_0$ are the "magnetic field" and "electric field" of the 1-form b_μ. The first equation of (6.8) indicates that additional charge density is bound at a flux/vortex core of $\vec{b}$. For a domain wall $b_y = |b_y|\mathrm{sgn}z$ on the yz-surface of the TCI, which has a "magnetic flux" of $\vec{b}$, Eq. (6.8) predicts that there exists a charge density of $j^0 = e|b_y|\mathrm{sgn}(m_A)/\pi$ trapped at the center of the domain wall. Macroscopically these responses arise from the half quantum Hall effect of each surface Dirac cone. They effectively see opposite electric and magnetic fields, but have opposite masses from the mirror-breaking m_A. Hence, their responses add and do not cancel. The defect structure that generates this response is illustrated for this case in Fig. 6.2. At the end we discuss the physical setup needed to experimentally probe this response.

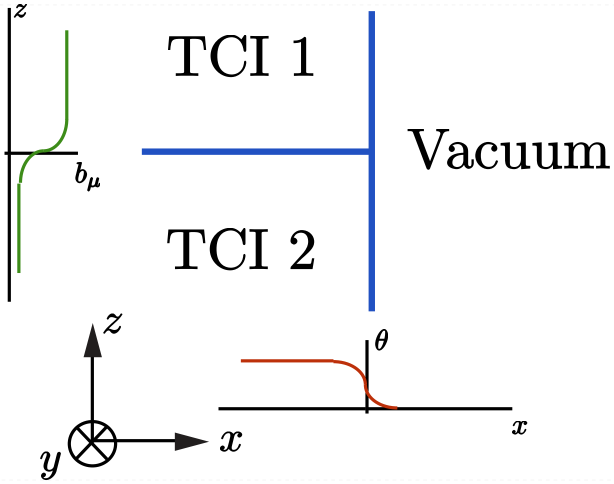

Figure 6.2: An illustration showing the kind of domain wall that can probe the response derived in Eq. 6.7. There is an interface between the TCI and the vacuum at $x = 0$ and an interface between two TCIs with different b_μ at $z = 0$. The quantities b_0, b_y naturally form a domain wall in the x direction at $z = 0$.

These results are based on the particular lattice model (6.3). However, they hold for any model with $\mathcal{C}_M = C_M(0) + C_M(\pi) = 2$. We show in the Sec. C.2 that for a system with $\mathcal{M}_z$ and $\mathcal{T}$ (or even with weakly broken $\mathcal{T}$), $\mathcal{C}_M = 2$ necessarily gives rise to two stable Dirac cones, and thus, upon the introduction of proper mirror-breaking mass terms, the response is described by Eq. (6.8) (see [97] for a discussion of the usual magnetoelectric response for $\mathcal{C}_M = 2$ systems).

For higher $\mathcal{C}_M = N$, there exist N stable surface Dirac nodes, and in principle more complex TCI responses can be obtained, but we leave discussion of those for future work (see [78] for some related examples in 2D DSMs). For cases with $\mathcal{C}_M = 0$, the surface Dirac cones can be gapped without breaking $\mathcal{M}_z$. However, if the bulk band inversions are at different k-points, then on certain surfaces the two Dirac cones can be located at different locations in the surface BZ. In this case gapping the Dirac cones, when mirror is preserved, requires breaking translational symmetry. By analogy with a weak TI [32, 65], we dub the system with surface Dirac nodes protected by $\mathcal{M}_z$ and translational symmetry a weak mTCI. When translation symmetry is intact, a weak mTCI can have a response (6.8) on certain surfaces with mirror symmetry, but not necessarily all of them.

6.3 Microscopic origin of the response

Eq. (6.8) is obtained from the continuum limit. However, from Eq. (6.3) we see $b_y\sigma^y$ couples to the system like a gauge field *only* in the continuum limit, i.e., when b_y is small. To obtain a complete picture, it is useful to verify the response from a microscopic lattice calculation.

From the TCI lattice model Eq. (6.3), we first solve for the surface Dirac states on the boundary of a mTCI ($x < 0$) with the vacuum ($x > 0$). The surface Dirac cones at $x = 0$ are given by

$$H_{\mathrm{2D}} = -\left(\sin k_y + b_y\sigma^y\right)s^x - \sin(k_z)s^z - m_A s^y\sigma^y, \tag{6.9}$$

where m_A is the mirror symmetry breaking mass, and the momentum range over which H_{2D} is valid is given by (see Sec. C.5.1) $|m - 1 + \cos k_y + \cos k_z| < 1$. In the continuum limit where $|b_y|$ is small, we can drop the sine in Eq. (6.9) and neglect the upper cutoff for $k_{y,z}$. Next, for the non-uniform b_y with a domain wall $b_y(z) = |b_{y0}|\mathrm{sgn}z$, the solution of Eq. (6.9) is given by

$$\Psi(x = 0, k_y, z) = \exp\left\{-\int_0^z [k_y\sigma^y + b_y(z')]dz'\right\}\Psi_0(k_y), \tag{6.10}$$

where $\Psi_0(k_y)$ satisfies $s^y\sigma^y\Psi_0(k_y) = -1$. Eq. (6.10) describes *two* bound states at each k_y, corresponding to the two eigenvalues of σ^y, both localized in the z-direction at the zero of the integrand of the exponent. Since b_y ranges from $-|b_{y0}|$ to $|b_{y0}|$, only states for which $|k_y| < |b_{y0}|$ have bound state solutions. Therefore, the total number of bound states is $2 \times 2|b_{y0}|/(2\pi/L_y)$. For a finite system, the surface $x = 0$ will also have an opposite domain wall with $b_y(z) = -|b_{y0}|\mathrm{sgn}z$. There exist the same number of bound states at the opposite domain wall with $s^y\sigma^y = 1$. With a small but finite m_A, the states localized at opposite domain walls are split away from zero energy and can be unambiguously filled (all states on one domain wall are filled). Due to the usual arguments [50], each state generates a localized charge $-\frac{e}{2}\mathrm{sgn}m_A$. Therefore we find that the bound state charge density is $j^0 = -e|b_{y0}|\mathrm{sgn}(m_A)/\pi$, and is in agreement with Eq. (6.8). We note that to see this response, we only need to break mirror symmetry with an infinitesimal mass term, while time reversal symmetry is intact.

For a larger magnitude of the domain wall $|b_{y0}|$, the charge response can deviate from the prediction from Eq. (6.8) and become non-universal, but this happens only with a gap closing transition in the bulk. To this end, for a sufficiently small $|b_{y0}|$, the Dirac nodes given by Eq. (6.9) simply get shifted. However, depending on the momentum range of validity of H_{2D}, a larger value of $|b_{y0}|$ can either eliminate the Dirac nodes or introduce additional Dirac nodes that can gap out each original one. In both cases, there is a gap closing in the bulk which indicates a transition from a mTCI to a trivial insulator. We show in the Sec. C.4 that, as long as the bulk gap does not close, the response (6.8) from the continuum model remains *exact* even in the lattice model. However for the cases when a large b_y eliminates or cancels the original Dirac nodes on the two sides of the domain wall, the charge density bound at the domain wall becomes non-universal.

6.4 Implication for experiments

As discussed above, the universal bulk contribution to the topological magneto-electric effect [76, 25, 24] is absent in a TCI; the Faraday effect and Kerr angles are non-universal when TR is explicitly and infinitesimally broken. However, our predicted response in Eq. (6.8) can be directly detected in other experiments, which requires engineering a domain wall or time gradient of the b_μ field, i.e., the momentum/energy displacement of the Dirac nodes. The surface Dirac nodes of a TCI can be moved in **k**-space via compression or dilation strains [89]. For SnTe, the surface Dirac nodes perpendicular to the (001) direction arise at $\pm\mathbf{k}_1, \pm\mathbf{k}_2$ and are protected by mirror symmetry along (110) and $(1\bar{1}0)$ axes, and are related by a C_4 rotation. With Isotropic compression or dilation, b_i's for both pairs of Dirac nodes increase or decrease. With uniaxial compression or stretching that breaks the C_4 symmetry, $b_{i,1}$ increases while $b_{i,2}$ decreases, or vice versa. A spatially inhomogeneous compression/dilation can thus generate the domain wall structure. A temporal gradient of b can be generated by surface acoustic waves produced by electromagnetically stimulating a piezo-electric layer deposited on the surface. The mass terms of the surface Dirac fermions can be generated [45, 22] through structural distortions where the atoms are displaced. After setting up the spatially-varying or time-dependent b_μ the localized charges can be detected by Scanning Tunneling Microscopy (STM) [8, 84] or the Scanning Single Electron Transistor Microscopy (SSETM) [109], while surface currents can be observed by a SQUID magnetometer.

Chapter 7

Discussion and Conclusions

In this thesis, we have explored the electromagnetic responses of topological semi-metals with point like Fermi surfaces and line-node Fermi surfaces in various spatial dimensions. We have seen that, generically, the quasi-topological contribution to the response depends on an n-form which represents the shape/geometry of the nodal surfaces in momentum space. To study these systems we first introduced a simple 1D model of a metal, which illustrated some of the general physical principles as well as helped to understand some response properties of the 3D Weyl semi-metal in a uniform magnetic field. This approach works because of the fact that the 1D response is embedded in the 3D Weyl semi-metal response, similar to the 1D topological insulator charge-polarization response being embedded in the 3D axion electrodynamic response [75].

After 1D we then moved onto the case of the 2D Dirac semi-metal which was constructed from layered 1D topological insulators that are stacked and coupled together. The gapless Dirac nodes which occur in this model each have a Chern-Simons response which, when written in terms of the electromagnetic gauge field, gives a polarization/magnetization which can be defined for a semi-metal, and is encoded in the momentum space positions and energies of the nodes. In this case, an energy difference between the nodes led to an edge current (bulk orbital magnetization) and a momentum separation between the nodes led to a boundary charge (bulk polarization). The $\mathcal{TI}$ symmetry ensures that the Dirac nodes are locally stable, immediately leads to the viable definition of charge polarization even in this gapless system.

We then moved onto 3D where we studied the properties of the Weyl semi-metal, and tested the predictions of the continuum field theory results with some numerical examples. Furthermore, we showed the precise anomaly cancellation calculation that connects the surface and bulk degrees of freedom. From there, the 3D DSM was then analyzed from the perspective that it is a layered QSH system. The 3D Dirac nodes separate Z_2 trivial regions of momentum space from Z_2 non-trivial regions, and the resultant response follows from the existence of these nontrivial QSH layers. As such, when a magnetic film is applied to a boundary with non-trivial surface states, we get boundary modes, and bound charge, localized on domain walls of the magnetization. Additionally a nonzero energy difference in the 3D Dirac nodes produces a localized current which runs along the domain wall.

The next model to be considered was the 3D LTSM with line-nodes in momentum space, where the response depended explicitly on a two form in momentum space. This two form furnished for us a polarization/magnetization response which depends on the shape of the embedded line-node in momentum space. While this approach is true for spin-polarized systems, we argued how $\mathbb{Z}_2$ cancellations would become relevant in considering experimental systems which are not spin polarized.

All of these responses followed in a straightforward way by considering the stacking construction of nth order weak topological insulators in lower dimensions. Along with determining the electromagnetic response, the stacking construction is also useful for discussing the properties of dislocations in WTIs and topological semi-metals [79, 48]. Additionally, the general pattern of metal/semi-metal responses is as follows. For a D-dimensional sample, a conventional Fermi-surface is a $D-1$-dimensional surface in momentum space. The response of this metal is given by a D-form $b_{\mu_1\ldots\mu_D}$ which is equivalent to a current via the identification $j^{\alpha}_{(b)} \sim \epsilon^{\alpha\mu_1\cdots\mu_D} b_{\mu_1\ldots\mu_D}$. Generically when the Fermi surface has dimension $D-q$ (codimension q), then the response is controlled by a $D-q+1$-form. These higher forms are sure to yield interesting physical predictions and connections with protected boundary modes.

Another immediate application of our results is to the bulk response action of the 3D topological crystalline insulator protected by mirror symmetry [29, 45, 88]. It has been shown that alloys of PbSnTe exhibit a mirror-symmetry protected topological phase. If we consider the [001] surface, then there will be four Dirac nodes which all have the same helicity [45], i.e. in our notation for the 2D Dirac semi-metal $\chi_a = +1$ for $a = 1, 2, 3, 4$. This response theory has been constructed explicitly in the case where the mirror Chern number is equal to 2 in Ch. 6 along with the experimental implications.

Appendix A

Appendices

A.1 Transformation from a Dirac semi-metal on the square lattice to the honeycomb lattice

In this section, we show that graphene can be thought of as an array of $1+1$-d TI wires. Let us begin with the one dimensional TI given by the following Bloch Hamiltonian:

$$H(\mathbf{k}) = t_x(1 + m - \cos k_x a)\sigma^x + t_x \sin k_x a\, \sigma^y \tag{A.1}$$

where t_x, m are parameters and a is the lattice constant. The system is gapped for all values of m except $m = 0$ or $m = 1$. Let us now induce tunneling in the y direction. In the following, the assumption of y being perpendicular to x is not needed. We could have this tunneling along an oblique direction and orthogonality is not required. In this case the Brillouin zone is not a simple square, but it can be a parallelogram. With hopping in the y-direction consider the modified Hamiltonian:

$$H(\mathbf{k}) = \left[t_x + t_x m - t_x \cos k_x a - t_\theta \cos(k_x a \cos\theta + k_y a \sin\theta)\right]\sigma^x + \left[t_x \sin k_x a + \bar{t}_\theta \sin(k_x a \cos\theta + k_y a \sin\theta)\right]\sigma^y.$$

where we have parameterized the y-direction by an angle θ with respect to the initial x-axis.

Let us now look at the graphene Hamiltonian. It is given by

$$H_G(\mathbf{k}) = -(t_1 + t_2 \cos \vec{k}\cdot\vec{a}_1 + t_3 \cos \vec{k}\cdot\vec{a}_2)\sigma^x + (t_2 \sin \vec{k}\cdot\vec{a}_1 + t_3 \sin \vec{k}\cdot\vec{a}_2)\sigma^y \tag{A.2}$$

where $\vec{a}_{1,2} = \sqrt{3}a\,(\cos(\pi/6), \pm\sin(\pi/6))$. For an easier comparison let us rotate this system in the counter-clockwise direction in real space by an angle $\pi/6$. The two lattice vectors are now given by $\vec{a}_1 = \sqrt{3}a\,(\cos(\pi/3), \sin(\pi/3))$ and $\vec{a}_2 = \sqrt{3}a\,(1, 0)$. Labeling $\sqrt{3}a = b$, we reduce the Hamiltonian to

$$H_G(\mathbf{k}) = -[t_1 + t_2 \cos(k_x b \cos\pi/3 + k_y b \sin\pi/3) + t_3 \cos k_x b]\sigma^x + [t_3 \sin k_x b + t_2 \sin(k_x b \cos\pi/3 + k_y b \sin\pi/3)]\sigma^y \tag{A.3}$$

We note that the Hamiltonians in Eq. A.3 and Eq. A.2 are the same with the following identifications. $t_1 \to -(t_x + t_x m)$, $t_2 \to t_\theta$, $t_3 \to t_x$ with the additional constraint $t_\theta = \bar{t}_\theta$.

Let us now set all parameters in our model A.2 to 1 except for $\bar{t}_\theta$. From our previous statement we know that this will be exactly the same as graphene when $\bar{t}_\theta = t_\theta = 1$. We want to show that the effect of deforming $\bar{t}_\theta$ away from this point is to move the Dirac nodes around in the BZ. Let us look at the gapless points of our model which are the solutions to

$$\sin(k_x a) + \bar{t}_\theta \sin(k_x a \cos\theta + k_y a \sin\theta) = 0 \tag{A.4}$$

$$\cos(k_x a) + \cos(k_x a \cos\theta + k_y a \sin\theta) = 1 + m. \tag{A.5}$$

In the limit that $\bar{t}_\theta = 1$, we have $(\frac{\pm 1}{a}\cos^{-1}(\frac{1+m}{2}), \frac{\mp(1+\cos\theta)}{a\sin\theta}\cos^{-1}(\frac{1+m}{2}))$ as the gapless points. On the other hand, if $\bar{t}_\theta = 0$, we have $(0, \pm\cos^{-1}(m))$ as the gapless points. As long as $|1+m| < 2$, and $0 \le \bar{t}_\theta \le 1$, we get two gapless points in the spectrum but their location depends generically on the model parameters. In this thesis, we always use the model in A.2 in the limit of $t_x = 1$, $t_\theta = 1$, $\bar{t}_\theta = 0$ for describing Dirac semi-metal physics with two bands.

A.2 Exact solution for boundary states in topological semimetal lattice models

In this Appendix we will study the edge states of the various topological semi-metal lattice models. The solution can be found analytically for the Dirac-type models we have been using following the results of [21, 58]. We will begin by solving for the edge states of the two-band lattice Dirac model, i.e., the minimal model for 1+1-d and 2+1-d topological insulators. We will then go on to modify these models to form Dirac and Weyl semi-metal states and solve for their boundary modes.

A.2.1 Exact solution for edge states of the lattice Dirac model

Consider the model given by

$$\begin{aligned} \mathcal{H} &= \epsilon(k) I_{2\times 2} + d_a(k)\sigma^a \\ d_a(k) &= (A\sin(k_1), d_2(k_2), M(k)) \\ M(k) &= M - 2B[2 - \cos(k_1) - \cos(k_2)] \end{aligned} \tag{A.6}$$

where $d_2(k_2)$ is an unspecified, but odd, function of k_2, and A, B, M are model parameters. Let us fix the sign of $A > 0$ and $B > 0$. Additionally, we assume that $\epsilon(k) = 0$ for now, but we will add it back in later. Note that with $\epsilon(k) = 0$ and $d_2(k_2) = -d_2(-k_2)$ the model is particle-hole symmetric with the symmetry operator $C = \sigma^x$; it is also inversion symmetric with $\mathcal{I} = \sigma^z$. The energy eigenvalues are given by

$$\begin{aligned} E_{\pm} &= \pm\sqrt{d_a d_a} \\ &= \pm\sqrt{A^2\sin^2(k_1) + d_2^2(k_2) + M^2(k)}. \end{aligned} \tag{A.7}$$

This spectrum is a gapped insulator as long as $\sqrt{d_a d_a} \neq 0$. One gapless critical point of this model occurs when $k_1 = k_2 = M = 0$ and for $M < 0$ ($M > 0$) the model is in a trivial (topological) insulator phase.

When the system is tuned to the non-trivial phase there are gapless edge states which can be shown explicitly in a finite strip geometry or a cylinder geometry. Let us assume that the system has boundaries at $x_1 = 0, L$ and is infinite in the x_2 direction. Since we have an inhomogeneous system with open boundaries we need to Fourier transform the Bloch Hamiltonian back from k_1 to x_1 via the substitution

$$c_{\vec{k}} = \frac{1}{\sqrt{L}}\sum_j e^{ik_1 x_1(j)} c_{k_2,j}. \tag{A.8}$$

This reduces the Hamiltonian to

$$\begin{aligned} \mathcal{H} &= \sum_{k_2,j}(\mathcal{M}c^{\dagger}_{k_2,j}c_{k_2,j} + \mathcal{T}c^{\dagger}_{k_2,j}c_{k_2,j+1} + \mathcal{T}^{\dagger}c^{\dagger}_{k_2,j+1}c_{k_2,j}) \\ \mathcal{M} &= A\sin(k_2)\sigma^2 - 2B\left[2 - \frac{M}{2B} - \cos(k_2)\right]\sigma^3 \\ \mathcal{T} &= \frac{iA}{2}\sigma^1 + B\sigma^3. \end{aligned} \tag{A.9}$$

Since we are interested in the exponentially localized edge states, we will focus on a solution ansatz of the form

$$\psi_\alpha(j) = \lambda^j \phi_\alpha \tag{A.10}$$

where λ is a complex number, j is the site index in the x_1 direction, and ϕ_α is a 2 component spinor with $\alpha = 1, 2$. We will first look for a solution at $k_2 = 0$, and since the Hamiltonian is particle-hole symmetric, the mid-gap edge state for this momentum will occur at $E = 0$. Acting with the Hamiltonian at $k_2 = 0$ on our ansatz yields the equation

$$\left[\frac{iA}{2}(\lambda^{-1}-\lambda)\sigma^1 + B(\lambda+\lambda^{-1})\sigma^3 + \mathcal{M}(0)\sigma^3\right]\phi = 0.$$

Multiplying this equation on both sides by σ^3 gives us

$$\frac{A}{2}(\lambda^{-1}-\lambda)(i\sigma^3\sigma^1)\phi = -[B(\lambda+\lambda^{-1}) + \mathcal{M}(0)]\phi. \tag{A.11}$$

The operator $i\sigma^3\sigma^1$ has eigenvalues ±1. First consider $i\sigma^3\sigma^1\phi = -\phi$, under which Eq. A.11 becomes a quadratic equation in λ which can be solved to find:

$$\lambda_{(1,2)} = \frac{-\mathcal{M}(0) \pm \sqrt{\mathcal{M}^2(0) + (A^2 - 4B^2)}}{A+2B}. \tag{A.12}$$

Thus, from the quadratic equation we have two λ solutions for the -1 eigenvalue (chirality) of $i\sigma^3\sigma^1$. For every solution λ we find that λ^{-1} is a solution for $i\sigma^3\sigma^1\phi = +\phi$, and thus for each eigenvalue of $i\sigma^3\sigma^1$ there are two possible values of λ. Let us label the eigenstates of $i\sigma^3\sigma^1$ as $\phi_\pm$ corresponding to the chiralities. The most general edge state can by written as

$$\psi_j(k_2=0) = \left(a\lambda^j_{(1)} + b\lambda^j_{(2)}\right)\phi_+ + \left(c\lambda^{-j}_{(1)} + d\lambda^{-j}_{(2)}\right)\phi_- \tag{A.13}$$

but to satisfy open boundary conditions we must have $a=-b$ and $c=-d$ since $\phi_\pm$ are linearly independent. Additionally, since the mode must be normalizable, we can only keep positive or negative powers of λ and thus only one normalizable mode exists (on each edge) as long as the λ do not lie on the unit circle, i.e. $|\lambda_{(1,2)}| \neq 1$. If $|\lambda_{(1,2)}| = 1$ an edge state solution does not exist at all. We also note that solutions with eigenvalues λ and λ^{-1} are localized on opposite edges of the system based on the form of Eq. A.13.

Now, let us generalize this solution for $k_2 \neq 0$. We see that the term $\cos(k_2)$ simply acts as a shift of the parameter M and can be easily accounted for. We also see that $[i\sigma^3\sigma^1, \sigma^2] = 0$ and clearly $[i\sigma^3\sigma^1, I_{2\times2}] = [\sigma^2, I_{2\times2}] = 0$. So, the terms $d_2(k_2)\sigma^2$ and $\epsilon(k_2)I_{2\times2}$ can simply be included as k_2 dependent shifts of the energy. These terms change the energy dispersion of the edge states, but the eigenstates remain the same. The energy for the edge state for any k_2 is given by

$$E_\pm(k_2) = \epsilon(k_2) \mp d_2(k_2). \tag{A.14}$$

Importantly, this dispersion does not hold across the entire k_2 Brillouin zone because there will exist some values of k_2 where the values of λ coming from a solution of

$$\begin{aligned}\lambda_{(1,2)}(k_2) &= \frac{-m(k_2,M) \pm \sqrt{m(k_2,M)^2+(A^2-4B^2)}}{A+2B} \\ m(k_2,M) &= -2B[2-M/2B-\cos(k_2)] \end{aligned} \tag{A.15}$$

do not yield normalizable modes. For the edge states to be normalizable, we have to satisfy the condition that $|\lambda_{(1,2)}| \neq 1$ which can be reduced to

$$-2B < m(k_2,M) < 2B \tag{A.16}$$

for each k_2. The special points in k_2-space where the inequalities become equalities are places in the energy spectrum where the edge states merge with the delocalized bulk states. Beyond these special values of k_2 the edge states no longer exist. This result, which consists of the dispersion, wavefunctions, and conditions for normalizablity represents the full analytic solution of the lattice edge states.

A.3 Edge theory for two dimensional semimetal

Based on the solution for the 2-band Dirac model we can immediately adapt it to the case of topological semi-metal states with minor modifications. First, let us consider the 2+1-d Dirac semi-metal including the possibility of the inversion breaking (m_A) and time-reversal breaking (m_B) mass terms discussed in Section 3. The Hamiltonian takes the form

$$\begin{aligned}\mathcal{H} &= \epsilon(k)I_{2\times 2}+d_a(k)\sigma^a \\ d_a(k) &= (A\sin k_1, m_A+m_B\sin k_2, M(k)) \\ M(k) &= M-2B[1-\cos k_1-\cos k_2] \\ \epsilon(k) &= \gamma\sin(k_2).\end{aligned}$$

Depending on the values of M and B this Hamiltonian can have Dirac nodes at $(0,\pm k_0)$ where $k_0 = \cos^{-1}(-M/2B)$. For a cylinder geometry with open boundary in the x_1 direction and periodic boundary conditions in the x_2 direction, this model will have edge states when the Dirac nodes exist. The edge states will occur between the Dirac nodes, but depending on the values of M and B they either stretch between the nodes within the Brillouin zone or across the Brillouin zone boundaries. For a choice such that they stretch within the Brillouin zone, the energies of the edge state branches on the two edges are given by

$$E_{\pm} = \gamma \sin(k_2) \mp |m_A + m_B \sin(k_2)| \quad |k_2| < k_0. \tag{A.17}$$

The restriction on the range of k_2 arises from a modified condition on normalizability through the relation

$$\begin{aligned} -2B &< m(k_2, M) < 2B \\ m(k_2, M) &= -2B[1 - M/2B - \cos(k_2)]. \end{aligned} \tag{A.18}$$

We can observe several interesting details from Eq. A.17. First we see that if we let $m_A = \gamma = 0$ but $m_B \neq 0$, then the dispersion matches that of the edge states of the 2+1-d Chern insulator [37] as it must since the m_B term is exactly the mass term required to convert a 2D Dirac semi-metal into a Chern insulator. If only m_A is non-zero and $m_B = \gamma = 0$, then we get two flat bands, one band on each edge. Finally, if we have $\gamma \neq 0$ and $m_A \neq 0$ but $m_B = 0$, then the two flat bands from the previous case will each disperse, and at half-filling there will be bound currents on each edge that, in the limit $m_B \to 0$ give rise to the magnetization discussed in Section 3. This matches our expectation because if M and B are tuned to values where $k_0 \neq 0$ as we have assumed, then for non-zero γ there will be an energy difference between the two Dirac nodes given by $\Delta E = 2|\gamma \sin k_0|$.

A.4 Edge theory in the case of the Weyl semimetal

The Weyl semi-metal also has a Hamiltonian which is given by the form of Eq. A.17 where

$$\begin{aligned} \mathcal{H} &= \epsilon(k_2, k_3) I_{2\times 2} + d_a(k)\sigma^a \\ d_a(k) &= (A \sin k_1, A \sin k_2, M(k)) \\ M(k) &= M - 2B[2 - \cos k_1 - \cos k_2 - \cos k_3] \end{aligned}$$

where we can let $\epsilon(k)$ be a generic function of k_2, k_3. This Hamiltonian has two gapless Weyl nodes for $|M/2B| < 1$ at $(k_1, k_2, k_3) = (0, 0, \pm k_0)$ where $k_0 = \cos^{-1}(-M/2B))$. Let us assume again that our system has boundaries at $x_1 = 0, L$ and that it is periodic in the other two directions. The main change between this case and the previous ones is that the condition for existence of these edge states at each momentum gets modified because the mass $m(k, M)$ is now parameterized by k_2 and k_3. The new normalizability condition that must be satisfied is given by

$$\begin{aligned} -2B &< m(k,M) < 2B \\ m(k,M) &= -2B[2 - M/2B - \cos k_2 - \cos k_3]. \end{aligned} \tag{A.19}$$

The edge state energies in this case are given by $E_{\pm} = \epsilon(k_2, k_3) \mp |A \sin k_2|$.

Let us consider a simple case first where $\epsilon(k) \equiv 0$. We want to consider the structure of the boundary modes on a surface with the normal vector in the x-direction and the surface Brillouin zone is the (k_2, k_3) plane. If we set the chemical potential to zero, we see that there exist Fermi arcs in this plane when $E_{\pm} = \mp|A \sin k_2| = 0$ which allows for $k_2 = 0, \pi$ and does not explicitly depend on k_3. The correct value of k_2 depends on the particular choice of M and B, so without loss of generality let us choose $k_2 = 0$. The boundary state existence condition of Eq. A.19, which does depend on k_3, can be simplified to give us the condition that boundary states are only present when $|k_3| < k_0$. Thus, for this case there exist Fermi arcs that are straight lines which go from $(k_2, k_3) = (0, -k_0)$ to $(k_2, k_3) = (0, k_0)$ in the surface Brillouin zone.

To get more non-trivial Fermi-arc shapes inversion symmetry needs to be broken to lift the degeneracy between the arcs on the two edges. Let us consider the Hamiltonian given by A.19 with $\epsilon(k) = \gamma \sin k_3$. The energy is given by $E_{\pm} = \gamma \sin k_3 \mp |A \sin k_2|$. With the chemical potential again set at $\mu = 0$ and, for example $\gamma = A/2$, we see that the points in the Fermi arc must satisfy $\sin k_3 = \pm 2 \sin k_2$ and Eq. A.19. The solutions to these constraints are complicated functions of (k_2, k_3) and must, in general, be solved numerically.

A.5 Tunneling between edge states

In this section, we will use our model of the boundary states for the topological semimetals to study properties at interfaces between semimetals with different Lorentz violating parameters, and thus different boundary state structures. Let us consider the interface between two, semi-infinite 2D DSMs first. Assume that the interface is at $x = 0$ with parameters for $x \leq 0$ given by A, B, M, γ and for $x > 0$ given by A', B', M', γ'.

The lattice Hamiltonian for $x \leq 0$ is given by

$$\mathcal{H} = \left(\sum_{j, k_2 = -\infty}^{j=-1} H_j(k_2) \right) + \mathcal{M} c^{\dagger}_{0,k_2} c_{0,k_2} + \mathcal{T} c^{\dagger}_{0,k_2} c_{1,k_2} + \mathcal{T}^{\dagger} c^{\dagger}_{1,k_2} c_{0,k_2} \tag{A.20}$$

where H_j is the lattice Hamiltonian we have been previously using. To be specific,

$$\begin{aligned}\mathcal{M} &= \gamma \sin k_2 \mathbb{I} + (m_A + m_B \sin k_2)\sigma^2 - 2B\left[1 - \frac{M}{2B} - \cos k_2\right]\sigma^3 \\ \mathcal{T} &= \frac{iA}{2}\sigma^1 + B\sigma^3. \end{aligned} \tag{A.21}$$

The Hamiltonian for $x > 0$ has a similar form, just with different parameters. We notice that there is a natural hopping term to connect the two systems. The matrix element for tunneling from site 0 to site 1 is $\mathcal{T}^\dagger$ and the matrix element for tunneling from site 1 to site 0 is $\mathcal{T}$.

Assume that the edge states are of chiralities c, c' which take on the values $+1, -1$. The chirality of the state is simply defined as its eigenvalue under the $i\sigma^3\sigma^1$ matrix discussed in the previous section. The state on the left edge and right edge are given by $\phi_c, \phi_{c'}$ respectively. The Hamiltonian in the edge subspace is given by

$$H = \begin{pmatrix} \langle \phi_c | \mathcal{M} | \phi_c \rangle & \langle \phi_c | \mathcal{T} | \phi_{c'} \rangle \\ \langle \phi_{c'} | \mathcal{T}^\dagger | \phi_c \rangle & \langle \phi_{c'} | \mathcal{M}' | \phi_{c'} \rangle \end{pmatrix}. \tag{A.22}$$

We can evaluate the matrix elements in each case by using the fact that $|\phi_\pm\rangle$ are eigenstates of $-\sigma^2$. When the chiralities are opposite, i.e $cc' < 0$, we have $\langle \phi_\pm | \mathcal{M} | \phi_\pm \rangle = \gamma \sin k_2 \mp (m_A + m_B \sin k_2)$, $\langle \phi_+ | \mathcal{T} | \phi_- \rangle = \langle \phi_+ | \mathcal{T} | \phi_- \rangle^\dagger = B - A/2$. Off diagonal terms turn out to be zero if $cc' > 0$ i.e. we have $\langle \phi_+ | \mathcal{T} | \phi_+ \rangle = \langle \phi_- | \mathcal{T} | \phi_- \rangle = 0$. So, in the case of $cc' > 0$, which is to say we have the same chirality for the edge states the tunneling Hamiltonian is given by

$$H = \frac{\gamma + \gamma'}{2} \sin k_2 \mathbb{I} \pm \left(m_A + (m_B + \frac{\gamma - \gamma'}{2}) \sin k_2 \right) \sigma^3. \tag{A.23}$$

We see that the edges don't mix and are only completely gapped when the inversion symmetry is broken (i.e. m_A non-zero). When they are of opposite chiralities, the tunneling Hamiltonian is given by

$$\begin{gathered} H = \frac{\gamma + \gamma'}{2} \sin k_2 \mathbb{I} \pm \\ \left(m_A + (m_B + \frac{\gamma - \gamma'}{2}) \sin k_2 \right) \sigma^3 + (B - A/2)\sigma^1. \end{gathered} \tag{A.24}$$

We see that the term $B - A/2$ when nonzero acts like a mass term and gaps the edge out in this case. In the models we consider, $A = 1, B = -1/2$ and $A - B/2 \neq 0$. In the case when the edge modes have the same chirality the ± signs in Eq. A.23 refer to the chirality itself. In the case when the edge modes have the opposite chirality the ± signs in Eq. A.24 refer to whether the left edge has + or − chirality.

An important thing to notice is that M and M' do not enter the edge Hamiltonians, however it still has an important effect. The above analysis tells us that the edge modes can gap each other out when they both exist at the same momentum k_2. However, it is M and M' that control where the Dirac nodes are and therefore the domain of existence of the edge states in k_2. So, those edge states on one edge with a momentum k_2 which do not have a counterpart on the other edge will remain gapless regardless. Thus, the edge states will only be removed if the domain of existence overlaps in the two systems.

A.6 Tunneling in Weyl semimetals

Let us start off with the Hamiltonian which is of the same flavor as before with

$$\begin{aligned} \mathcal{M} &= A\sin k_2\sigma^2 - 2B\left[2 - \frac{M}{2B} - \cos k_2 - \cos k_3\right]\sigma^3 \\ \mathcal{T} &= \frac{iA}{2}\sigma^1 + B\sigma^3. \end{aligned} \tag{A.25}$$

Let us assume that again that we have an edge at $x = 0$ and the same setup as the 2D Dirac semi-metal. For $x \leq 0$ we have parameters A, B, M and for $y > 0$ we have parameters A', B', M'. Our analysis from the previous section helps us immensely here. The edge states $|\phi_c\rangle$ are again eigenvectors of $-\sigma^2$. The edge Hamiltonian when we have same chiralities on the two edges is again given by

$$H = \pm A\sin k_2\mathbb{I}. \tag{A.26}$$

On the other hand, when the edge states have opposite chiralities, the edge Hamiltonian is

$$H = \pm A\sin k_2\sigma^3 + (B - A/2)\sigma^1. \tag{A.27}$$

So, yet again, when the edges have opposite chiralities, the term $B - A/2$ acts like a mass term and gaps the modes out. This is of course only valid if the edge states exist at the same k_3. Edge states with a momentum k_3 which do not have a counterpart on the other edge will remain gapless. The ± signs are related to the same definitions in the previous section. There could be more complications when a term $\epsilon(k_2, k_3)\mathbb{I}$ is added to the Hamiltonian. This modifies the surface Fermi arcs from being straight lines to some other complicated structure. When this happens, only those states on the surface which are degenerate at the same momenta k_2, k_3 gap each other out.

A.7 K-matrix formalism

The action in Eq. 3.41 can be rewritten as

$$S_{eff} = \frac{e^2}{4h}\int d^3x K_{ab}\epsilon^{\mu\nu\rho}A_{(a)\mu}\partial_\nu A_{(b)\rho} \tag{A.28}$$

where $K_{ab} = \chi_a g_a \delta_{ab}$. From these independent currents and gauge fields we can extract the electromagnetic response which couples democratically to each Dirac cone via a 2N-dimensional "charge"-vector $t_{EM} = (e, e, \dots, e, e)^T$ where e is the electron charge. The Hall conductivity is then $\sigma_{xy} = \frac{1}{2h}t_{EM}^T K t_{EM}$. We can also define a valley charge vector $t_V = (\chi_1, \chi_2, \dots, \chi_{2N})^T$. We can define a valley Hall conductivity via $\sigma_{xy}^V = \frac{1}{h}t_{EM}^T K t_V$ which determines the valley current in response to an electromagnetic field. Finally, we can define a valley-valley Hall conductivity via $\sigma_{xy}^{VV} = \frac{1}{2h}t_V^T K t_V$ which determines the amount of valley current that flows in response to a valley electromagnetic field (generated, for example, by strain).

In general we may have other interesting types of charge vectors t_S if we have more symmetries, e.g., spin-rotation symmetry, or point-group symmetries, that correspond to the quantum numbers carried by the corresponding Dirac cones. We can define charge and valley Hall conductivities of those additional quantum numbers by $\sigma_{xy}^S = \frac{1}{h}t_{EM}^T K t_S$ and $\sigma_{xy}^{VS} = \frac{1}{h}t_V^T K t_S$. As an example, suppose that we have translation symmetry in spacetime, which gives rise to conserved momentum and energy. For translation along the x-direction each Dirac cone has a momentum component $k_{(i)}^x$ leading to a charge vector $t_x = \hbar(k_{(1)}^x, k_{(2)}^x, \dots, k_{(2N)}^x)^T$. We could use this to define the charge polarization along the y direction as $P_1^y = \frac{1}{2h}t_{EM}^T K t_x$. This can be written in a more covariant way as $P_1^a = \frac{1}{2h}\epsilon^{ab}t_{EM}^T K t_b$ and $M = \frac{1}{2h}t_{EM}^T K t_\epsilon$ where $t_\epsilon = \hbar(\epsilon_{(1)}, \epsilon_{(2)}, \dots, \epsilon_{(2N)})^T$.

Let us consider a few explicit examples. The simplest case is $N = 1$ where the the Dirac cones are specified, without loss of generality by $(+, \mathbf{P}_{(1)}, \epsilon_1, g_1)$and $(-, \mathbf{P}_{(2)}, \epsilon_2, g_2)$. Up to global signs, the two possible K-matrices are $K_1 = \mathbb{I}$ and $K_2 = \sigma^z$. The K-matrix K_1 (K_2) corresponds to the case of a time-reversal symmetry (inversion symmetry) breaking anomalous response. The electromagnetic and valley charge vectors for both K-matrices are $t_{EM} = (e, e)^T$ and $t_V = (1, -1)^T$. For K_1 we easily find $\sigma_{xy} = e^2/h$, $\sigma_{xy}^V = 0$ and $\sigma_{xy}^{VV} = 1/h$. For K_2 we have $\sigma_{xy} = \sigma_{xy}^{VV} = 0$ and $\sigma_{xy}^V = \frac{e}{h}$.

Now let us consider translation invariance so that we can construct a charge vector associated to the energy and momentum of each Dirac point $t_x = (k_{(1)x}, k_{(2)x})$, $t_y = (k_{(1)y}, k_{(2)y})$, $t_\epsilon = (\epsilon_{(1)}, \epsilon_{(2)})$. We can see that the Polarization would be $P_1^a = \frac{1}{4\pi}\epsilon^{ab}(k_{(1)b} + k_{(2)b})$ when $K = \mathbb{I}$ and $P_1^a = \frac{e}{4\pi}\epsilon^{ab}(k_{(1)b} - k_{(2)b})$ when $K = \sigma^z$. The Magnetization would be given by $M = \frac{e}{4\pi}(\epsilon_{(1)} - \epsilon_{(2)})$ when $K = \sigma^z$ and $M = \frac{e}{4\pi}(\epsilon_{(1)} + \epsilon_{(2)})$ when $K = \mathbb{I}$.

We can also consider a more complicated example with $N = 2$ which will have four Dirac cones. As an explicit example, take $\chi_1 = \chi_2 = 1$ and $\chi_3 = \chi_4 = -1$. The electromagnetic and valley charge vectors are $t_{EM} = (e, e, e, e)^T$ and $t_V = (1, 1, -1, -1)$. We can also define two other useful, linearly-independent charge vectors $t_U = (1, -1, -1, 1)$ and $t_W = (1, -1, 1, -1)$. There are $2^4 = 16$ possible K-matrices but we only need to consider eight since the other eight differ by an overall sign. These eight are

$$\begin{aligned} K_1 &= \mathrm{diag}[1, 1, 1, 1] & K_2 &= \mathrm{diag}[1, 1, -1, -1] \\ K_3 &= \mathrm{diag}[1, -1, -1, 1] & K_4 &= \mathrm{diag}[-1, 1, -1, 1] \\ K_5 &= \mathrm{diag}[1, 1, -1, 1] & K_6 &= \mathrm{diag}[1, -1, 1, 1] \\ K_7 &= \mathrm{diag}[-1, 1, 1, 1] & K_8 &= \mathrm{diag}[1, 1, 1, -1]. \end{aligned} \tag{A.29}$$

We can tabulate their (dimensionless) electromagnetic responses via $\frac{1}{2} t_{EM}^T K t_\alpha$ where α = EM, V, U, and W. We find :

$$\left[\begin{array}{ccccc} & EM & V & U & W \\ K_1 & 2 & 0 & 0 & 0 \\ K_2 & 0 & 2 & 0 & 0 \\ K_3 & 0 & 0 & 2 & 0 \\ K_4 & 0 & 0 & 0 & 2 \\ K_5 & 1 & 1 & 1 & 1 \\ K_6 & 1 & -1 & 1 & -1 \\ K_7 & 1 & -1 & -1 & 1 \\ K_8 & 1 & 1 & -1 & -1 \end{array}\right]. \tag{A.30}$$

We note that while all of these results are simple and appealing, we must be careful to handle the cases when the response coefficients have a Z_2 nature, i.e. when they are connected to the charge polarization. As shown in the main draft, handling the possibility of Z_2 cancellation can be taken care of by modifying the product $\chi_a g_a$ for certain nodes. This could, in general, give rise to a modified K-matrix, but after that the rest of the formulation would go through. Additionally, since this formalism was derived from independent continuum flavors of Dirac fermions, it may be necessary to modify the sign of certain response coefficients to match the lattice results. Such a sign may be present, for example, for the charge polarization. We called this extra factor Θ in the main text. We will leave a full discussion of these issues to future work.

Appendix B

Appendix for 3D line-node semimetal

B.1 Multiple FLs and the polarization

When we have multiple FLs, the problem of calculating the polarization precisely is not quite as simple because the boundary charge is decided by the overlap and filling of the low energy boundary states that are enclosed by the multiple FLs. Despite this, even in the most general setting, the polarization can be written down as a signed-sum of the various projected areas enclosed by the various FLs. As described in the main text, we showed that we can perform a simple bulk calculation to determine a set of values for these signs. However, a precise surface theorem giving the bound charge associated to the polarization change at an interface is meaningful only when the occupations of the surface states are specified (similar to the complications in [20, 78] for the polarizations in a Chern insulator or 2D Dirac semi-metal respectively). If the boundary occupations are precisely known, then one can determine the necessary sign for each area contribution that will determine the correct surface charge. Hence, the projected areas that determine the surface charge are decided by the geometry of the FLs, but the signs multiplying each area can differ from the bulk calculation, and depend explicitly on the boundary state occupation.

The results simplify when there is only one or two FLs in the system. In the former case, the surface charge is determined (up to a sign decided by the inversion-symmetry breaking) by whether the surface states exist inside or outside the FL. For two (or more) FLs another complication appears due to the possibility of the projected areas overlapping in the surface BZ. In these cases we can have edge states overlapping, and we expect generically that a $\mathbb{Z}_2$ cancelation will occur for the overlapping states. Now, let us show how we can determine the bulk value of the polarization precisely for the case of two line nodes. A natural guess for a generalization of the polarization formula we have derived in Eq. 5.6 would be

$$P^i = \epsilon^{ijk}(-1)^{\nu_{jk}} \sum_a \frac{e}{8\pi^2} \Xi_a \Omega_{a,jk}, \tag{B.1}$$

but this unfortunately does not account for the possible $\mathbb{Z}_2$ cancelations. To account for this we start off by

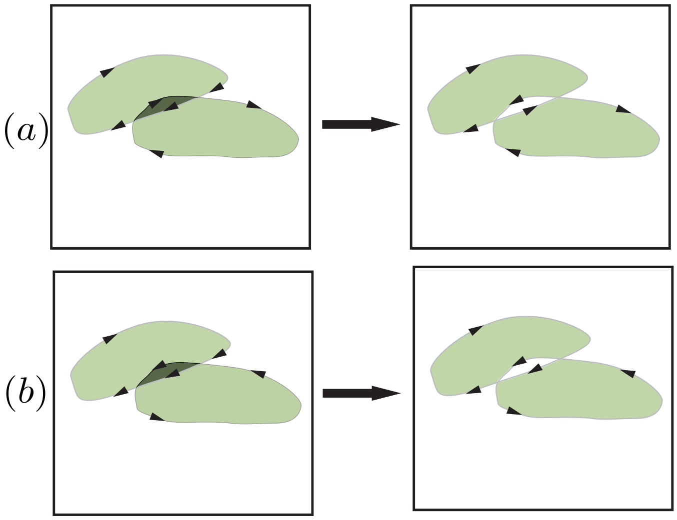

Figure B.1: Rules for the modification of $\chi\mathrm{sgn}\, m_{\mathcal{I}}$ for the determination of the boundary charge for the case of two FLs are illustrated. The green shaded areas represent regions where edge states exist, and the dark green area represents areas where there are overlapping edge states. Case (a) needs a reassignment of arrows while case (b) does not.

drawing the projected FLs in the appropriate surface BZ perpendicular to the polarization direction. We must take care to include arrows indicating the direction along which Berry flux is flowing along the FL with respect to the surface normal. The flow is clockwise when the product $\chi\mathrm{sgn}\, m_{\mathcal{I}} = +1$ and counterclockwise for the product $\chi\mathrm{sgn}\, m_{\mathcal{I}} = -1$ where χ corresponds to the FL helicity with respect to the normal along the ith direction. If there are some regions where the projected areas of the FLs overlap, we have to carefully handle the $\mathbb{Z}_2$ cancellation. We assume that any place where two FL areas overlap there is a cancellation. We can effectively take this into account in our formula after performing a simple graphical analysis. First, if the weak invariant $(-1)^{\nu_{ij}} = -1$, we start off by shading the region around (π, π), else we leave it unshaded. Then every time we cross a FL, we change from shaded to unshaded and vice versa. This prescription gives us a unique way of shading the entire surface BZ with the projected FLs where *alternating* regions are shaded. The shaded regions naturally represent regions of the surface BZ with stable surface states. After we are done with shading, we check if the regions which are shaded have an arrow consistently going clockwise/counterclockwise on its boundary. If they do, we sum over the areas of the regions shaded with the product $\chi\mathrm{sgn}\, m_{\mathcal{I}}$ for that region coming from the direction of the arrow on the boundary. If the direction of arrows is inconsistent, we follow the reassignment of the arrows as shown in Fig. B.1 and sum over the modified areas.

With more FLs, this prescription does not give us a unique answer in regions which have *more* than two sets of edge states overlapping. The sign of the polarization arising from these regions depends on the details of how the surface states are coupled to give the $\mathbb{Z}_2$ cancelation, and hence how the states are occupied. The value of the polarization that matches the surface charge is ultimately still a signed sum of the projected areas, but these signs can only be determined after the occupation of the edge state branches is chosen. All of these issues arise due to the $\mathbb{Z}_2$ stability of the edge states, as opposed to the $\mathbb{Z}$ stable chiral case. We will leave the problem of exhaustive treatment of generic FL configurations to future work.

B.2 $\mathcal{TI}$ symmetry and Berry curvatures

To prove the result about the properties of the Berry curvature for a line-node, we switch back to writing out the ket $|\alpha\rangle = u_{\alpha,\mathbf{k}}$ as a column vector with u^i_α being the ith component (the bras will be row vectors and we will use lowered indices for them). Let us consider the following matrix element $M = \mathrm{Im}\,\langle\partial_b\alpha_1|\alpha_2\rangle\langle\alpha_2|\partial_c\alpha_1\rangle = \mathrm{Im}\,(\partial_b u^*_{\alpha_1,i})u^i_{\alpha_2}u^*_{\alpha_2,j}(\partial_c u^j_{\alpha_1})$ and its transformation properties under $\mathcal{TI}$, where we assume that $\mathcal{TI} = UK$ with U being a constant unitary matrix. Repeated indices of i, j, k are assumed to be summed. The action of $\mathcal{TI}$ on the matrix element gives us the following:

$$\begin{aligned} M &= \mathrm{Im}\,((U^\dagger)^k_i\partial_b u_{\alpha_1,k})(U^i_r u^{r,*}_{\alpha_2})((U^\dagger)^s_j u_{\alpha_2,s})(U^j_p\partial_c u^{p,*}_{\alpha_1}) \\ &= \mathrm{Im}\,(\partial_b u_{\alpha_1,k})(u^{k,*}_{\alpha_2})(u_{\alpha_2,s})(\partial_c u^{s,*}_{\alpha_1}) \\ &= -\mathrm{Im}\,(\partial_b u^*_{\alpha_1,i})u^i_{\alpha_2}u^*_{\alpha_2,j}(\partial_c u^j_{\alpha_1}) \end{aligned} \tag{B.2}$$

where the asterisk denotes complex conjugation. We have summed over i, j when we go from the first to the second line to get rid of factors of U. The minus sign from the second to the third line comes from conjugation. Further, we have used the following symmetry properties of the Bloch states under $\mathcal{TI}$ given by:

$$u^i_\alpha = U^i_j u^j_\alpha,\ u^*_{\alpha,i} = (U^\dagger)^j_i u^*_{\alpha,j} \tag{B.3}$$

Put together, what we have proved is that $\mathrm{Im}\,\langle\partial_b\alpha_1|\alpha_2\rangle\langle\alpha_2|\partial_c\alpha_1\rangle = -\mathrm{Im}\,\langle\partial_b\alpha_1|\alpha_2\rangle\langle\alpha_2|\partial_c\alpha_1\rangle$ under $\mathcal{TI}$. We also note that $\mathrm{Im}\,\langle\partial_b\alpha_1|\alpha_2\rangle\langle\alpha_2|\partial_c\alpha_1\rangle = \mathcal{F}^{\alpha_1\alpha_1}_{bc,proj}$ is the Berry curvature of the α_1th band coming from the Hamiltonian $H_{12} = \epsilon_{\alpha_2}|\alpha_2\rangle\langle\alpha_2| + \epsilon_{\alpha_1}|\alpha_1\rangle\langle\alpha_1|$ (We call this the projected α_1, α_2 subsystem). What we have proved with our analysis of the matrix element under $\mathcal{TI}$ is that $\mathcal{F}^{\alpha_1\alpha_1}_{bc,proj} = -\mathcal{F}^{\alpha_1\alpha_1}_{bc,proj} \bmod 2\pi$. If the two bands do not cross, clearly the projected Berry curvature should be zero at every point in the BZ. If on the other hand, they do touch along stable FLs we can see that it must be equal to $\pi\Xi\delta(k - k_0)$ where k_0 is the location of the nodal line. The other identity which we use is that $\mathrm{Im}\,\langle\partial_b\alpha_1|\alpha_2\rangle\langle\alpha_2|\partial_c\alpha_1\rangle =$

$-\mathrm{Im}\,\langle \partial_b \alpha_2 | \alpha_1 \rangle \langle \alpha_1 | \partial_c \alpha_2 \rangle$, i.e. $\mathcal{F}^{\alpha_1\alpha_1}_{bc,proj} = -\mathcal{F}^{\alpha_2\alpha_2}_{bc,proj}$ in the projected system. This simply follows from the property that $\langle \alpha_2 | \partial_a \alpha_1 \rangle = -\langle \partial_a \alpha_2 | \alpha_1 \rangle$. Thus, we must have:

$$\begin{aligned} \mathrm{Im}\,\langle \partial_b \alpha_1 | \alpha_2 \rangle \langle \alpha_2 | \partial_c \alpha_1 \rangle &= \mathrm{Im}\,\langle \alpha_1 | \partial_b \alpha_2 \rangle \langle \partial_c \alpha_2 | \alpha_1 \rangle \\ &= \mathrm{Im}\,(\langle \partial_b \alpha_2 | \alpha_1 \rangle \langle \alpha_1 | \partial_c \alpha_2 \rangle)^* \\ &= -\mathrm{Im}\,\langle \partial_b \alpha_2 | \alpha_1 \rangle \langle \alpha_1 | \partial_c \alpha_2 \rangle \end{aligned} \tag{B.4}$$

as claimed.

B.3 Magnetization in a LTSM model

Let us now calculate the magnetization for our model, which will eventually give us insight into the generic form for all LTSMs. The calculation of the (orbital) magnetization in crystalline systems was developed in [85, 13], and the result of our calculation is essentially an extension of the results of the 2D Dirac semimetal shown in [105, 78]. To proceed, the adiabatic (Berry) curvatures $\mathcal{F}_{xy}, \mathcal{F}_{yz}, \mathcal{F}_{zx}$ for the following generic two-band model are calculated:

$$H(k) = A(\vec{k})\sigma^x + m_{\mathcal{I}}\sigma^y + B(\vec{k})\sigma^z \tag{B.5}$$

where $m_{\mathcal{I}}$ represents an infinitesimal inversion-breaking mass term that must be added to properly calculate the magnetization. Note that for the purposes of calculating the adiabatic curvatures, the additional $\epsilon(\vec{k})\mathbb{I}$ term that we will add to change the energy of the FL can be ignored since its inclusion will not affect the Bloch wavefunctions. The adiabatic curvature can be represented by defining the unit vector $\hat{d}$ as

$$\hat{d}(\vec{k}) = \frac{(A, m_{\mathcal{I}}, B)}{\sqrt{A^2 + m_{\mathcal{I}}^2 + B^2}} \tag{B.6}$$

which yields

$$\mathcal{F}_{ij} = \epsilon^{abc} \hat{d}_a \partial_i \hat{d}_b \partial_j \hat{d}_c \tag{B.7}$$

where $\partial_i = \frac{\partial}{\partial k_i}$ for $i = x, y, z$. So for the model in Eq. B.5 we have

$$\mathcal{F}_{ij} = m_{\mathcal{I}} \frac{\partial_i A\, \partial_j B - \partial_j A\, \partial_i B}{(A^2 + m_{\mathcal{I}}^2 + B^2)^{3/2}}. \tag{B.8}$$

For the case of the semimetal, the limit of $m_{\mathcal{I}} \to 0$ must be taken. Using the identity that $\lim_{\epsilon\to 0}\frac{\epsilon}{\epsilon^2+\alpha^2} = \pi\,\mathrm{sgn}\, m_{\mathcal{I}}\,\delta(\alpha)$, the curvature can be simplified to

$$\mathcal{F}_{ij} = \pi\,\mathrm{sgn}\, m_{\mathcal{I}}\delta(\sqrt{A^2+B^2})\frac{\partial_i A\,\partial_j B - \partial_j A\,\partial_i B}{\sqrt{A^2+B^2}}. \tag{B.9}$$

If we think about the actual terms $A(\vec{k})$ and $B(\vec{k})$ from the model H_3, then we quickly see that the δ-function only has non-zero support exactly on the line-nodes. Generically, when $A(\vec{k})$ and $B(\vec{k})$ both vanish, then the system is gapless (when $m_{\mathcal{I}} \to 0$), and these gapless regions are the only sources of adiabatic curvature for a system with $\mathcal{TI}$ symmetry. Thus, in the gapless, semimetallic limit the only adiabatic curvature in the BZ is localized exactly on the FL, which we know must be the case for a model with $\mathcal{TI}$ symmetry.

To finish the magnetization calculation, consider the model $\bar{H}_3(\vec{k}) = \epsilon(\vec{k})\mathbb{I} + H_3(\vec{k})$ which now has broken $\mathcal{T}$ and broken $\mathcal{I}$, but preserves $\mathcal{TI}$. The expression for the magnetization density in terms of Bloch bands is given by [13]

$$M^a = \epsilon^{abc}\frac{e}{2\hbar}\int\frac{d^3k}{(2\pi)^3}\mathrm{Im}\langle\partial_b u_-|(\bar{H}_3(k) + E_-(k))|\partial_c u_-\rangle \tag{B.10}$$

where $E_-(k), |u_-\rangle$ are the energy and Bloch functions of the lower occupied band, and the derivatives are with respect to momentum. From symmetry, and from the fact that the extra kinetic term is proportional to the identity matrix, the above expression simplifies to

$$M^a = \mathrm{sgn}\, m_{\mathcal{I}}\frac{e\epsilon^{abc}}{4\hbar}\int_{BZ}\frac{d^3k}{(2\pi)^3}2\epsilon(\vec{k})\mathcal{F}_{bc}. \tag{B.11}$$

The expression from Eq. B.9 for the curvature can now be substituted. Notice that we can do a coordinate transformation under the integral from $(k_a, k_b, k_c) \to (k_a, A, B)$ and the Jacobian of the transformation $J = |\partial_i A\partial_j B - \partial_j A\partial_i B|$ is already sitting in the curvature up to a total sign. Using the property that $\int_{\mathbf{X}}\delta(g(x))f(g(x))|g'(x)|dx = \int_{g(\mathbf{X})}\delta(u)f(u)du$, we can rewrite Eq. B.11 as

$$M^a = \pm\,\mathrm{sgn}\, m_{\mathcal{I}}\frac{e}{4\hbar}\int\frac{dk^a dA dB}{(2\pi)^2}2\epsilon(\vec{k})\frac{\delta(\sqrt{A^2+B^2})}{\sqrt{A^2+B^2}} \tag{B.12}$$

where the domain of integration has now changed to the range of values which A, B take over the BZ and the outer signs represent the helicity of the FL, i.e. the sign of the Jacobian. We can make a coordinate transformation to polar coordinates in $A, B \to r, \theta$ where we note that r, θ could in general depend on k^a.

$$M^a = \pm\,\mathrm{sgn}\, m_{\mathcal{I}}\frac{e}{4\hbar}\int\frac{dk^a \times r dr d\theta}{(2\pi)^2}2\epsilon(\vec{k})\frac{\delta(r)}{r} \tag{B.13}$$

which can be simplified by integrating the expressions over r, θ. The δ function localizes the integral to the FL and the integral over θ gives us a factor of 2π.

$$\vec{M} = \pm \operatorname{sgn} m_{\mathcal{I}} \frac{e}{4\pi\hbar} \int_{\partial R} \epsilon(\vec{k}) d\vec{k} \tag{B.14}$$

where we have explicitly indicated that the integration in Eq. B.14 is over the FL which is equivalent to ∂R. We note that the magnetization results from integrating the energy of each point on the FL along the line node. Again, the ± sign in front of the magnetization tells us the sense in which the Berry flux circulates along the string, i.e., clockwise or counter-clockwise. This is a simple derivation of the bulk magnetization in the case of a single line node. If there are multiple FLs, contributions to the magnetization from each FL using Eq. B.14 must be added up, but the result is not as complicated as the polarization with multiple FLs since the magnetization adds up normally, not as a Z_2 quantity. It is important to note that the connection between the bulk magnetization calculation and the boundary current can depend on the details of how the boundary states are filled similar to what was shown in [78] for 2D Dirac semi-metals.

Appendix C

Appendix for 3D topological crystalline insulator

C.1 Diagrammatic calculation of response

In this section we provide a direct diagrammatic calculation for the response in the main text. We begin with the continuum version of the Hamiltonian for a TCI described in Chapter 6,

$$H_{\mathrm{TCI}} = k_x\Gamma^x + (k_y + b_y\sigma^y)\Gamma^y + k_z\Gamma^z + m'\cos\Theta\Gamma^0 + m'\sin\Theta\sigma^y\Gamma^5, \tag{C.1}$$

where tensor products are implicit and σ^0's have been omitted. The relevant diagrams that need to be calculated are shown in Fig. C.1.

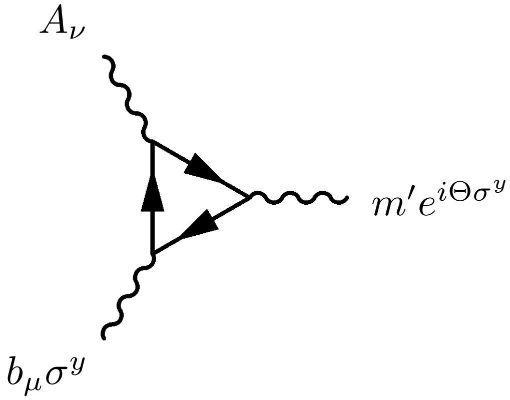

Figure C.1: Relevant Feynman diagrams for the effective action indicated in Eq. (C.3).

The two diagrams are equal due to symmetry and contribute an extra factor of 2. Evaluating the diagrams as in [10], we find:

$$S[A,b] = -2\times\int d^4x\frac{e^2}{16\pi^2}\epsilon^{\mu\nu\rho\sigma}\mathrm{Tr}_\sigma\left[\partial_\mu(\Theta\sigma^y)(b_\nu\sigma^y)\partial_\rho A_\sigma\right] \tag{C.2}$$

After tracing over σ and integrating by parts, we obtain

$$S[A,b] = \frac{e}{8\pi^2}\int d^4x\,\Theta(x)\,\epsilon^{\mu\nu\rho\sigma} f_{\mu\nu}F_{\rho\sigma}, \tag{C.3}$$

which is the response quoted in the main text.

C.2 Stability of the surface Dirac nodes for $\mathcal{C}_M = 2$

In this section, we show that for a mTCI with mirror symmetry (say along z direction, $\mathcal{M}_z$) and time-reversal symmetry ($\mathcal{T}$), the stability of the surface Dirac nodes is related to $\mathcal{C}_M$. Particularly, we prove that for the case of $\mathcal{C}_M = 2$, there are two stable Dirac nodes on *all* mirror symmetric surfaces. Upon including proper mirror-breaking mass terms and a defect in the b field, the TCI response we postulate can be obtained.

Our discussion begins with a heuristic analysis of a TCI that consists of two blocks of a strong TI that has inversion symmetry $\mathcal{I}$ in addition to time-reversal and mirror symmetry. Each copy contributes $\mathcal{C}_M = 1$ to the mirror Chern number. In the presence of inversion symmetry, the mirror Chern number for each of the TI copies $\mathcal{C}_M$ can be directly related to the mirror chirality η defined [91] at TR invariant points on the mirror planes. Using the mirror chirality, we show that for all cases where $\mathcal{C}_M = 2$, the TCI supports two stable surface Dirac nodes.

In the second section, we provide a more general proof that for *all* cases with $\mathcal{M}_z$ and $\mathcal{T}$, $\mathcal{C}_M = 2$ necessarily indicates two stable Dirac cones on the surfaces. All of these arguments are a slightly expanded version of what is present in [91].

C.3 TCI from two strong TI's

Let us consider our 3D lattice model for a TCI which consists of two blocks of the usual 3D strong TI. The model for the 3D TI is

$$H_{TI} = v_x \sin k_x \Gamma^x + v_y \sin k_y \Gamma^y + v_z \sin k_z \Gamma^z - (M + \cos k_x + \cos k_y + \cos k_z)\Gamma^0 \tag{C.4}$$

where $\Gamma^x = \tau^y \otimes \mathbb{I}, \Gamma^y = \tau^z \otimes s^x, \Gamma^z = \tau^z \otimes s^z, \Gamma^0 = \tau^x \otimes \mathbb{I}$ and $\Gamma^5 = \tau^z \otimes s^y$. The mirror operators are $\mathcal{M}_i = \Gamma^5\Gamma^i$ which satisfy $\mathcal{M}_i^2 = -1$. In particular $\mathcal{M}_z = i\mathbb{I} \otimes s^x$.

Given this model we can construct a TCI Hamiltonian by taking two blocks of H_{TI}, although we will see that it is important to consider generic velocities in each block. To simplify the analysis, we will choose each velocity v_i for both blocks to be proportional to a positive constant v which we will set to 1 for convenience. Then each velocity parameter represents just the sign of the velocity, i.e., $v_i = \pm 1$. Given a choice of mirror operator we can define the mirror chirality of the $k \cdot P$ Hamiltonians around each time-reversal invariant momentum. For our simple model, if we choose mirror operator $\mathcal{M}_i$ then the mirror chirality for each 4×4 Dirac block is

$$\chi_M = \mathrm{sgn}(v_j v_k), \tag{C.5}$$

where $i \neq j \neq k$ as derived in [91].

At this point, we concern ourselves with the mirror symmetry $\mathcal{M}_z$ and consider surface Hamiltonians perpendicular to $\hat{x}, \hat{y}$. For H_{TI} if we choose $M = 0$ the bands at Γ are inverted and will lead to surface states. For a surface with normal vector $\hat{x}$ we find the surface Hamiltonian

$$H_{\mathrm{surf},x} = (\mathrm{sgn} v_x)(v_y \sin k_y s^x + v_z \sin k_z s^z) \tag{C.6}$$

and the mirror operator projects to is^x on the surface. Note that the dependence on the sign of v_x arises from the bound state condition where that sign chooses which eigenvalue of $\Gamma^x \Gamma^0$ corresponds to which surface. If we switch the sign then the bound state on the $+\hat{x}$ surface corresponds to the opposite eigenvalue and the projected surface matrices each pick up a negative sign.

For the $+\hat{y}$ direction we have

$$H_{\mathrm{surf},y} = (\mathrm{sgn} v_y)(v_x \sin k_x s^z + v_z \sin k_z s^x) \tag{C.7}$$

and, importantly, the mirror operator projects to is^z on this surface. Both of these surface Hamiltonians are protected as long as mirror symmetry is preserved.

Now if we add a second block to represent a TCI we have some choices of velocity signs. In fact, we have a sign choice for each velocity. There are $2^3 = 8$ choices, but, they only give rise to four distinct Hamiltonians as far as the stability analysis is concerned. These are:

$$H_{\mathrm{surf},x,1} = \sin k_y \mathbb{I} \otimes s^x + \sin k_z \mathbb{I} \otimes s^z \tag{C.8}$$

$$H_{\mathrm{surf},x,2} = \sin k_y \mathbb{I} \otimes s^x + \sin k_z \mu^z \otimes s^z \tag{C.9}$$

$$H_{\mathrm{surf},x,3} = \sin k_y \mu^z \otimes s^x + \sin k_z \mathbb{I} \otimes s^z \tag{C.10}$$

$$H_{\mathrm{surf},x,4} = \sin k_y \mu^z \otimes s^x + \sin k_z \mu^z \otimes s^z \tag{C.11}$$

and the other four differ from these by a global sign multiplying the full Hamiltonian. In cases $H_{\mathrm{surf},x,3}$ and $H_{\mathrm{surf},x,4}$ we can find mass terms which preserve $\mathcal{M}_z$, e.g. $\mu^x \otimes s^x$ and $\mu^x \otimes \mathbb{I}$ respectively.

We can do something similar for the other surface type

$$\begin{aligned} H_{\mathrm{surf},y,1} &= \sin k_x \mathbb{I} \otimes s^z + \sin k_z \mathbb{I} \otimes s^x && \text{(C.12)} \\ H_{\mathrm{surf},y,2} &= \sin k_x \mathbb{I} \otimes s^z + \sin k_z \mu^z \otimes s^x && \text{(C.13)} \\ H_{\mathrm{surf},y,3} &= \sin k_x \mu^z \otimes s^z + \sin k_z \mathbb{I} \otimes s^x && \text{(C.14)} \\ H_{\mathrm{surf},y,4} &= \sin k_x \mu^z \otimes s^z + \sin k_z \mu^z \otimes s^x. && \text{(C.15)} \end{aligned}$$

In this case as well, the last two Hamiltonians are unstable even when mirror is preserved.

Interestingly, we see that the two Dirac nodes in $H_{\mathrm{surf},x/y,3}$ have the opposite helicity, but those in $H_{\mathrm{surf},x/y,4}$ have the same helicity, and yet they can be gapped in either case. Hence, the helicity is not what we should be using to characterize the surface states. However, one can easily check that if the *mirror chirality* χ between the blocks are the same (different), then the resulting surface states are stable (unstable). As shown in Teo, Fu, and Kane [91], the mirror chirality determines the sign of the *change* in mirror Chern number when there is a band inversion. Thus, we can correlate the cases with stable surface states as having $\mathcal{C}_M = \pm 2$ and in the unstable cases $\mathcal{C}_M = 0$.

Let us look at another example. Consider $H_{\mathrm{surf},x,1}$ and $H_{\mathrm{surf},x,3}$ and turn on the b_y shift generated by $b_y \mu^y \otimes \Gamma^y$ in the bulk Hamiltonian. We immediately find that this perturbation shifts the Dirac nodes in $H_{\mathrm{surf},x,1}$ but gaps the Dirac nodes in $H_{\mathrm{surf},x,3}$. Hence, if we have a domain wall in b_y, this term will gap out the Dirac nodes in $H_{\mathrm{surf},x,3}$ instead of shifting them. We can see that it is crucial to have the μ^z term in the surface Hamiltonian which will anti-commute with the μ^y term in the shift. We could have also chosen to shift with μ^x but the same result applies.

C.4 General proof

Let us consider a system with mirror symmetry along z direction ($\mathcal{M}_z$) and time reversal symmetry ($\mathcal{T}$), characterized by a mirror Chern number

$$\mathcal{C}_M \equiv C_M(k_z = 0) + C_M(k_z = \pi) = 2, \tag{C.16}$$

where $k_z = 0$ and $k_z = \pi$ are two invariant momenta under mirror symmetry. We claim that there necessarily exist two Dirac cones on a x-surface that are protected by $\mathcal{M}_z$.

Before we start, we note that due to $\mathcal{M}_z$ symmetry, Dirac cones located at $k_z \neq 0, \pi$ always appear in pairs with opposite k_z values. These Dirac cones can generically gap out each other when translational symmetry along z is broken, i.e., at the domain wall of $m_A(z)$ we consider in the main text. Therefore, such Dirac cones do not have nontrivial contribution to the topological response we consider, and we will focus only at $k_z = 0, \pi$ planes.

At $k_z = 0, \pi$, $\mathcal{M}_z$ is a good quantum number, and we can divide this 2D system into two subsystem with $\mathcal{M}_z = \pm i$. From the definition $\mathcal{C}_M = (\mathcal{C}_i - \mathcal{C}_{-i})/2$ and by time-reversal symmetry, we have $\mathcal{C}_i = 2$ and $\mathcal{C}_{-i} = -2$.

The fact that $\mathcal{C}_i = 2$ indicates two chiral modes in the $+i$ sector at the edge of the xy plane with at $k_z = 0$ and/or $k_z = \pi$. Hence at an x-surface, to linear order,

$$H_{i,k_z=0,\pi} = v_y k_y \mu^0, \tag{C.17}$$

where μ^0 is a 2-by-2 matrix corresponding to the two edge modes. In principle there is nothing enforcing the v_y's to be the same for the two chiral modes, but they should have the same sign. Generally, it can be shown that a different magnitude of $|v_y|$'s would lead to no change to the final conclusion.

On the other hand, $C_{-i} = -2$ also indicates two edge modes in the $-i$ sector that are related to $+i$ sector by time-reversal symmetry, hence $H_{-i,k_z=0,\pi} = -v_y k_y \mu^0$. Combining $\pm i$ sectors,

$$H_{k_z=0,\pi} = v_y k_y s^x \otimes \mu^0, \tag{C.18}$$

where we define $s^x = \pm 1$ for $\mathcal{M}_z = \pm i$. Thus, in the subspace of the four surface bands, the form of the mirror operators is given by $\mathcal{M}_z = i s^x \otimes \mu^0$.

We can now introduce the k_z dependence back. Other than a constant term, mirror symmetry $\mathcal{M}_z$ enforces that the only allowed terms are of the form $\sim v_z k_z s^{y,z} \otimes \mu^{0,1,2,3}$. In general the 2D Hamiltonian at the x-surface is

$$H_{yz} = v_y k_y s^x \otimes \mu^0 + v_z k_z \Pi_z, \tag{C.19}$$

where $\{\mathcal{M}_z, \Pi_z\} = 0$ which arises from the fact that $\mathcal{M}_z H_{yz}(k_y, k_z) \mathcal{M}_z^{-1} = H(k_y, -k_z)$ due to mirror symmetry. This Hamiltonian corresponds to two Dirac cones.[1] *Any* gapping term necessarily involves $s^{y,z}$, which is forbidden by $\mathcal{M}_z$.

---

[1] Due to the anti-commutation with $\mathcal{M}_z$, the four eigenvalues of Π_z are necessarily of the form $(+a, -a, +b, -b)$, where the two states with $\Pi_z|\alpha\rangle = a|\alpha\rangle$ and $\Pi_z|-\alpha\rangle = -a|-\alpha\rangle$ are related by $|-\alpha\rangle = -i\mathcal{M}_z|\alpha\rangle$. In each block, say the one with eigenvalues $\pm a$, Π_z projects to $a\sigma^z$ and $s^x \otimes \mu^0 \equiv -i\mathcal{M}_z$ projects to σ^x. The reduced Hamiltonian in that block is $H = v_y k_y \sigma^x + a v_z k_z \sigma^z$, hence the Dirac cone.

C.5 Microscopic origin of the response

C.5.1 Surface states of a TCI

We derive the surface Dirac states from the explicit tight binding model for the TCI. We start with the lattice model used in the main text with b_y turned on:

$$H_{TCI}[\mathbf{k},\theta] = \sin k_x\Gamma^x + (\sin k_y + b_y\sigma^y)\Gamma^y + \sin k_z\Gamma^z - (m + c\cos k_x + c\cos k_y + c\cos k_z + c\cos\theta)\Gamma^0 + \sin\theta\,\Gamma^5 \tag{C.20}$$

where c is a constant that we set to 1 and $\theta = \pi$ is the adiabatic parameter field. Let us remind ourselves of the Dirac Γ matrix basis that we choose:

$$\Gamma^0 = \tau^x s^0,\ \Gamma^x = \tau^y s^0,\ \Gamma^y = \tau^z s^x,\ \Gamma^z = \tau^z s^z,\ \Gamma^5 = \tau^z s^y. \tag{C.21}$$

We solve for the states bound at the two yz surfaces perpendicular to the x direction. Let us first consider the TCI Hamiltonian (C.20) without the terms involving Γ^y, Γ^z, and solve for the *zero energy* eigenstates. Since the x-direction is no longer periodic in this case, we explicitly return to real space in x direction. The reduced Hamiltonian is

$$H_1 = \sum_{x=1}^{N-1}\left[\frac{i}{2}\Gamma^x(c^\dagger_{x+1}c_x - c^\dagger_x c_{x+1}) + \frac{1}{2}\Gamma^0(c^\dagger_{x+1}c_x + c^\dagger_x c_{x+1})\right] - \sum_{x=1}^{N}(m - 1 + \cos k_y + \cos k_z)\Gamma^0 c^\dagger_x c_x, \tag{C.22}$$

where we have suppressed the k_y and k_z indices in c_x operators. We use the ansatz

$$|\Phi\rangle = \sum_{x'=1}^{N}\lambda^{x'}c^\dagger_{x'}|0\rangle \tag{C.23}$$

for the wave function. Substituting this ansatz for the edge state, we have:

$$\begin{aligned}\Gamma^0 H|\Phi\rangle = &\left[\frac{i}{2}\Gamma^0\Gamma^x\left(\frac{1}{\lambda} - \lambda\right) + \frac{1}{2}\left(\frac{1}{\lambda} + \lambda\right) - (m - 1 + \cos k_y + \cos k_z)\right]|\Phi\rangle \\ &- \frac{i}{2}\Gamma^0\Gamma^x(c^\dagger_1 - \lambda^{N+1}c^\dagger_N)|0\rangle - \frac{1}{2}(c^\dagger_1 + \lambda^{N+1}c^\dagger_N)|0\rangle = 0.\end{aligned} \tag{C.24}$$

We can take $i\Gamma^0\Gamma^x = -\tau^z = \pm 1$, and then the first line reduces to an algebraic equation. However, we need to be careful about the two end terms at $x = 1$ and $x = N$ in the second line. For the state with $i\Gamma^0\Gamma^x = -1$, i.e. $\tau^z = 1$, $c^\dagger_1$ cancels out, and $c^\dagger_N$ term can only be neglected if $|\lambda| < 1$. For the same reason if $i\Gamma^0\Gamma^x = 1$, i.e. $\tau^z = -1$, we need to impose $|\lambda| > 1$. Therefore $\tau^z = 1$ corresponds to the "left" yz surface of the TCI and $\tau^z = -1$ corresponds to the "right" yz TCI surface. Solving for the first line of Eq. (C.24) with $\tau^z = -i\Gamma^0\Gamma^x = \pm 1$ we find $\lambda = (m - 1 + \cos k_y + \cos k_z)^{\pm 1}$. It is easy to see that, for both surface states corresponding to $\tau^z = \pm 1$, it is required that

$$|m - 1 + \cos k_y + \cos k_z| < 1. \tag{C.25}$$

We can now put back the $\Gamma^y = \tau^z s^x$ and $\Gamma^z = \tau^z s^z$ terms, namely,

$$H_2 = (\sin k_y + b_y \sigma^y)\Gamma^y + \sin k_z \Gamma^z \tag{C.26}$$

into the TCI Hamiltonian. Since τ^z commutes with both Gamma matrices, we can simply substitute it with the corresponding eigenvalue. Focusing on the right surface where $\tau^z = -1$, we obtain the surface dispersion

$$H_{2D}(k_y, k_z) = -(\sin k_y + b_y \sigma^y)s^x - \sin(k_z)s^z, \tag{C.27}$$

with $k_{y,z}$ satisfying $|m - 1 + \cos k_y + \cos k_z| < 1$. Eqs. (C.25) and (C.27) are Eqs. (11) and (10) in the main text.

For $-2 < m < 0$, the range (C.25) for k_y and k_z are centered around the Γ point. Particularly for $k_z = 0$ the range for k_y is given by

$$-\Lambda_m < k_y < \Lambda_m, \quad \Lambda_m = \arccos(-1 - m). \tag{C.28}$$

For simplicity, throughout the rest of the Supplemental Material we focus on this case. However, we have verified that our final conclusion will hold for other values of m. For $2 < m < 4$ the range for k_y and k_z is centered around (π, π), and for $0 < m < 2$ the range for k_y and k_z is centered around $(\pi, 0)$ and $(0, \pi)$; our analysis around $(0, 0)$ point can be easily carried over to these cases.

In general the 2D Hamiltonian in (C.27) describes the surface Dirac nodes of the TCI. For a small b_y, the Dirac nodes are simply shifted from Γ point. However, a larger b_y can either shift the original Dirac nodes outside the validity range, or introduce additional Dirac nodes with opposite helicities compared to original ones and then annihilate them. In both cases the transition happens when a Dirac node is at the upper limit of the range (C.28), i.e. $k_y = \pm\Lambda_m$. This corresponds to

$$|b_y^{cr}| = \sin(\Lambda_m), \tag{C.29}$$

and for $-2 < m < 0$ we have $|b_y^{cr}| = \sqrt{-m(m+2)}$.

C.5.2 Domain wall states on the surface of TCI

In this section we analyze the surface states of the TCI bound at domain walls of b_y in the z-direction. The domain walls we consider are mirror symmetric, given by

$$b_y(z) = \begin{cases} |b_y^0|, & z > z_0, \\ -|b_y^0|, & |z| < z_0 \\ |b_y^0|, & z < -z_0. \end{cases} \tag{C.30}$$

Since the two domain walls are spatially separated, it suffices to consider each of them separately. After a simple coordinate shift, we focus on a domain wall where $b_y(z) = |b_y^0|$ as $z \to \infty$ and $b_y(z) = -|b_y^0|$ as $z \to -\infty$. To do this the most intuitive way would be start from the surface Dirac Hamiltonian (C.27), and replace b_y with $b_y(z)$ and k_z with $-i\partial_z$. However, with this method the role of the momentum range of the surface states (C.25) would become unclear. In this section we instead directly solve for the domain wall bound state from the bulk Hamiltonian. The derivation follows similar procedures as in the previous section.

Similar to the previous Section, we split the TCI Hamiltonian into two parts, $H_{TCI} = H_1 + H_2$, where H_1 and H_2 are defined similarly as in the previous section, only with the z-direction expressed in real space. Explicitly, we have:

$$\begin{aligned} H_1 = \sum_{x,k_y,z} \Big[& \frac{i}{2}\Gamma^x (c^\dagger_{x+1,k_y,z} c_{x,k_y,z} - c^\dagger_{x,k_y,z} c_{x+1,k_y,z}) + \frac{1}{2}\Gamma^0 (c^\dagger_{x+1,k_y,z} c_{x,k_y,z} + c^\dagger_{x,k_y,z} c_{x+1,k_y,z}) \\ & -(m-1+\cos k_y)\Gamma^0 c^\dagger_{x,k_y,z} c_{x,k_y,z} - \frac{1}{2}\Gamma^0 (c^\dagger_{x,k_y,z+1} c_{x,k_y,z} + c^\dagger_{x,k_y,z} c_{x,k_y,z+1}), \Big] \\ H_2 = \sum_{x,k_y,z} \Big[& \sin(k_y + b_y(z)\sigma^y)\Gamma^y c^\dagger_{x,k_y,z} c_{x,k_y,z} + \frac{i}{2}\Gamma^z (c^\dagger_{x,k_y,z+1} c_{x,k_y,z} - c^\dagger_{x,k_y,z} c_{x,k_y,z+1}) + m_A \sigma^y \Gamma^5 c^\dagger_{x,k_y,z} c_{x,k_y,z} \Big], \end{aligned} \tag{C.31}$$

where we have added a small mirror symmetry breaking mass m_A to H_2. We use the ansatz for the domain wall state given by

$$|\Phi(k_y)\rangle = \sum_{x,k_y,z=1}^{N} \lambda(z)^x \exp^{-\sum_{z'=1}^{z} f(z')} c^\dagger_{x,k_y,k_y,z} |0\rangle, \tag{C.32}$$

where $f(z)$ is a function that we will relate to $b_y(z)$ later. We emphasize that, this ansatz describes a bound state *only* if $\lambda(z) \neq 1$, *and* the function $f(z)$ goes through zero with a *positive* slope.

We use the ansatz to solve for a zero energy state of H_1. Similar to the first line of Eq. (C.24), we have for the zero energy solution

$$\begin{aligned}
&\frac{i}{2}\Gamma^0\Gamma^x\left[\frac{1}{\lambda(z)}-\lambda(z)\right]+\frac{1}{2}\left[\frac{1}{\lambda(z)}+\lambda(z)\right]-\left[m-1+\cos k_y+\frac{\exp[f(z+1)]+\exp[-f(z-1)]}{2}\right]\\
\approx&\frac{i}{2}\Gamma^0\Gamma^x\left[\frac{1}{\lambda(z)}-\lambda(z)\right]+\frac{1}{2}\left[\frac{1}{\lambda(z)}+\lambda(z)\right]-[m-1+\cos k_y+\cosh f(z)]=0. \qquad \text{(C.33)}
\end{aligned}$$

where in the second step we have assumed that $f(z)$ is a slow varying function. Just like the case of the surface state, for this equation to make sense the condition is that for $i\Gamma^0\Gamma^x=-\tau^z=\pm 1$, $|\lambda(z)|\gtrless 1$. Substituting this into the solution of Eq. (C.33),

$$|m-1+\cos k_y+\cosh f(z)|<1. \qquad \text{(C.34)}$$

We still need to determine the form of $f(z)$. This can be done by solving for eigenstates of H_2, which involves Γ^y and Γ^z. We have for $\tau^z=-1$

$$H_2=-[\sin k_y+b_y(z)\sigma^y]s^x-i\sinh f(z)s^z-m_A s^y\sigma^y. \qquad \text{(C.35)}$$

This Hamiltonian is solved by

$$f(z)=-\sinh^{-1}\{[\sin k_y\sigma^y+b_y(z)]s^y\sigma^y\},\ \sigma^y s^y=-1, \qquad \text{(C.36)}$$

where $\sinh^{-1}$ is meant to act separately on each eigenstate of σ^y and s^y. In order for this to be a bound state, the slope of $f(z)$ has to be positive, which enforces $s^y\sigma^y=-1$. Therefore, the energy of this state is $E=m_A$. The function $f(z)$ goes through zero where $\sin k_y\sigma^y+b_y(z)=0$, and therefore there are two bound states localized at $z=\pm z_0$, where $\sin k_y=b_y(z_0)$ and the ± corresponds to the two eigenvalues of σ^y. The doubling of the bound states corresponds to the fact that our particular TCI model are composed of two copies of the TI.

Eq. (C.34) becomes

$$\left|m-1+\cos k_y+\sqrt{1+[\sin k_y\sigma^y+b_y(z)]^2}\right|<1. \qquad \text{(C.37)}$$

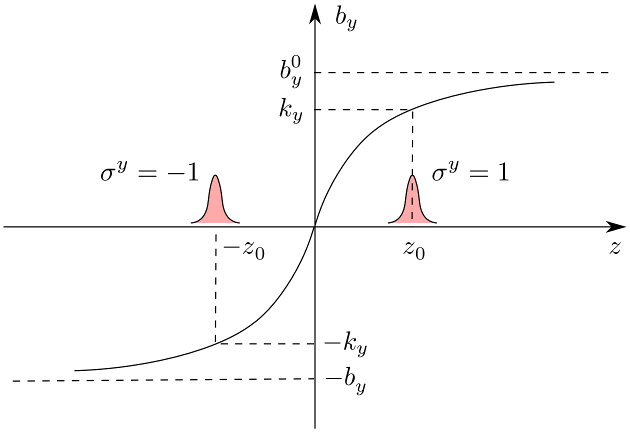

Figure C.2: The two zero-energy bound states at a given momentum k_y localized at the domain wall in b_y along z direction, each corresponding to $\sigma^y = \pm 1$.

For the bound state in $z \sim \pm z^0$, one can safely rewrite Eq. (C.37) as

$$|m + \cos k_y| < 1. \tag{C.38}$$

Note that, Eq. (C.38) is identical to the condition on the range of the surface state at $k_z = 0$. For $-2 < m < 0$, this range is centered around $k_y = 0$ and has the form $-\Lambda_m < k_y < \Lambda_m$.

C.5.3 Charge density from the domain wall bound states

In the continuum limit, we can linearize Eq. (C.36) and neglect the upper cutoff on k_y. We take $f(z) = k_y + b_y(z)\sigma^y$, and from the ansatz (C.32) one can easily make sure this corresponds to two bound states localized at $z = \pm z_0$ for $\sigma^y = \pm 1$, with z_0 given by $b_y(z_0) = k_y$. We illustrate this in Fig. C.2 for a given k_y. Each bound state contributes a charge $-e/2\text{sgn}(m_A)$. On the other hand, for a domain wall across which b_y changes from $-|b_y^0|$ to $|b_y^0|$, the total number of such bound states is $2 \times |b_y^0| L_y/\pi$, where L_y is the system size in the y-direction. Therefore, the total charge density bound at the domain wall of b_y around $z = 0$ is $-e|b_y^0|\text{sgn}(m_A)/\pi$. This agrees with the result from the analytical response.

On the other hand, for a domain wall of b_y with a larger "height", whether the ansatz (C.32) correponds to a bound state on the surface is more tricky. "Inside" the domain wall, $b_y = b_y(z)$ smoothly extrapolates from $-|b_y^0|$ to $|b_y^0|$. At an intermediate position $z = z_1$, if $b_y(z_1)$ is sufficiently large, there can be two possible situations. Within the range $-\Lambda_m < k_y < \Lambda_m$, the equation $f(z_1) = \sin k_y + b_y(z_1)\sigma^y = 0$ can either have no solution, or have two solutions at which $f(z_1)$ has opposite slopes. In both cases, the ansatz (C.32) is not normalizable in z direction, and hence does not correspond to a bound state solution localized at this $z = z_1$.

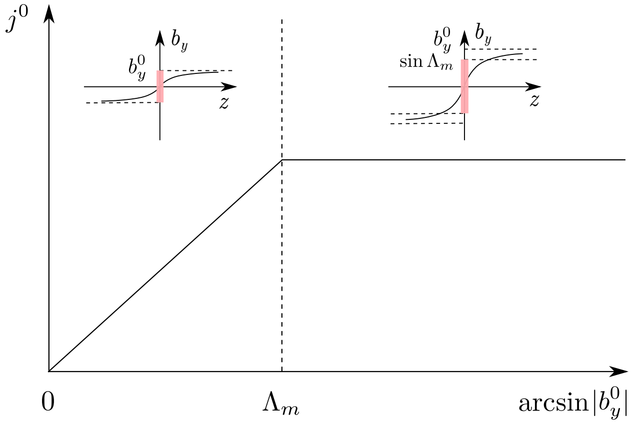

Figure C.3: Main figure: the charge density response j^0 at the surface domain wall of b_y as a function of the height of the domain wall. In the first region the response is consistent with the analytical result obtained from the effective action. Insets: The domain walls of b_y in z direction. The colored thick lines mark the intermediate $b_y(z_1)$ values that have bound states localized at $z = \pm z_1$.

Note that the two cases are closely related to the fate of the surface Dirac nodes discussed in Section II. Indeed, it is not difficult to see that the first case corresponds to when the surface Dirac nodes are eliminated within the range given by Eq. (C.25), and the second case corresponds to when additional Dirac nodes with opposite helicities to the original ones are introduced. In both cases, the topology of the bulk Hamiltonian changes. Therefore, we conclude that inside the domain wall, if an intermediate value $b_y(z_1)$ removes or cancels the surface Dirac nodes, there is *no* charge density bound at $z = z_1$. This occurs for

$$|b_y(z_1)| > |b_y^{cr}| = \sin\Lambda_m, \tag{C.39}$$

and we remember that for $-2 < m < 0$, $\sin\Lambda_m = \sqrt{-m(m+2)}$.

We can now obtain the generic charge density response as a function of the height of the domain wall $|b_y^0|$, which we plot in Fig. C.3. For a small $|b_y^0| < |b_y^{cr}| = \sin\Lambda_m$, everywhere inside the domain wall there exist surface bound states, with k_y ranging from $-\arcsin|b_y^0|$ to $\arcsin|b_y^0|$, leading to a charge density proportional to the corresponding momentum range $\arcsin|b_y^0|$, i.e.

$$j^0 = -\frac{e}{\pi}\arcsin|b_y^0|\mathrm{sgn}(m_A) \equiv -\frac{e}{\pi}|\tilde{b}_y^0|\mathrm{sgn}(m_A). \tag{C.40}$$

This response is universal, as it depends on universal numbers and a purely geometrical quantity $\tilde{b}_y^0 \equiv \arcsin|b_y^0|$, which is the magnitude of the *shift* of surface Dirac nodes on both sides of the domain wall. For $|b_y^0| > |b_y^{cr}| = \sin\Lambda_m$, however, only part of the domain wall interior traps bound states (see the second inset of Fig. C.3). The charge response is $j^0 = -e\mathrm{sgn}(m_A)/\pi \times \sin\Lambda_m$ and does not depend on b_y^0.

For a generic case given by a different m, or even a totally different lattice model, the value of $\sin\Lambda_m$ differs from our result. However, the behavior of the charge response remains the same, namely, the charge density first scales linearly with the height of the domain wall and then saturates at a critical value of $|b_y^0|$. This critical value of $|b_y^0|$ precisely corresponds to a change in the bulk topology, which leads to the elimination or cancellation of the surface Dirac nodes.

References

[1] A. Altland and M. R. Zirnbauer. Nonstandard symmetry classes in mesoscopic normal-superconducting hybrid structures. *Phys. Rev. B*, 55(2):1142, 1997.

[2] L. Balents and M. P. Fisher. Chiral surface states in the bulk quantum hall effect. *Phys. Rev. Lett.*, 76(15):2782, 1996.

[3] W. A. Benalcazar, J. C. Teo, and T. L. Hughes. Classification of two dimensional topological crystalline superconductors and majorana bound states at disclinations. *arXiv preprint arXiv:1311.0496*, 2013.

[4] B. A. Bernevig. *Topological Insulators and Topological Superconductors.* Princeton University Press, 2013.

[5] B. A. Bernevig. *Topological Insulators and Topological Superconductors.* Princeton University Press, 2013.

[6] B. A. Bernevig, T. L. Hughes, S. Raghu, and D. P. Arovas. Theory of the three-dimensional quantum hall effect in graphite. *Phys. Rev. Lett.*, 99(14):146804, 2007.

[7] B. A. Bernevig, T. L. Hughes, and S.-C. Zhang. Quantum spin hall effect and topological phase transition in hgte quantum wells. *Science*, 314(5806):1757–1761, 2006.

[8] G. Binnig and H. Rohrer. Scanning tunneling microscopy. *Surface science*, 126(1-3):236–244, 1983.

[9] A. A. Burkov, M. D. Hook, and L. Balents. Topological nodal semimetals. *Phys. Rev. B*, 84:235126, Dec 2011.

[10] C. G. Callan Jr and J. A. Harvey. Anomalies and fermion zero modes on strings and domain walls. *Nuclear Physics B*, 250(1):427–436, 1985.

[11] S. M. Carroll, G. B. Field, and R. Jackiw. Limits on a lorentz-and parity-violating modification of electrodynamics. *Physical Review D*, 41(4):1231, 1990.

[12] A. H. Castro Neto, F. Guinea, N. M. R. Peres, K. S. Novoselov, and A. K. Geim. The electronic properties of graphene. *Rev. Mod. Phys.*, 81:109–162, 2009.

[13] D. Ceresoli, T. Thonhauser, D. Vanderbilt, and R. Resta. Orbital magnetization in crystalline solids: Multi-band insulators, chern insulators, and metals. *Phys. Rev. B*, 74(2):024408, 2006.

[14] C.-Z. Chang, J. Zhang, X. Feng, J. Shen, Z. Zhang, M. Guo, K. Li, Y. Ou, P. Wei, L.-L. Wang, et al. Experimental observation of the quantum anomalous hall effect in a magnetic topological insulator. *Science*, 340(6129):167–170, 2013.

[15] Y. Chen, D. Bergman, and A. Burkov. Weyl fermions and the anomalous hall effect in metallic ferromagnets. *Phys. Rev. B*, 88(12):125110, 2013.

[16] Y. Chen, S. Wu, and A. Burkov. Axion response in weyl semimetals. *Phys. Rev. B*, 88(12):125105, 2013.

[17] M. N. Chernodub, A. Cortijo, A. G. Grushin, K. Landsteiner, and M. A. Vozmediano. A condensed matter realization of the axial magnetic effect. *arXiv preprint arXiv:1311.0878*, 2013.

[18] C.-K. Chiu, H. Yao, and S. Ryu. Classification of topological insulators and superconductors in the presence of reflection symmetry. *Phys. Rev. B*, 88(7):075142, 2013.

[19] G. Y. Cho, J. H. Bardarson, Y.-M. Lu, and J. E. Moore. Superconductivity of doped weyl semimetals: Finite-momentum pairing and electronic analog of the 3 he-a phase. *Phys. Rev. B*, 86(21):214514, 2012.

[20] S. Coh and D. Vanderbilt. Electric polarization in a chern insulator. *Phys. Rev. Lett.*, 102(10):107603, 2009.

[21] M. Creutz. Aspects of chiral symmetry and the lattice. *Rev. Mod. Phys.*, 73:119–150, Jan 2001.

[22] M. Drüppel, P. Krüger, and M. Rohlfing. Strain tuning of dirac states at the snte (001) surface. *Phys. Rev. B*, 90:155312, Oct 2014.

[23] P. Dziawa, B. Kowalski, K. Dybko, R. Buczko, A. Szczerbakow, M. Szot, E. Łusakowska, T. Balasubramanian, B. M. Wojek, M. Berntsen, et al. Topological crystalline insulator states in pb1- xsnxse. *Nature materials*, 11(12):1023–1027, 2012.

[24] V. Dziom, A. Shuvaev, A. Pimenov, G. Astakhov, C. Ames, K. Bendias, J. Böttcher, G. Tkachov, E. Hankiewicz, C. Brüne, et al. Observation of the universal magnetoelectric effect in a 3d topological insulator. *arXiv:1603.05482*, 2016.

[25] A. M. Essin, J. E. Moore, and D. Vanderbilt. Magnetoelectric polarizability and axion electrodynamics in crystalline insulators. *Phys. Rev. Lett.*, 102(14):146805, 2009.

[26] C. Fang, Y. Chen, H.-Y. Kee, and L. Fu. Topological nodal line semimetals with and without spin-orbital coupling. *arXiv preprint arXiv:1506.03449*, 2015.

[27] C. Fang, M. J. Gilbert, and B. A. Bernevig. Bulk topological invariants in noninteracting point group symmetric insulators. *Phys. Rev. B*, 86(11):115112, 2012.

[28] C. Fang, M. J. Gilbert, and B. A. Bernevig. Entanglement spectrum classification of c n-invariant noninteracting topological insulators in two dimensions. *Phys. Rev. B*, 87(3):035119, 2013.

[29] L. Fu. Topological crystalline insulators. *Phys. Rev. Lett.*, 106(10):106802, 2011.

[30] L. Fu and C. L. Kane. Topological insulators with inversion symmetry. *Phys. Rev. B*, 76(4):045302, 2007.

[31] L. Fu, C. L. Kane, and E. J. Mele. Topological insulators in three dimensions. *Phys. Rev. Lett.*, 98(10):106803, 2007.

[32] L. Fu, C. L. Kane, and E. J. Mele. Topological insulators in three dimensions. *Phys. Rev. Lett.*, 98:106803, 2007.

[33] S. Ganeshan and S. D. Sarma. The optical lattice weyl semimetal. *arXiv preprint arXiv:1405.4866*, 2014.

[34] P. Goswami and S. Tewari. Axion field theory and anomalous non-dissipative transport properties of (3+ 1)-dimensional weyl semi-metals and lorentz violating spinor electrodynamics. *arXiv preprint arXiv:1210.6352*, 2012.

[35] A. G. Grushin. Consequences of a condensed matter realization of lorentz-violating qed in weyl semi-metals. *Physical Review D*, 86(4):045001, 2012.

[36] G. B. Halász and L. Balents. Time-reversal invariant realization of the weyl semimetal phase. *Phys. Rev. B*, 85(3):035103, 2012.

[37] F. Haldane. Model for a quantum hall effect without landau levels: Condensed-matter realization of theparity anomaly. *Phys. Rev. Lett.*, 61(18):2015–2018, 1988.

[38] F. Haldane. Attachment of surface" fermi arcs" to the bulk fermi surface:" fermi-level plumbing" in topological metals. *arXiv preprint arXiv:1401.0529*, 2014.

[39] F. D. M. Haldane. Berry curvature on the fermi surface: Anomalous hall effect as a topological fermi-liquid property. *Phys. Rev. Lett.*, 93:206602, Nov 2004.

[40] B. I. Halperin. Possible states for a three-dimensional electron gas in a strong magnetic field. *Japanese Journal of Applied Physics Supplement*, 26:1913–1919, 1987.

[41] M. Z. Hasan and C. L. Kane. Colloquium: topological insulators. *Rev. Mod. Phys.*, 82(4):3045, 2010.

[42] P. Hosur. Friedel oscillations due to fermi arcs in weyl semimetals. *Phys. Rev. B*, 86:195102, Nov 2012.

[43] P. Hosur and X. Qi. Recent developments in transport phenomena in weyl semimetals. *Comptes Rendus Physique*, 14(9):857–870, 2013.

[44] D. Hsieh, D. Qian, L. Wray, Y. Xia, Y. S. Hor, R. J. Cava, and M. Z. Hasan. A topological dirac insulator in a quantum spin hall phase. *Nature*, 452:970, 2008.

[45] T. H. Hsieh, H. Lin, J. Liu, W. Duan, A. Bansil, and L. Fu. Topological crystalline insulators in the snte material class. *Nat. Comm.*, 3:982, 2012.

[46] T. L. Hughes, R. G. Leigh, and O. Parrikar. Torsional anomalies, hall viscosity, and bulk-boundary correspondence in topological states. *Phys. Rev. D*, 88:025040, Jul 2013.

[47] T. L. Hughes, E. Prodan, and B. A. Bernevig. Inversion-symmetric topological insulators. *Phys. Rev. B*, 83(24):245132, 2011.

[48] T. L. Hughes, H. Yao, and X.-L. Qi. Majorana zero modes in dislocations of sr2ruo4. *arXiv:1303.1539*, 2013.

[49] R. Jackiw and S.-Y. Pi. Chern-simons modification of general relativity. *Phys. Rev. D*, 68:104012, Nov 2003.

[50] R. Jackiw and C. Rebbi. Solitons with fermion number 1/2. *Phys. Rev. D*, 13(12):3398, 1976.

[51] R. Jackiw and C. Rebbi. Vacuum periodicity in a yang-mills quantum theory. *Phys. Rev. Lett.*, 37:172–175, 1976.

[52] P. Jadaun, D. Xiao, Q. Niu, and S. K. Banerjee. Topological classification of crystalline insulators with space group symmetry. *Phys. Rev. B*, 88(8):085110, 2013.

[53] Z. Jian-Hui, J. Hua, N. Qian, and S. Jun-Ren. Topological invariants of metals and the related physical effects. *Chinese Physics Letters*, 30(2):027101, 2013.

[54] C. L. Kane and E. J. Mele. Quantum spin hall effect in graphene. *Phys. Rev. Lett.*, 95(22):226801, 2005.

[55] C. L. Kane and E. J. Mele. Z 2 topological order and the quantum spin hall effect. *Phys. Rev. Lett.*, 95(14):146802, 2005.

[56] R. King-Smith and D. Vanderbilt. Theory of polarization of crystalline solids. *Phys. Rev. B*, 47(3):1651, 1993.

[57] A. Kitaev. Periodic table for topological insulators and superconductors. *arXiv preprint arXiv:0901.2686*, 2009.

[58] M. König, H. Buhmann, L. W. Molenkamp, T. Hughes, C.-X. Liu, X.-L. Qi, and S.-C. Zhang. The quantum spin hall effect: theory and experiment. *Journal of the Physical Society of Japan*, 77(3), 2008.

[59] M. König, S. Wiedmann, C. Brüne, A. Roth, H. Buhmann, L. W. Molenkamp, X.-L. Qi, and S.-C. Zhang. Quantum spin hall insulator state in hgte quantum wells. *Science*, 318(5851):766–770, 2007.

[60] Z. Liu, B. Zhou, Z. Wang, H. Weng, D. Prabhakaran, S.-K. Mo, Y. Zhang, Z. Shen, Z. Fang, X. Dai, et al. Discovery of a three-dimensional topological dirac semimetal, na3bi. *arXiv preprint arXiv:1310.0391*, 2013.

[61] S. Matsuura, P.-Y. Chang, A. P. Schnyder, and S. Ryu. Protected boundary states in gapless topological phases. *New Journal of Physics*, 15(6):065001, 2013.

[62] T. Meng and L. Balents. Weyl superconductors. *Phys. Rev. B*, 86(5):054504, 2012.

[63] G. Montambaux and M. Kohmoto. Quantized hall effect in three dimensions. *Phys. Rev. B*, 41(16):11417, 1990.

[64] J. Moore. Topological insulators: The next generation. *Nat. Phys.*, 5(6):378–380, 2009.

[65] J. E. Moore and L. Balents. Topological invariants of time-reversal-invariant band structures. *Phys. Rev. B*, 75:121306(R), 2007.

[66] T. Morimoto and A. Furusaki. Topological classification with additional symmetries from clifford algebras. *Phys. Rev. B*, 88(12):125129, 2013.

[67] K. Mullen, B. Uchoa, and D. T. Glatzhofer. Dirac loops in carbon allotropes. *arXiv preprint arXiv:1408.5522*, 2014.

[68] M. Neupane, S. Xu, R. Sankar, N. Alidoust, G. Bian, C. Liu, I. Belopolski, T.-R. Chang, H.-T. Jeng, H. Lin, et al. Observation of a topological 3d dirac semimetal phase in high-mobility cd3as2 and related materials. *arXiv preprint arXiv:1309.7892*, 2013.

[69] H. B. Nielsen and M. Ninomiya. A no-go theorem for regularizing chiral fermions. *Physics Letters B*, 105(2):219–223, 1981.

[70] S. Parameswaran, T. Grover, D. Abanin, D. Pesin, and A. Vishwanath. Probing the chiral anomaly with nonlocal transport in weyl semimetals. *arXiv preprint arXiv:1306.1234*, 2013.

[71] M. Phillips and V. Aji. Tunable line node semimetals. *Physical Review B*, 90(11):115111, 2014.

[72] F. Pollmann, E. Berg, A. M. Turner, and M. Oshikawa. Symmetry protection of topological phases in one-dimensional quantum spin systems. *Phys. Rev. B*, 85(7):075125, 2012.

[73] X.-L. Qi, T. L. Hughes, S. Raghu, and S.-C. Zhang. Time-reversal-invariant topological superconductors and superfluids in two and three dimensions. *Phys. Rev. Lett.*, 102(18):187001, 2009.

[74] X.-L. Qi, T. L. Hughes, and S.-C. Zhang. Fractional charge and quantized current in the quantum spin hall state. *Nat. Phys.*, 4(4):273–276, 2008.

[75] X.-L. Qi, T. L. Hughes, and S.-C. Zhang. Topological field theory of time-reversal invariant insulators. *Phys. Rev. B*, 78(19):195424, 2008.

[76] X.-L. Qi, T. L. Hughes, and S.-C. Zhang. Topological field theory of time-reversal invariant insulators. *Phys. Rev. B*, 78(19):195424, 2008.

[77] S. T. Ramamurthy and T. L. Hughes. In preparation.

[78] S. T. Ramamurthy and T. L. Hughes. Patterns of electromagnetic response in topological semimetals. *Phys. Rev. B*, 92:085105, Aug 2015.

[79] Y. Ran, Y. Zhang, and A. Vishwanath. One-dimensional topologically protected modes in topological insulators with lattice dislocations. *Nature Physics*, 5(4):298–303, 2009.

[80] A. N. Redlich. Parity violation and gauge noninvariance of the effective gauge field action in three dimensions. *Physical Review D*, 29(10):2366, 1984.

[81] R. Roy. Topological phases and the quantum spin hall effect in three dimensions. *Phys. Rev. B*, 79:195322, 2009.

[82] A. P. Schnyder, S. Ryu, A. Furusaki, and A. W. Ludwig. Classification of topological insulators and superconductors in three spatial dimensions. *Phys. Rev. B*, 78(19):195125, 2008.

[83] G. W. Semenoff. Condensed-matter simulation of a three-dimensional anomaly. *Phys. Rev. Lett.*, 53:2449–2452, Dec 1984.

[84] P. Sessi, D. Di Sante, A. Szczerbakow, F. Glott, S. Wilfert, H. Schmidt, T. Bathon, P. Dziawa, M. Greiter, T. Neupert, G. Sangiovanni, T. Story, R. Thomale, and M. Bode. Robust spin-polarized midgap states at step edges of topological crystalline insulators. *Science*, 354(6317):1269–1273, 2016.

[85] J. Shi, G. Vignale, D. Xiao, and Q. Niu. Quantum theory of orbital magnetization and its generalization to interacting systems. *Physical review letters*, 99(19):197202, 2007.

[86] R.-J. Slager, A. Mesaros, V. Juričić, and J. Zaanen. The space group classification of topological band-insulators. *Nat. Phys.*, 9:98, 2012.

[87] R.-J. Slager, A. Mesaros, V. Juričić, and J. Zaanen. The space group classification of topological band-insulators. *Nature Physics*, 9(2):98–102, 2013.

[88] Y. Tanaka, Z. Ren, T. Sato, K. Nakayama, S. Souma, T. Takahashi, K. Segawa, and Y. Ando. Experimental realization of a topological crystalline insulator in snte. *Nat. Phys.*, 8(11):800–803, 2012.

[89] E. Tang and L. Fu. Strain-induced partially flat band, helical snake states and interface superconductivity in topological crystalline insulators. *Nature Physics*, 10(12):964–969, 2014.

[90] J. C. Teo and T. L. Hughes. Existence of majorana-fermion bound states on disclinations and the classification of topological crystalline superconductors in two dimensions. *Phys. Rev. Lett.*, 111(4):047006, 2013.

[91] J. C. Y. Teo, L. Fu, and C. L. Kane. Surface states and topological invariants in three-dimensional topological insulators: Application to bi1xsbx. *Phys. Rev. B*, 78:045426, 2008.

[92] D. Thouless. Quantization of particle transport. *Phys. Rev. B*, 27(10):6083, 1983.

[93] A. M. Turner, A. Vishwanath, and C. O. Head. Beyond band insulators: Topology of semi-metals and interacting phases. *Topological Insulators*, 6:293, 2013.

[94] A. M. Turner, Y. Zhang, R. S. Mong, and A. Vishwanath. Quantized response and topology of magnetic insulators with inversion symmetry. *Physical Review B*, 85(16):165120, 2012.

[95] Y. Ueno, A. Yamakage, Y. Tanaka, and M. Sato. Symmetry-protected majorana fermions in topological crystalline superconductors: Theory and application to Sr_2RuO_4. *Phys. Rev. Lett.*, 111:087002, Aug 2013.

[96] D. Vanderbilt, I. Souza, and F. Haldane. Comment on weyl fermions and the anomalous hall effect in metallic ferromagnets. *Phys. Rev. B Phys Rev B*, 89:117101, 2014.

[97] D. Varjas, F. de Juan, and Y.-M. Lu. Bulk invariants and topological response in insulators and superconductors with nonsymmorphic symmetries. *Physical Review B*, 92(19):195116, 2015.

[98] M. Vazifeh and M. Franz. Electromagnetic response of weyl semimetals. *Phys. Rev. Lett.*, 111(2):027201, 2013.

[99] X. Wan, A. M. Turner, A. Vishwanath, and S. Y. Savrasov. Topological semimetal and fermi-arc surface states in the electronic structure of pyrochlore iridates. *Phys. Rev. B*, 83(20):205101, 2011.

[100] Z. Wang, Y. Sun, X.-Q. Chen, C. Franchini, G. Xu, H. Weng, X. Dai, and Z. Fang. Dirac semimetal and topological phase transitions in a 3 bi (a= na, k, rb). *Phys. Rev. B*, 85(19):195320, 2012.

[101] Z. Wang, H. Weng, Q. Wu, X. Dai, and Z. Fang. Three-dimensional dirac semimetal and quantum transport in cd 3 as 2. *Phys. Rev. B*, 88(12):125427, 2013.

[102] X.-g. Wen and A. Zee. Classification of abelian quantum hall states and matrix formulation of topological fluids. *Phys. Rev. B*, 46(4):2290, 1992.

[103] H. Weng, Y. Liang, Q. Xu, Y. Rui, Z. Fang, X. Dai, and Y. Kawazoe. Topological node-line semimetal in three dimensional graphene networks. *arXiv preprint arXiv:1411.2175*, 2014.

[104] Y. Xia, D. Qian, D. Hsieh, L. Wray, A. Pal, H. Lin, A. Bansil, D. Grauer, Y. Hor, R. Cava, et al. Observation of a large-gap topological-insulator class with a single dirac cone on the surface. *Nat. Phys.*, 5(6):398–402, 2009.

[105] D. Xiao, W. Yao, and Q. Niu. Valley-contrasting physics in graphene: magnetic moment and topological transport. *Phys. Rev. Lett.*, 99(23):236809, 2007.

[106] S.-Y. Xu, C. Liu, N. Alidoust, M. Neupane, D. Qian, I. Belopolski, J. Denlinger, Y. Wang, H. Lin, L. Wray, et al. Observation of a topological crystalline insulator phase and topological phase transition in pb1- xsnxte. *Nat. Comm.*, 3:1192, 2012.

[107] B.-J. Yang and N. Nagaosa. Classification of stable three-dimensional dirac semimetals with nontrivial topology. *arXiv preprint arXiv:1404.0754*, 2014.

[108] K.-Y. Yang, Y.-M. Lu, and Y. Ran. Quantum hall effects in a weyl semimetal: Possible application in pyrochlore iridates. *Phys. Rev. B*, 84(7):075129, 2011.

[109] M. Yoo, T. Fulton, H. Hess, R. Willett, L. Dunkleberger, R. Chichester, L. Pfeiffer, and K. West. Scanning single-electron transistor microscopy: Imaging individual charges. *Science*, 276(5312):579–582, 1997.

[110] S. M. Young, S. Zaheer, J. C. Y. Teo, C. L. Kane, E. J. Mele, and A. M. Rappe. Dirac semimetal in three dimensions. *Phys. Rev. Lett.*, 108:140405, Apr 2012.

[111] J. Zak. Berrys phase for energy bands in solids. *Phys. Rev. Lett.*, 62(23):2747, 1989.

[112] F. Zhang, C. Kane, and E. Mele. Topological mirror superconductivity. *Phys. Rev. Lett.*, 111(5):056403, 2013.

[113] T. Zhang, P. Cheng, X. Chen, J.-F. Jia, X. Ma, K. He, L. Wang, H. Zhang, X. Dai, Z. Fang, et al. Experimental demonstration of topological surface states protected by time-reversal symmetry. *Phys. Rev. Lett.*, 103(26):266803, 2009.

[114] A. Zyuzin and A. Burkov. Topological response in weyl semimetals and the chiral anomaly. *Phys. Rev. B*, 86(11):115133, 2012.